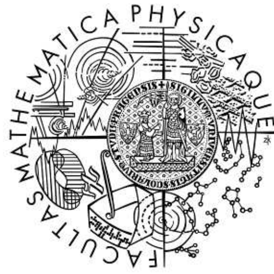

FACULTY
OF MATHEMATICS
AND PHYSICS
Charles University

DOCTORAL THESIS

Artem Musiienko

Photo-Hall effect spectroscopy and laser-induced transient currents in CdTe-based semiconductor radiation detectors

Institute of Physics of Charles University

Supervisor of the doctoral thesis: Prof. RNDr. Roman Grill, CSc.

Study program: Physics

Specialization: Quantum Optics and Optoelectronics

Prague 2018

I declare that I carried out this doctoral thesis independently, and only with the cited sources, literature and other professional sources.

I understand that my work relates to the rights and obligations under the Act No. 121/2000 Coll., the Copyright Act, as amended, in particular the fact that the Charles University has the right to conclude a license agreement on the use of this work as a school work pursuant to Section 60 paragraph 1 of the Copyright Act.

In…......... date.............   signature Mgr. Artem Musiienko

Acknowledgment

I would like to thank especially my supervisor Prof. RNDr. Roman Grill, CSc. for the procreative discussions about the ideas of the work, experiments, and theory. I am grateful to Doc. RNDr. Pavel Moravec, CSc. for shared experience and experimental details. I am also thankful to Doc. Ing. Eduard Belas, CSc., Doc. Ing. Petr Praus, CSc., Prof. Ing. Jan Franc, DrSc., RNDr. Jakub Pekárek, Ph.D., RNDr. Jakub Zázvorka, Ph.D., RNDr. Václav Dědič, Ph.D., Hassan Elhadidy, Ph.D., Mgr. Igor Vasylchenko, Mgr. Lukáš Šedivý, Mgr. Katarína Ridzoňová, and other colleagues at the Institute of Physics at Charles University for their help in my research. My thanks also belong to my family and my closest friends for their support. I would like also to thank the Charles University Grant Agency (project No. 8515) for the financial support of the part of my Ph.D. study.

Title: Photo-Hall effect spectroscopy and laser-induced transient currents in CdTe-based semiconductor radiation detectors
Author: Artem Musiienko

Department / Institute: Institute of Physics of Charles University
Supervisor of the doctoral thesis: Prof. RNDr. Roman Grill, CSc, Institute of Physics of Charles University

Abstract:
Cadmium Telluride, Cadmium Zinc Telluride, and Cadmium Manganese Telluride are important semiconductors with applications in radiation detection, solar cells, and electro-optic modulators. Their electrical and optical properties are principally controlled by defects forming energy levels within the bandgap. Such defects create recombination and trapping centers capturing photo-created carriers and depreciating the performance of the detector. Simultaneously, the changed occupancy of levels leads to the charging of detector's bulk, which results in the screening of applied bias and the loss of detector's sensitivity. Detailed knowledge of crystal defect structure is thus necessary for the predictable detector work and also for the possibility to reduce the structural defects concentration.

This thesis reports on the investigation of deep energy levels in CdTe-based high resistivity and detector-grade materials by photo-Hall effect spectroscopy. The existing approach is also extended by dual-wavelength and enhanced monochromatic excitations. Experimental results are completed by numerical simulations based on the Shockley-Read-Hall model.

A method is presented for the determination of the carriers drift mobility, lifetime, electric field distribution, and the dynamics of space charge in polarizing semiconductor radiation detectors. The procedure stems from the laser-induced transient current measurements done at steady-state and pulsed biasing and at variable temperature.

Keywords: CdTe, CdZnTe, CdMnTe, photo-Hall effect spectroscopy, transient-current-technique, Shockley–Read–Hall model simulations, deep levels, semiconductors, insulators, radiation detectors.

Contents

1. Introduction 3
1.1. Basic properties of CdTe-based semiconductors used for radiation detection 4
1.2. Crystal defects and deep levels 5
1.3. Deep level spectroscopy techniques and photo-Hall effect spectroscopy 6
1.4. Negative differential photoconductivity 9
1.5. Motivation and goals 10
2. Theory 11
2.1. Carrier transport phenomena 11
2.2. Photo-Hall deep level detection concept 13
2.3. Shockley-Read- Hall carrier generation-recombination model 15
2.4. Metal-Semiconductor contacts and detector polarization 17
2.5. Laser induced transient current technique 24
2.5.1. Laser induced current waveforms 24
2.5.2. Charge collection process in semiconductor radiation detectors 28
3. Experimental 28
3.1. Samples 28
3.2. Photoluminescence 29
3.3. Galvanomagnetic measurements 30
3.4. Photo-Hall spectroscopy measurements 32
3.5. Laser induced transient current technique 34
4. Photo-Hall effect spectroscopy and Photoluminescence in n-type samples 35
4.1. PHES with single wavelength illumination 35
4.2. PHES with dual-wavelength illumination 40
4.2.1. Unusual Hall mobility and Photoconductivity decrease 40
4.2.2. Deep level detection 43
4.2.3. Theoretical simulations and negative differential photoconductivity 47
4.3. Chapter summary 52
5. Photo-Hall effect spectroscopy and Photoluminescence in p-type samples 53
5.1. PHES with conventional illumination sources in p-CdTe 53
5.2. PHES with enhanced white laser illumination in p-$Cd_{1-x}Mn_xTe$ 57
5.2.1. Deep levels, carrier mobility, and negative differential photoconductivity 57
5.2.2. Deep level detection and charge carrier Shockley-Reed-Hall simulations 62
5.2.3. Negative differential photoconductivity characterization and charge carrier transport simulations under high illumination flux 65

5.2.4. Chapter summary 69

6. Characterization of polarizing semiconductor radiation detector by laser-induced transient currents 70

7. Conclusions 75

Bibliography 77

List of Tables 89

List of Abbreviations 90

List of symbols 91

Attachments 95

1. Introduction

Ionizing radiation, invisible to an eye, can be detected using only appropriate physical methods and instrumentation. Moreover, one can use the properties of this radiation for a number of scientific, technical, industrial and medical applications. Detectors of ionizing radiation play a central role in such applications.

Detectors can be divided into groups using three main criteria: time of detection, the complexity of measured radiation information, and physical principle of detection. The first group consists of continuous and integral detectors. Continuous detectors detect each single radiation photon with high-resolution time (typically up to ns); meanwhile, integral detectors can detect only much larger energy portions in a large time intervals (typically seconds). The second group of detectors is determined by information which we get from the radiation such as intensity, photon energy, and spatial distribution of radiation. The last criterion, physical principle of detection, combines photo-chemical and electronic detectors. Photo-chemical detectors use chemical reactions produced by radiation such as a change in a color, temperature, etc.

Electronic detectors are based on electronic circuits which convert and amplify current pulses produced by incident radiation. Incident radiation is typically absorbed by an ionization chamber, scintillator detector, semiconductor detector, magnetic spectrometer, etc. Each type of detector has its advantages and disadvantages. The ionization chamber-based detector, for example, is not compact. Scintillator detector has a longer dead time and indirect radiation conversion. This work is mainly focused on physics of semiconductor materials used for radiation detection in electrical circuits.

Semiconductor radiation detectors have experienced remarkable development in the last few years. They are now used in a large variety of fields, including nuclear physics, X-ray and gamma-ray astronomy and nuclear medicine. Their imaging capabilities, good energy resolution and the ability to fabricate compact systems are very attractive features, in comparison with other types of detectors, such as gas detectors and scintillators. In addition to mastered silicon and germanium technology [1]–[3], intensive research led to the progress of CdTe and CdZnTe to the quality convenient for the extensive detector applications [4], [5]. Multiple compound

semiconductors like GaAs, InP, HgI_2, TlBr, PbI_2, SiC also reached significant improvement [6]–[9]. The possibility to choose a specific material allows users to design their equipment optimally for a needed assignation. Despite a distinct progress in the detector technology, the industry still faces many challenges that stand in the way to multi-purpose cheap detectors.

An engagement of semiconductors in electronic and optoelectronic applications is considerably controlled by deep levels (DLs) associated with crystallographic imperfections [10], [11]. Such defects are responsible for the recombination processes [12], space charge formation and polarization of biased sample [13], [14], and by an emergence of potential non-uniformities inside the device [10], [12]. The material quality strongly controls the price of the ingots [4] and further investigation and improvement of the materials are therefore needed.

1.1. Basic properties of CdTe-based semiconductors used for radiation detection

Binary compound semiconductor CdTe and its ternary modifications $Cd_{1-x}Zn_xTe$ and $Cd_{1-x}Mn_xTe$ have a lot of applications in X- and gamma-ray detection [4], [15], security [16], medicine [15], investigation of the universe [17], and in photovoltaics [18] due to a convenient tunable bandgap and good absorption properties [19], see Table 1. Despite these benefits as-grown materials often suffer from crystallographic defects that deteriorate the transport properties of devices [10]. The CdTe-based material resistivity homogeneity and detection properties can be enhanced by adding Se or Mn into the solution [20], [21] due to uniform segregation of these components. Moreover, the bandgap energy can be controlled by the compound composition [22]. Such compound materials have known limitations for the detector applications such as strong carrier recombination [23] and device polarization [24], [25] caused by deep levels inside the band gap.

Table 1. Several semiconductor material properties at 298 K [4], [26]

Material	Si	Ge	GaAs	CdTe	CdZnTe	TlBr
Crystal structure	Cubic	Cubic	Cubic(ZB)	Cubic(ZB)	Cubic(ZB)	Cubic
Growth method	C	C	CVD	THM	HPB, THM	BM
Atomic number	14	32	31, 33	48, 52	48, 30, 52	81,35
Density (g/cm^3)	2.33	5.33	5.32	6.20	5.78	7.56
Band gap (eV)	1.12	0.67	1.43	1.44	1.57	2.68
Resistivity (Ωcm)	10^4	50	10^7	10^9	10^{10}	10^{12}
$\mu_e\tau_e$ (cm^2/V)	>1	>1	10^{-5}	10^{-3}	10^{-3}-10^{-2}	10^{-5}
$\mu_h\tau_h$ (cm^2/V)	~1	>1	10^{-6}	10^{-5}	10^{-5}	10^{-6}

[a] Growth methods: C - Czochralski, CVD - chemical vapor deposition, THM - traveler heater method, BM - Bridgman method, and HPB - high-pressure Bridgman.

1.2. Crystal defects and deep levels

Inevitable crystallographic defects such as point, line, planar and bulk defects represent one of the most serious problems faced by a semiconductor manufacture technology so far. The presence of such defects in the ordered semiconductor lattice structure leads to a formation of the energy states inside the band gap. These states can be divided into two major groups. The first one, shallow levels, are the less localized states with activation energies E_t typically less or similar to the thermal energy kT. Shallow states are produced by small lattice perturbations and generally act as dopants (donor or acceptor) without harmful influence on the material. The second group is called deep levels with E_t significantly exceeding kT. The difference

from the previous case of shallow states consists in much larger perturbation brought by these defects to the lattice potential in the close vicinity of the defect. Thus, the wave function of the trapped electron (or hole) is much more localized. Deep levels have a harmful impact at the utilization of the semiconductor in optoelectronic applications acting as electron (hole) traps or recombination centers depending on their cross sections ratio σ_e/σ_h, where σ_e (σ_h) is the electron (hole) capture cross-section.

1.3. Deep level spectroscopy techniques and photo-Hall effect spectroscopy

Multiple DLs forming energy states in the band gap have been detected using diverse techniques, each of them has advantages and disadvantages. The deep-level transient spectroscopy (DLTS) [27] has been used effectively for quantitative characterization of DLs involving defect density, activation energy, and carrier capture cross-section. In compensated high-resistivity materials with the free-carrier concentration less than the DLs densities, the straightforward application of DLTS is improper [28] due to the damped signal, which mostly disappears in the noise. Recently, improved DLTS-based techniques to study DLs in wide bandgap semiconductors – low rate DLTS (LRDLTS) [29] and discharge current measurements (DCM) [30] were developed to overcome this obstacle. Other methods based on photo-excitation, photo-DLTS (PDLTS) [27], photo-induced current transient spectroscopy (PICTS) [31] and photoconductivity (PhC) [32], are sensitive methods determining the properties of DLs either from the temperature dependence of the time constant of current transients following an optical excitation pulse in case of PDLTS and PICTS, or in a direct way by observing the characteristic increase of conductivity once the photon energy reaches the excitation energy of the level in case of PhC. The photoluminescence spectroscopy (PL) is also often used for determination of zero-phonon lines (ZPL) of DLs [33]. While PDLTS and PICTS were used for the determination of the DL positions relative to respective bands [27], this feature cannot be deduced by PhC or PL. The character of the trap may be recognized by the thermoelectric effect spectroscopy (TEES) [34], [35] based on the

measurement of electric current of thermally excited carriers emitted from previously optically excited DLs with temperature gradient used as a driving force.

TEES, as well as other techniques based on thermally excited trapped carriers, PDLTS, PICTS, afford the trap energy E_{tT}, which deviates from an actual trap energy $E_t(T)$ according to the formula [34]

$$E_{tT} = E_t(T) - T\frac{dE_t(T)}{dT} \quad (1.1)$$

Anticipating temperature dependent trap energy, the determined E_{tT} may deviate from the room temperature trap energy by an amount of up to 0.1 eV. These methods also do not reveal very deep DLs with trapping energy well above the half of the band gap energy $E_g/2$. The signal of such DLs is exceeded by intrinsic carriers excited at the temperature necessary for such DLs visualization. The heating to a temperature above 400K, where principal DLs are detected, may also irreversibly disturb the quality and electrical properties of studied material [36]. A novel approach to investigate DLs by time-of-flight measurements excited by sub-bandgap light (SBTOF) was reported recently in [37]. The procedure allows researchers to directly identify the ionization energy as well as the character of DLs.

Multiple achievements were attained by photo-Hall effect spectroscopy (PHES). It was used to prove the bipolar character of photo-conduction in high resistivity p-CdTe:Cl [38]. Low-temperature (10–40 K) PHES was successfully used for a characterization of impurities in p-HgCdTe [39]. A phenomenological model of deep donors in GaSb:S was developed and supported by PHES [40], [41]. The character of DLs was revealed in semi-insulating GaAs, where all identified traps were found as electron-type[42]. Another approach to measure the mobility of photo-carriers by polarization-sensitive terahertz emission in the magnetic field was presented by Lin et al.[43]. It was found by Chen et al.[44], [45] that PHES can be used for hybrid organic-inorganic lead $CH_3NH_3PbCl_3$(Br_3 or I_3) perovskites characterization. PHES measurements in materials with low carrier mobility or suppressed Hall signal[46] can be used with combination of the alternating magnetic field and lock-in amplifier[45]. In such a set-up the magnetic signal is chosen as the reference signal. The PHES measurements can be divided into two groups: the Hall signal measurements as a function of illumination intensity at various temperatures

and the Hall signal measurements with different illuminating photon energies. Some modifications of the experiment are possible inside the groups such as dual photon energy illumination [47]or time transient measurements [48].

Table 2. Overview of deep energy levels in (CdZn)Te

E_t (eV)	Type[a]	Capture Cross section (cm^2)	Origin	Method	Ref.
0.26	acceptor	-	Au	PL	[49]
0.35	acceptor	-	Fe	EPR, PL	[50]
0.34	acceptor	10^{-13}	In	DLTS	[51]
0.36	acceptor	10^{-13}	Cu	PICTS	[52]
0.39-0.43	donor	$(2\text{-}5)\times10^{-13}$	Te_{Cd}	TEES	[53]
0.4, 0.43	acceptor	2×10^{-16}	V_{Cd}	DLTS, PICTS	[27], [54]
0.43-0.49	acceptor	10^{-14}	Te_{Cd}-$2V_{Cd}$	TEES	[53]
0.4, 0.5	donor	4×10^{-16}	V_{Te}	Theory	[19], [20]
0.54, 0.64	donor	10^{-12}	Cd_I	PICTS, DLTS	[52], [27],[57]
0.69-0.71	acceptor	5×10^{-14}	Te_{Cd}-$2V_{Cd}$	TEES	[53]
0.73	acceptor	-	Ge	PL	[58]
0.73	donor	-	Mn	Hall	[59]
0.73-0.85	acceptor	2×10^{-12}	Te_{Cd}-V_{Cd}	TEES	[53]
0.74	donor	-	Te_{Cd}	TEES	[60]
0.78	acceptor	4×10^{-13}	V_{Cd}	QTS[a]	[57]
0.8, 0.86	acceptor	5×10^{-13}, 2×10^{-12}	In	QTS, DLTS	[57]
0.88	-	10^{-12}	-	DLTS	[61]
0.85-0.9	donor	5×10^{-12}	Sn	QTS, DLTS	[50], [57],[62]
0.95-1.0	donor	10^{-10}	V	DLTS	[63]
1.1	donor	-	V_{Te}	DLTS,	[27]

				PICTS	
1.1	donor	-	dislocation	DLTS, PL	[64]
1.25	acceptor	-	Co	EPR, PL ODMR	[65]
1.3	donor	-	V_{Cd}	DLTS, PL	[64]

[a]Type of the defect donor/acceptor

1.4. Negative differential photoconductivity

Negative differential photoconductivity (NDPC) is characterized by the decrease of the photoconductivity under illumination [66]. The effect is mathematically described by a negative derivative of photoconductivity PhC with respect to illumination intensity *I*. It can be induced both by a decrease of the electron (hole) concentration n (p) and by a decrease of the carrier mobility μ_e (μ_h) according to the formula

$$\frac{dPhC}{dI} = q_e(\mu_e \frac{dn}{dI} + \mu_h \frac{dp}{dI} + n \frac{d\mu_e}{dI} + p \frac{d\mu_h}{dI}), \quad (8)$$

where q_e is an elementary charge.

The effect of the conductivity decrease under illumination below the dark equilibrium value is known as absolute negative photoconductivity (ANPC) [67]. According to known models, NDPC and ANPC can be induced by two mechanisms. The first one is associated with a decrease of the carrier mobility induced by light radiation. This effect can be reached by stimulation of scattering mechanisms as it was shown for graphene [43], [68], gold nanoparticles [69], Ge(Si) type-II quantum dots [70], and interacting quantum gas [71]. NDPC stimulated by potential non-uniformity was observed by our group in CdZnTe [72] and by Shalish et al. [73] in GaAs films using Hall photo-voltage. The second mechanism producing NDPC is the decrease of the majority carrier concentration due to minority carriers recombination supported by a recombination-type crystallographic defect. This model was firstly proposed by Stockman et al. [74] and implemented for diamond photodetectors [67], thin films [75], MoS_2 monolayers [76], p-type PbEuTe and other materials. Similar mechanism of enhanced radioactive capture of hot electrons was proposed by Ridley et al. [77] for III-V and II-VI semiconductors. Despite a

large number of experimental observations, the detailed theoretical study of NDPC (or ANPC) induced by defect levels was not presented. The simple model was given for inhomogeneous materials by Bube et al. [78]. Despite similar nature of two effects, the connection between NDPC and ANPC was not shown. The dependence of NDPC on DL parameters was also not specified.

1.5. Motivation and goals

CdTe single crystals and its compounds have been studied for decades at the Institute of Physics of Charles University by classic Hall-effect measurements. As it was shown in previous sections 1.1-1.3 semiconductor materials are affected by crystallographic defects which depreciate material detection and transport properties. This thesis is focused on the development of deep level spectroscopy method based on Hall-effect measurements and upgraded by light illumination at different photon energies. This method represents the extension of classic Hall voltage measurements to samples brought out of equilibrium by optical excitation. The second goal of the project is to study deep levels in CdTe/CdZnTe samples used for fabrication of X-ray and gamma-ray detectors by PHES measurements. The data will be further used for comprehensive analysis of the defect structure and negative differential photoconductivity in CdTe based materials by Shockley-Reed-Hall theoretical simulations. Obtained results are important for improving the charge collection and characterization of CdTe/CdZnTe detectors as well as for the description of carrier trapping and understanding the mechanisms of space charge formation.

Semiconductor detectors represent the promising group of devices designed for the direct conversion X-ray and gamma-ray spectroscopy. The third goal of this thesis is to develop a straightforward procedure enabling the determination of principal properties of radiation detectors via the laser-induced transient current technique (L-TCT). The approach is useful in detectors exhibiting polarization in the dark where the complex processes related to the space charge formation in the depletion region near the contact make the common analysis difficult [79], [80].

2. Theory

2.1. Carrier transport phenomena

The standard semi-classical transport theory is based on the Boltzmann equation

$$\frac{\partial f}{\partial t} + \boldsymbol{v}\nabla_r f - \frac{q_e \boldsymbol{F}}{\hbar}\nabla_k f = \left(\frac{\partial f}{\partial t}\right)_{Col}, \tag{2.1}$$

where $\boldsymbol{r}$ is the position, $\boldsymbol{k}$ is the momentum, $f(\boldsymbol{k};\, t)$ is the distribution function (for instance, a Fermi-Dirac in equilibrium), $\boldsymbol{v}$ is the group velocity, $\boldsymbol{F} = -q_e[\boldsymbol{E} + (\boldsymbol{v} \times \boldsymbol{B})]$ is the force (electric and Lorentz force) acting on an electron. The terms on the left hand side indicate, respectively, the dependence of the distribution function on time, space (explicitly related to velocity), and momentum (explicitly related to electric and magnetic fields). The term $\left(\frac{\partial f}{\partial t}\right)_{Col}$ on the right hand side defines the collision term, which accounts for all the scattering events:

$$\left(\frac{\partial f}{\partial t}\right)_{Col} = \sum_{\boldsymbol{k}'}\big[W(\boldsymbol{k}',\boldsymbol{k}) f(\boldsymbol{r},\boldsymbol{k}',t)\big(1 - f(\boldsymbol{r},\boldsymbol{k}',t)\big) - W(\boldsymbol{k},\boldsymbol{k}') f(\boldsymbol{r},\boldsymbol{k},t)\big(1 - f(\boldsymbol{r},\boldsymbol{k}',t)\big)\big], \tag{2.2}$$

where $W(\boldsymbol{k},\boldsymbol{k}')$ is the transition probability between the momentum states $\boldsymbol{k}$ and $\boldsymbol{k}'$, and $[1 - f(\boldsymbol{r},\boldsymbol{k}',t)]$ is the probability of non-occupation for a momentum state $\boldsymbol{k}'$. The Boltzmann equation is valid under assumptions of semi-classical transport: effective mass approximation (which incorporates the quantum effects due to periodicity of the crystal); Born approximation for the collisions, in the limit of small perturbation for the electron-phonon interaction and instantaneous collisions; no memory effects, i.e. no dependence on initial condition terms. Analytical solutions of the Boltzmann equation are possible only under very restrictive assumptions. Direct numerical methods for device simulation have been limited by the complexity of the equation, which in the complete 3-D time-dependent form requires seven independent variables for time, space and momentum. In the simplest approach, the collision term on the right hand side of Eq. 2.2) is substituted with a phenomenological term

$$\left(\frac{\partial f}{\partial t}\right)_{Col} \approx -\frac{f - f_0}{\tau}, \tag{2.3}$$

where f_0 indicates the (local) equilibrium distribution function, and τ is a microscopic relaxation time. The dominant scattering mechanisms are provided by

phonons or defects in the material. Both scattering mechanisms depend on the temperature.

Relying on the effective mass and mobility approximation concept the current density in the case of only longitudinal current can be represented as follows:

$$\boldsymbol{J} = \sigma \boldsymbol{E} = \left(\frac{q_e^2 n}{m_e^*} \langle \tau_e \rangle + \frac{q_e^2 p}{m_n^*} \langle \tau_h \rangle \right) \boldsymbol{E} = q_e (n\mu_e + p\mu_h) \boldsymbol{E}, \tag{2.4}$$

where $\langle \tau_e \rangle (\langle \tau_h \rangle)$, and $n(p)$ are the electron (hole) average scattering time constant and carrier concentration. Carrier drift mobility $\mu_e(\mu_h)$ characterizes transport of electrons (holes) caused by electric field. Bimolecular conductivity σ can be founded according to the Ohm law from the resistivity ρ

$$\sigma = \frac{1}{\rho} = \frac{IS}{Ul}, \tag{2.5}$$

where *I*, *U*, *S*, and *l* are the absolute current, longitudinal voltage drop, sample cross section and crystal length.

Let's now consider the semiconductor with longitudinal current in perpendicular magnetic field **B**. Lorenz force effects electrons, which create the transversal voltage drop across the sample. This voltage compensates the Lorenz force and steady state conditions are established:

$$q_e E = q_e v B = q_e \frac{j}{q_e n} B \tag{2.6}$$

$$E = \frac{j}{q_e n} B. \tag{2.7}$$

There the carrier velocity v can be defined from the current j. Hall coefficient R_H is defined by the following relation in n-type semiconductors.

$$R_H = -r_H \frac{1}{q_e n} = \frac{V_H d}{IB}, \tag{2.8}$$

where d is a sample thickness. The Hall factor r_H is a constant given for a specific material (the value can vary from 1 up to 3 [81]). For a CdTe-based materials $r_H = 1$ is chosen [38]. The Hall mobility μ_H is defined by

$$\mu_H = |\sigma R_H| = \left| \frac{\sigma V_H d}{IB} \right| = \begin{cases} \mu_n, & if\ n \gg p; \\ \mu_h, & if\ n \ll p. \end{cases} \tag{2.9}$$

The drift mobility can be found when one type of carrier concentration dominates. For a p-type material only sign of the charge in Eq. 2.8 will change.

The Hall coefficient in a low doped semiconductor (or intrinsic) where the minority carrier concentration cannot be neglected is given by the following relation

$$R_H = \frac{(p\mu_h^2 - n\mu_n^2)}{q_e(p\mu_h + n\mu_n)} \tag{2.10}$$

and the Hall mobility is given by

$$\mu_H = \frac{|\mu_h^2 \cdot p - \mu_e^2 \cdot n|}{\mu_h \cdot p + \mu_e \cdot n}. \tag{2.11}$$

The bipolar photoconductivity *PhC* after illumination is related to the free electron *n* and hole *p* concentrations by relation:

$$PhC = q_e[\mu_h(p - p_0) + \mu_e(n - n_0)], \tag{2.12}$$

where $n_0(p_0)$ represent carrier concentration in equilibrium.

2.2. Photo-Hall deep level detection concept

The transverse Hall voltage and longitudinal conductivity in the dark in p-type material depend on the dark minority (n_0) and majority (p_0) carrier concentrations and their mobilities. Dark carrier concentrations are further adjusted by photo-generated holes $p = p_0 + \Delta p$ and electrons $n = n_0 + \Delta n$ after illumination of the sample. It is important to note that $\Delta n \neq \Delta p$ and corresponding values mainly depend on filling of DLs in the band gap, illumination photon energy, and intensity. In case of ANPC Δn or Δp may be even negative. Whenever the illumination photon energy ($h\nu$) reaches the trap energy counted relatively to the respective band, free electrons or holes are generated. This leads to a change of the spectral envelope and a rise in conductivity. An increase of μ_H can be provided by the free hole generation, see Eq. (2.11). On the contrary, photo-generated electrons provide a decrease of μ_H until the sign reversal of V_H arises at $n = \left(\frac{\mu_h}{\mu_e}\right)^2 \cdot p$, which may be well approximated by $n \approx 0.01 \cdot p$ for studied CdTe-based compound materials. Let us mention that whilst positive V_H proves the p-type character of the material, due to the higher electron mobility, in CdTe based materials, the negative V_H does not directly testify to the n-type. The comparison of μ_e and μ_H must be than included to solve this task.

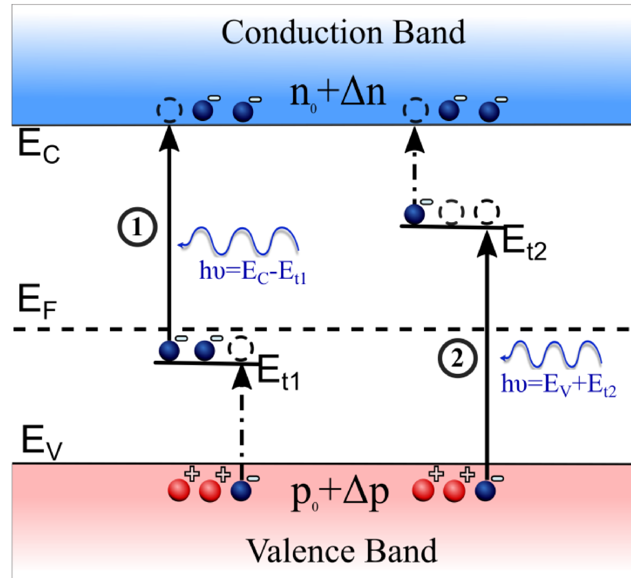

Fig. 2.1. Competing deep level models No 1 and No 2 . Solid and dashed arrows show direct and secondary carrier generation processes correspondingly. E_F shows Fermi level position in p-type material.

Analyzing μ_H as a function of photon energy and light intensity enables us the determination of the position of the DLs inside the band gap correspondingly. Due to the higher electron mobility even smaller rise up of electron concentration caused by secondary electron emission from the DL with threshold energy E_t>E_F outlined by DL model No 2 in Fig. 2.1 might produce μ_H decrease. The secondary emission involves thermal detrapping and secondary photon induced transition ($E_g - hv$) to the conduction band. A smart treatment must be chosen for the resolution of this task. The solution of the problem stems from different mechanisms of free electrons generation. The photon-induced transition from the filled DL below E_F to the conduction band satisfies the rule $\Delta n = \Delta n_t^{empt} + \Delta p$, where Δn_t^{empt} is a concentration of photo-induced empty states of the deep level (see Fig. 2.1). Therefore, such a transition is followed by prevailing photoelectron concentration $\Delta n > \Delta p$. The secondary electron emission produced by empty (or nearly empty) DL with the energy E_t>E_F is ruled by similar relation $\Delta n + \Delta n_t = \Delta p$, where Δn_t is a concentration of trapped electrons on the deep level. As we can see, this alternative transition is followed by predominant hole generation and the photo-generated hole concentration must be higher $\Delta p > \Delta n$ than the concentration of photo-generated electrons. The distinctions at the electron excitation mechanisms from DL localized below or above E_F was used at the determination of DL position in the bandgap

using the dual wavelength excitation [72]. Similar concept can be used in a p-type material where $\mu_h > \mu_e$.

2.3. Shockley-Read- Hall carrier generation-recombination model

The Shockley-Read-Hall (SRH) theory [82] completed by illumination-mediated deep level - band transitions shown in Fig. 2.2 is used to analyze in details two alternative DL models (presented in section 2.2) and NDPC appearance. The evaluation of corresponding charge dynamics is performed in steady state illumination regime. Equations (2.13-2.15) represent the electron and hole dynamics correspondingly.

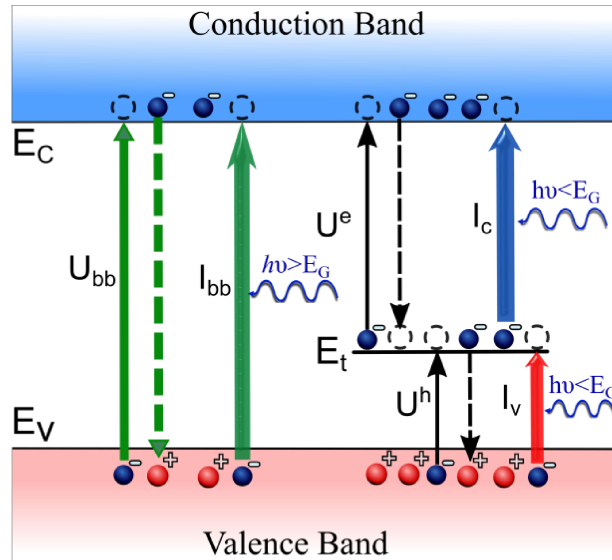

Fig. 2.2. Shockley-Reed-Hall carrier generation-recombination model. Solid and dashed arrows show carrier generation and recombination processes correspondingly.

$$\frac{\partial n}{\partial t} = -\sum_i U_i^e + \sum_i I_{ci} + I_{bb} - U_{bb}, \tag{2.13}$$

$$\frac{\partial p}{\partial t} = -\sum_i U_i^h + \sum_i I_{vi} + I_{bb} - U_{bb}, \tag{2.14}$$

$$\frac{\partial n_{ti}}{\partial t} = U_i^e - I_{ci} - U_i^h + I_{vi}, \tag{2.15}$$

$$U_i^e = \sigma_{ei} v_e [(N_{ti} - n_{ti})n - n_{ti} n_{1i}], \tag{2.16}$$

$$U_i^h = \sigma_{hi} v_h [n_{ti} p - (N_{ti} - n_{ti}) p_{1i}], \tag{2.17}$$

$$I_{ci} = I\tilde{\alpha}_{ei} n_{ti}, \tag{2.18}$$

$$I_{vi} = I\tilde{\alpha}_{hi}(N_{ti} - n_{ti}), \tag{2.19}$$

$$I_{bb} = G_{bb} I, \tag{2.20}$$

$$U_{bb} = C_{bb}(np - n_i^2). \tag{2.21}$$

Here n, p, n_{ti}, U_i^e (U_i^h), $I_{bb}$and U_{bb} are the densities of free electrons, free holes, electron trapped in the i-th level, electron (hole) net recombination rate at the i-th level, the interband light induced generation rate, and the band-to-band net recombination rate respectively. The quantities defining recombination rates n_i, N_{ti}, σ_{ei}, σ_{hi}, ν_e and ν_h in Eqs. (2.16-2.21) are intrinsic carrier density, i-th DL density, electron and hole thermal capture cross sections, and electron (hole) thermal velocities, respectively. Symbols n_{1i} and p_{1i} stand for electron and hole densities in case of Fermi level E_F being set equal to the DL ionization energy E_{ti} [82]. The effect of the illumination on the i-th DL occupancy is defined by I_{ci} (I_{vi}) generation rate from i-th level to the conduction (valence) band where I, $\tilde{\alpha}_{ei}$, and $\tilde{\alpha}_{hi}$ are the photon flux and photon capture cross sections relevant to the conduction and valence band transition respectively. The interband light induced generation rate I_{bb} can be neglected for $h\nu<E_g$.. The band-to-band recombination constant C_{bb} = 10^{-11} cm^2 can be estimated according to Ref. [83]. The band-to-band recombination rate is much lower in comparison with DL assisted recombination and can be neglected. The value of photon capture cross sections were chosen to fit the shape of PHES spectra and the order of magnitude was chosen according to Ref. [72]. Both photon energy and photon flux dependencies were fitted simultaneously by the same parameters. The charge neutrality is assured by the neutrality equation

$$p - n - \sum_i n_{ti} = p_0 - n_0 - \sum_i n_{t0i}, \tag{2.22}$$

where the equilibrium zero-indexed quantities p_0, n_0,and n_{t0i} on the right-hand side are defined by the position of Fermi level E_F. The solution of equations (2.13-2.15) and (2.22) significantly simplifies in the steady state regime, where the time derivatives are set to zero. The electron and hole lifetimes τ_e and τ_h can be found by relations:

$$\tau_e = \frac{1}{\sum_i v_{ei}\sigma_{ei}(N_{ti} - n_{ti})}, \tag{2.23}$$

$$\tau_h = \frac{1}{\sum_i v_{hi}\sigma_{hi}n_{ti}}. \quad (2.24)$$

The occupation of DLs can be conveniently described by a dimensionless filling factor (FF) which is defined by us as the ratio of DL electron occupation and the total DL concentration $f_i = n_{ti}/N_{ti}$. The change of the DL occupation from the equilibrium under illumination intensity I can be presented by reduced filling factor $F_i(I)$, $-1 < F_i < 1$:

$$F_i(I) = f_i(I) - f_i(0). \quad (2.25)$$

The occupation and depletion of the deep level can be tracked by the positive or negative sign correspondingly.

2.4. Metal-Semiconductor contacts and detector polarization

Metal-semiconductor contacts are obvious components of any semiconductor device. Depending on the material properties of the metal and the semiconductor, we usually distinguish two types of metal-semiconductor junctions: the rectifying contact (known as Schottky barrier) and non-rectifying, which is also called ohmic contact. Rectifying contact has nonlinear current–voltage characteristic and the resistance is orders of magnitude smaller at the forward bias than at reverse bias. The resistivity of the ohmic contact adheres to Ohm's law with a linear current–voltage characteristic. For a given semiconductor, the type of contact depends primarily on the difference between the values of the work functions of a semiconductor $q\phi_s$ and metal $q\phi_m$ materials. The work function ϕ is the minimum thermodynamic work (i.e. energy) needed to remove an electron from a solid to a point in the vacuum (i.e. vacuum level E_{Vac}) immediately outside the solid surface. The semiconductor is also characterized by the electron affinity χ, defined as the distance between the vacuum level and the lower edge of the conduction band E_C. Note that χ is not affected by the doping of the semiconductor. In the further discussion we neglect surface states and oxide layers on a semiconductor surface for simplicity. In reality, surface states and additional oxide interlayer can significantly affect contact properties [84].

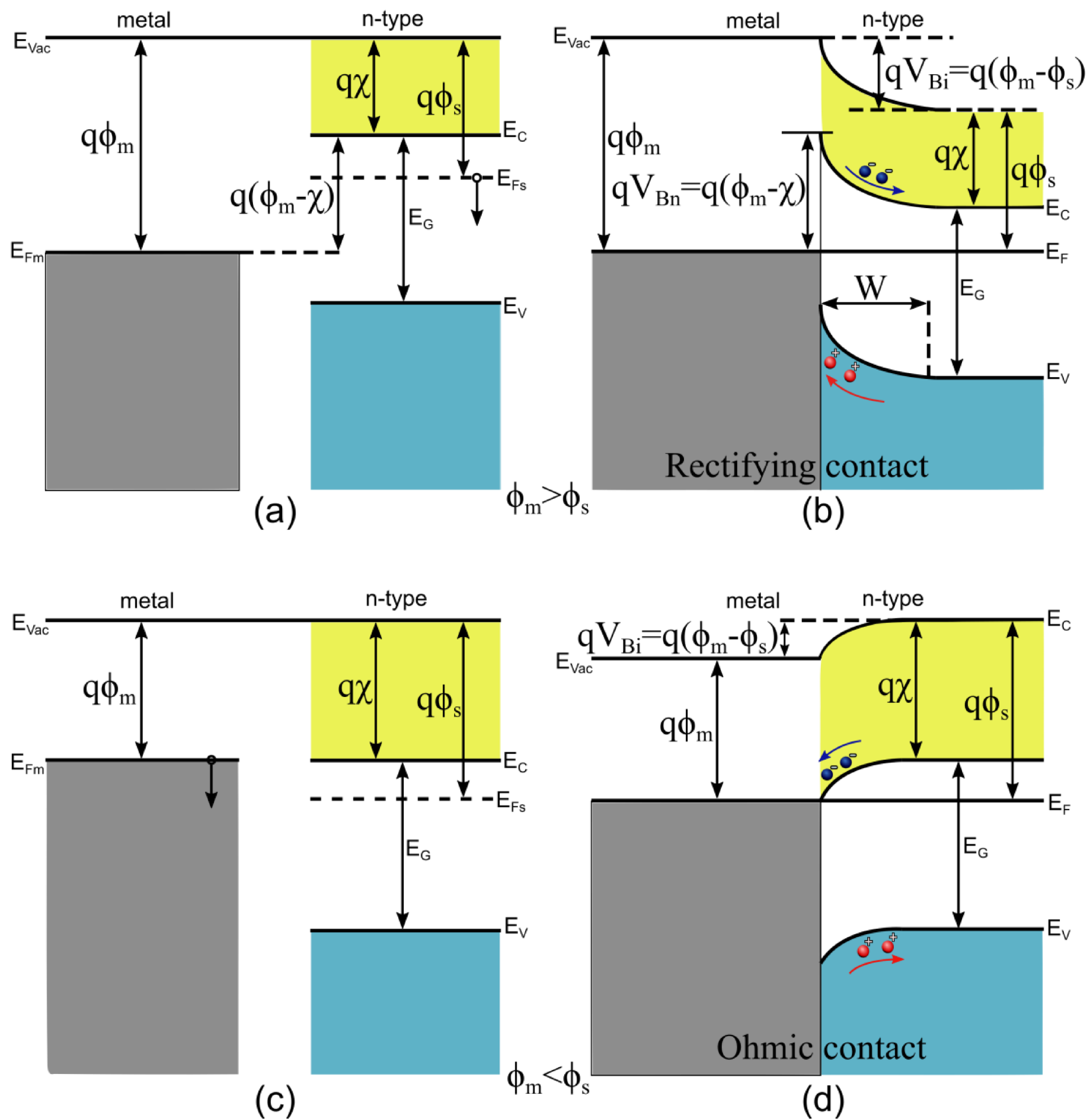

Fig. 2.3. The band diagrams of a metal and n-type semiconductor. (a) before and (b) after the conjunction with a metal of a greater work function than that of semiconductor; (c) before and (d) after the conjunction with a metal of a smaller work function than that of semiconductor.

Fig. 2.3 (a) shows the separated band diagrams of a metal and an n-type semiconductor in case of $q\phi_m > q\phi_s$. The Fermi level in the n-type semiconductor is shifted into the direction of the conductive band. If the metal and the semiconductor are brought together and form an ideal contact, two requirements must be fulfilled:

a) at thermal equilibrium the Fermi level energy must be constant throughout the junction;

b) the vacuum level must be continuous.

Due to higher Fermi level in semiconductor (E_{Fs} > E_{Fm}) electrons flow from semiconductor into the metal in dynamic state of the system until Fermi levels align in both materials. The passed electrons leave uncompensated positive space charge in semiconductor which is responsible for creation of the electric field E near the contact. As a result, a barrier is formed between the metal and the semiconductor, as depicted in Fig. 2.3(b). The electric field prevents prevailing electron transfer (due to thermal emission or tunneling through the barrier) from the semiconductor to metal and enhances electrons flow from metal to semiconductor. The total current through the junction is equal to zero. The energy difference between the level where the conduction band meets the metal and the Fermi level E_F is called the Schottky barrier, qV_{Bn}. This barrier represents the energy required for electron injection from the metal into the semiconductor and it is a characteristic for this junction. For an n-type semiconductor, the height of this barrier is given by

$$qV_{Bn} = q(\phi_m - \chi). \tag{2.26}$$

In the quasi-neutral region the bands of the semiconductor are horizontal, reflecting the fact that there is no voltage drop across this region. We can see easily that the metal-semiconductor work function difference also forms a barrier (built-in potential barrier qV_{Bi}) for electrons to travel from the n-type semiconductor to the metal. This barrier obstructs the straightforward collection of electrons in the semiconductor by the metal [85], [86].

The region between the metal and the quasi-neutral region is denoted as the depletion region and this region has a width W. The word “depletion” implies that region is depleted of free charge carriers; free electrons in the case of an n-type semiconductor. As a result the charge density in this region is formed by positively charged donor ions (or another non-compensated lattice defects) that are fixed in the semiconductor lattice. In the depletion region this charge density is constant as a function of position. Evidently, charge neutrality imposes that an equal amount of negative charge is present in the metal near the interface. In reality, it is surface charge right at the interface with the semiconductor. The charge distribution and electric field profile are schematically shown in Fig. 2.4. As the density of states in the metal is much larger than in semiconductor, the thickness of the charged region in the metal, blue region in Fig. 2.4, is much thinner than it is sketched in the figure.

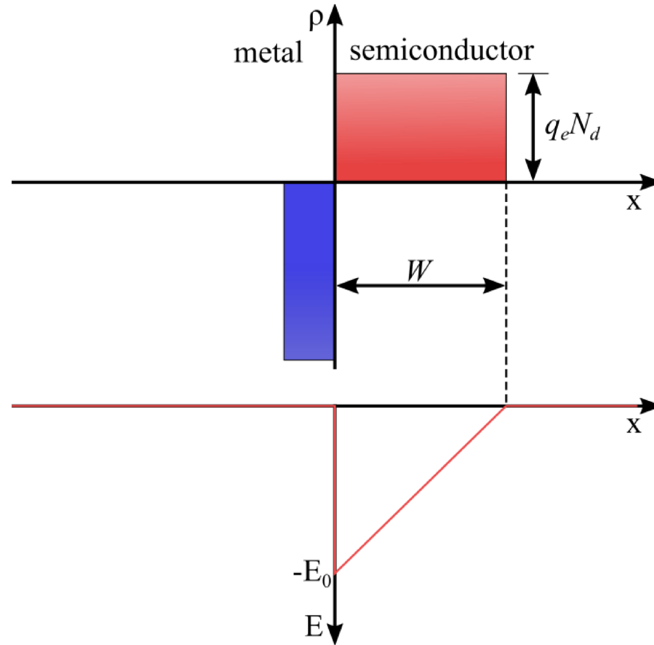

Fig. 2.4. The charge distribution and the electric field profile in the metal-semiconductor junction.

We can now estimate the electric field distribution $E(x)$ using the Poisson equation and Gauss's law involving the electrostatic potential $\phi(x)$ and the space charge density ρ:

$$\frac{d^2\phi(x)}{dx^2} = -\frac{E(x)}{dx} = -\frac{\rho}{\varepsilon}. \tag{2.27}$$

The electric field strength is zero at the edge of the depletion region and it has linear profile $E(x) = E_0 + ax$ in the depletion region. Applying the Poisson equation again we can see that $\phi(x)$ will vary parabolically with x in the depletion region and the bands in the semiconductor bend upwards. When the built-in voltage of the junction and the charge density in the depletion region are known, the depletion region width can be determined as

$$W_0 = \sqrt{-\frac{2\varepsilon V_{Bi}}{qN_d}}. \tag{2.28}$$

Let's now apply a bias voltage to the rectifying junction. We will first consider the case in which we apply a forward bias voltage, which means a negative voltage on the n-type semiconductor with respect to the metal. As a result, the quasi-neutral part of the n-type semiconductor will be at a higher potential energy and the barrier for electrons to travel from the semiconductor to the metal is reduced from V_{Bi} to

$V_{Bi} - V$, where V is the applied voltage. The width of the depletion region W has reduced:

$$W = \sqrt{-\frac{2\varepsilon(V_{Bi} - V)}{qN_d}}. \quad (2.29)$$

The slope, a, of the electric field distribution has not changed, as this slope is determined by the charge density in the depletion region.

Table 3. Work function of some metals and semiconductors [87]–[92]

Material	$q\phi$(eV)	Material	$q\phi$(eV)
Ag	4.26 - 4.74	Se	5.9
Al	4.06 - 4.26	Sn	4.42
As	3.75	Te	4.95
Au	5.10 - 5.47	W	4.2
C	~5	Zn	3.63 - 4.9
Cd	4.08	$MAPbI_3$[a]	3.7 - 5.2
Cs	1.95	GaAs	4.69
Cu	4.53 - 5.10	CdTe	5.2 - 5.7
Fe	4.67 - 4.81	CdZnTe	5.09 - 6.0
In	4.09	InSb	4.57
Mg	3.66	Ge	4.75
Mn	4.1	Bi_2Te_3	5.3
Ni	5.04 - 5.35	Si	4.85
Pb	4.25	SiC	4.6-4.8
Pt	5.12 - 5.93	ZnO	4.5

[a] $CH_3NH_3PbI_3$

Now let's consider reverse bias voltage. In that case, the Fermi level of the semiconductor is below that of the metal and the barrier for electrons to travel from the semiconductor to the metal has increased to $V_{Bi} + V$. The applying of a reverse bias increases the depletion region width according to Eq. (2.29) where the sum of

voltages is used. The general current-voltage characteristic of a metal-semiconductor contact under thermionic emission is given by

$$J(V) = J_s(e^{q_e V/k_b T} - 1), \tag{2.30}$$

where the saturation current density J_s is given by the following equation

$$J_s = \tilde{A}T^2 e^{-q_e V_{Bn}/k_b T}. \tag{2.31}$$

The constant $\tilde{A}$ is the Richardson constant for thermionic emission, which is given by

$$\tilde{A} = \frac{4\pi q m_n^* k^2}{h^3} \tag{2.32}$$

with the effective electron mass m_n^*. Also, transport of minority carriers occurs, but it is orders of magnitude smaller than the majority carrier transport.

The contact resistivity R_C can be simply defined from Eq. (2.31)

$$R_C = \left(\frac{\delta J}{\delta V}\right)_{V=0}^{-1} = \frac{k}{q_e \tilde{A} T} \exp\left(\frac{q_e V_{Bn}}{k_b T}\right) \tag{2.33}$$

or if the semiconductor has a high doping concentration N_D and quantum-mechanic tunneling of the charge carriers through the barrier becomes more probable (due to the decrease of barrier width, see. Eq. (2.29)) we find

$$R_C \sim \exp\left(\frac{8\pi\sqrt{m_n^*}\varepsilon_s q_e V_{Bn}}{\sqrt{N_D}h}\right). \tag{2.34}$$

For reducing the contact resistance, the barrier height should be kept low and vice versa.

Now look at the case in which the work function of the semiconductor is larger than of the metal, see Fig. 2.3 (c-d). Like we have seen for the Schottky barrier junction, the Fermi level in thermal equilibrium should line up but there is no barrier for electrons in the conduction band of the semiconductor to transfer to the metal. The absence of the barrier eases the current flow and the bands in the semiconductor bend downwards. There is no depletion region and due to the bending resulting from the differences in work function the electron density and negative space charge increase near the junction. In case of weak band bending the general current-voltage characteristic of a metal-semiconductor ohmic contact is given by simple linear relation. Large bend banding induces significant space charge formation under forward bias and a model of the space-charge-limited currents must be engaged [93], [94].

In case of a p-type semiconductor the rectifying contact is formed if $q\phi_m < q\phi_s$ and respectively an ohmic contact is formed if $q\phi_m > q\phi_s$, see Fig. 2.5.

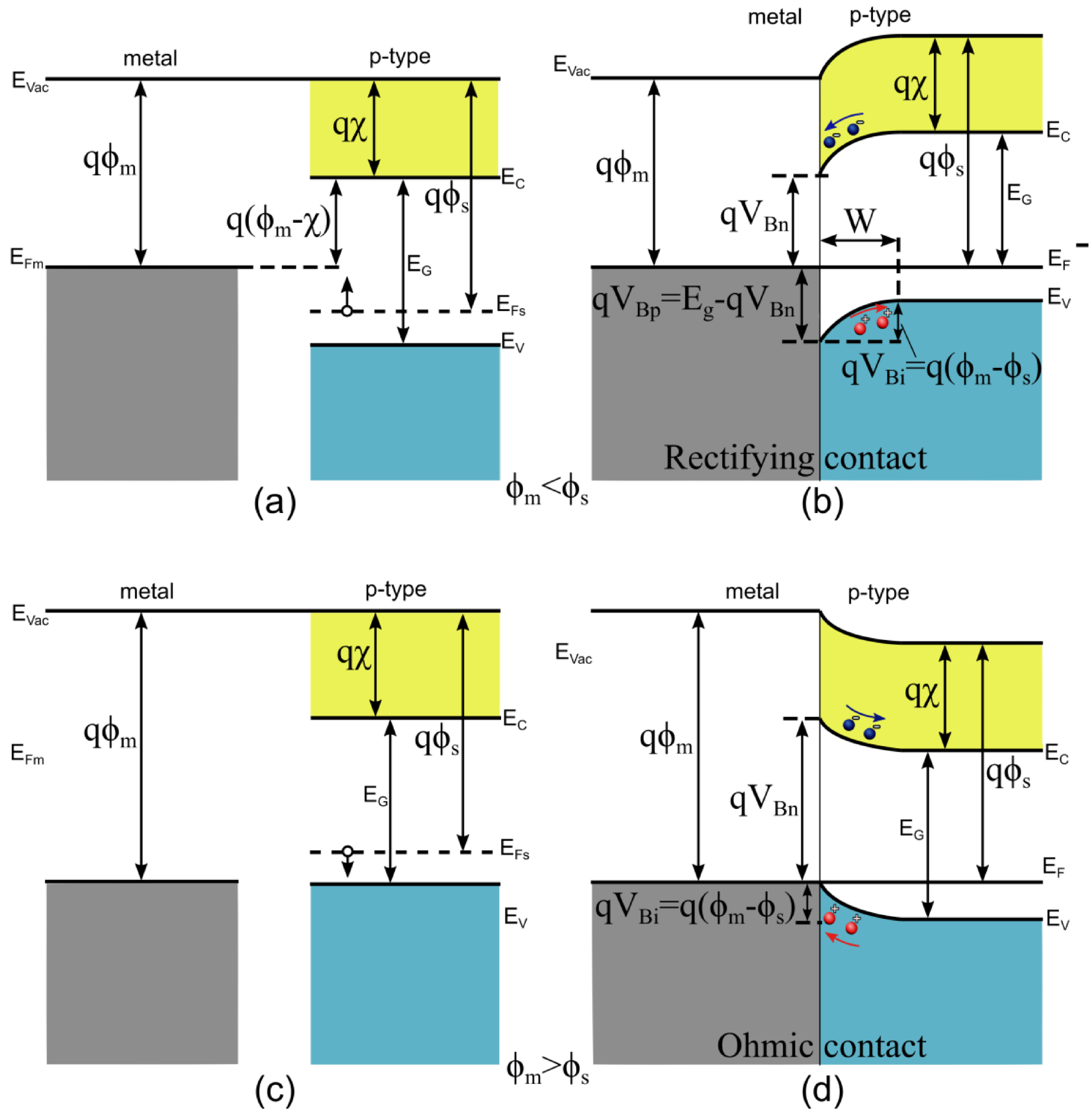

Fig. 2.5. The band diagrams of a metal and p-type semiconductor. (a) before and (b) after the conjunction with a metal of a smaller work function than that of semiconductor; (c) before and (d) after the conjunction with a metal of a greater work function than that of semiconductor.

The height of the barrier for holes is given by

$$qV_{Bp} = E_G - q(\phi_m - \chi). \tag{2.35}$$

2.5. Laser induced transient current technique

2.5.1. Laser induced current waveforms

In this chapter we present a procedure which enables to determine principal characteristics of radiation detectors via the laser-induced transient current technique (L-TCT). The approach is especially useful in detectors exhibiting polarization in the dark where the complex processes related to the space charge formation in the depletion region near the contact make the common analysis difficult [79], [80]. The theory is developed for the detector polarizing due to the carriers depletion induced by Schottky contact on the irradiated cathode as shown in Fig**.** 2.6**.** The space charge

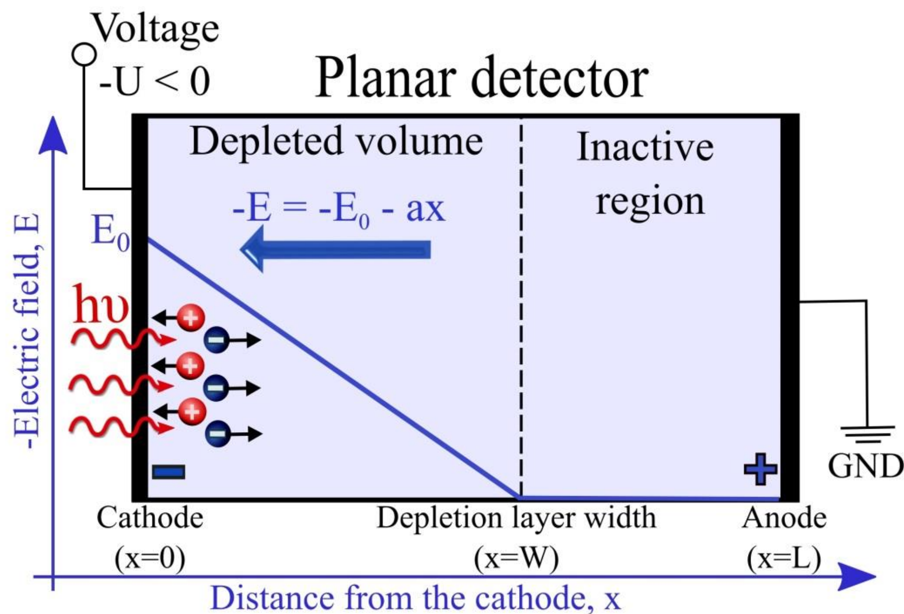

Fig. 2.6. Schematic view of the electric field profile in a detector with a positive space charge formed under the cathode. The laser illumination from the cathode side is used. The bias $U > 0$ marks the anode-cathode potential difference.

is not electrically compensated by free carriers in the depletion region so that a linear drop of the electric field occurs. The validity of the theoretical concept is demonstrated on a fast polarizing n-CdTe detector in the dark, where all evaluation steps may be well tracked. The term ‘fast polarization’ is used to express the rate of the space charge buildup, which takes about 0.1s in contrast to multiple other measurements [95] where significantly slower space charge formation was reported. In our approach we demonstrated that, if the L-TCT synchronized with pulsed bias

was applied, even the fast polarization did not disable the use of the proposed treatment.

Based on the model of detector polarization [34], a spatially constant space charge arising due to the electron detrapping from an electron trap and the positive space charge formation in the depleted region is assumed. The electric field profile $E(x)$ may be then expressed in the form [79], [96]

$$-E(x) = max\{0, -E_0 - ax\}, \quad (2.36)$$

where $a=eN/(\varepsilon_0\varepsilon_r)$. The values E_0, e, ε_0, ε_r, and N are the electric field at the cathode, elementary charge, vacuum and relative permittivity, and normalized space charge density expressed in cm^{-3} units, respectively. Note that the electric field is negative in the depleted region as the cathode is placed in $x=0$. Once N exceeds a certain value [79], the inactive region with a zero electric field appears near the anode 'dead layer'. The space charge in the inactive region is reverted to zero as well. It was shown [97] that the current transient induced by moving electrons produced by the laser pulse may be expressed in a proportionality relation via a single exponent as

$$i(t) \propto e^{-\left(a+\frac{1}{\mu\tau}\right)\mu t} = e^{-ct}, \quad (2.37)$$

where μ is electron mobility, τ is electron lifetime and c $(=a\mu+1/\tau)$ is a damping parameter characterizing current waveform (CWF) during the charge passing through the detector. Note that the exponential-shaped CWF may be used for the practical verification of the assumed constant N within the detector. We also point out that the detrimental effect of the surface recombination, which often hampers evaluation of the mobility-lifetime product by the fitting of the Hecht relation at L-TCT [98], does not affect the shape of Eq. ((2.37).

Another feature characterizing the CWF termination is the transit time t_{tr} defining the period of the electrons drifting to the anode. While in unpolarized detector $t_{tr}=L^2/(\mu U)$, where L is the detector thickness and U is a bias, t_{tr} in the polarized detector is obtained in the more complex form [97]

$$t_{tr} = \frac{1}{a\mu} ln\left(\frac{1+\frac{aL^2}{2U}}{1-\frac{aL^2}{2U}}\right) \quad (2.38)$$

showing an effect of polarization on t_{tr}. On inspecting Eq. (2.38), one may see that t_{tr} is converging to infinity at $aL^2/(2U)\rightarrow 1$. This effect is consistent with the full screening of the field near the anode and the appearance of the inactive region there.

It is apparent in Eq. ((2.37) that the CWF damping occurs for two principal reasons: (i) The damping due to the charge drift in the screened electric field represented by the parameter a and (ii) the charge trapping and recombination defined by $1/\tau$. Since both processes affect $i(t)$ in Eq. ((2.37) in the same form, the effect of space charge and carrier trapping on CWF cannot be simply detached. A smart approach must be searched for the resolution of this task. Here we suggest two independent approaches for its solution.

(A) The first method is based on an L-TCT monitoring of the space charge formation after the step-wise switch on the bias. This concept stems from the fact that the space charge is equal to zero in the detector in equilibrium at U=0 and grows only after the biasing [99]. Taking this fact into account, the damping parameter c may be measured as a function of the time delay after the biasing Δt, and τ is discovered according to the limit

$$\tau = \frac{1}{\lim_{\Delta t \to 0} c(\Delta t)}. \quad (2.39)$$

Having τ, we may easily deduce the time dependence of a and N from known c. If the polarization is ruled by a single dominant trap, the dynamics of space charge density may be described by the simple exponential law

$$N(t) = N_f \left(1 - e^{-\frac{t}{\tau_D}}\right) \quad (2.40)$$

with N_f defining the final $N(t=\infty)$ and the detrapping time τ_D correlating with the trap properties according to the Shockley-Reed-Hall model [100]

$$\tau_D = \frac{1}{v_e \sigma_e n_1}, \quad (2.41)$$

where v_e, σ_e, and n_1 are the electron thermal velocity, thermal capture cross-section and electron density in case of Fermi energy E_F being set to the deep level (DL) ionization energy, respectively. If measurements are done at variable temperature T, the obvious fit of the Arrhenius plot may be used for determining the trap energy E_T and thermally determined capture cross-section $\sigma_{e(T)}$:

$$\ln(\tau_D \cdot T^2) = \left(\frac{E_T - E_C}{k_b}\right)\frac{1}{T} - \ln(A \cdot \sigma_{e(T)}), \quad (2.42)$$

where $A=2k_b^2 m^*/(\pi^2\hbar^3)=3\times10^{21} (m^*/m_0)$ cm^{-2}s^{-1}K^{-2} with k_b, m^*, m_0 and $\hbar$ are the Boltzmann constant, effective mass of free carriers, electron mass, and Planck constant, respectively.

(B) Another approach is based on the particular dependence of t_{tr} on a in Eq. (2.38). Whenever a satisfies the condition

$$a = \frac{2U}{L^2}, \tag{2.43}$$

t_{tr} is converged to the infinity and CWF is turned into the single exponential shape. Such transformation can be identified by the measurement of the CWF shape and a may be fixed. Defining c by the fit of CWF with the single exponential function $\propto e^{-ct}$, the lifetime τ may be straightforwardly determined according to the formula

$$\tau = \frac{1}{c - \frac{2U\mu}{L^2}}. \tag{2.44}$$

While method (A) conveniently describes the detector at a high bias, the latter approach (B) is applied well at low bias where the detector charging often leads to the formation of the inactive region. The comparison of τ discovered according to Eqs. (2.39) and (2.44) affords us a convenient tool for the verification of evaluated quantities.

The detector properties evaluated according to the above scheme may be further refined by involving additional electron traps released by the electron detrapping from depleted level. These extra traps reduce τ in the polarized detector according to the formula

$$\tau = \frac{\mu e + \upsilon_e \sigma_e \varepsilon_0 \varepsilon_s}{\frac{\mu e}{\tau_0} + c\upsilon_e \sigma_e \varepsilon_0 \varepsilon_s}, \tag{2.45}$$

where τ_0 is the lifetime in the uncharged (neutral) detector. Corresponding modified a and N are given by

$$\frac{eN}{\varepsilon_0 \varepsilon_s} = a = \frac{c - \frac{1}{\tau_0}}{\mu + \frac{\upsilon_e \sigma_e \varepsilon_0 \varepsilon_s}{e}}. \tag{2.46}$$

The coupling of τ, c and σ_e in Eq. (2.45) may be moreover used for the direct determination of σ_e by means of model B, in which τ and c may be found. A simple rearrangement of Eq. (2.45) results in the formula

$$\sigma_e = \frac{\mu e \left(1 - \frac{\tau}{\tau_0}\right)}{\nu_e \varepsilon_0 \varepsilon_r (\tau c - 1)}. \tag{2.47}$$

This approach completely relies on transient measurements and may be used in experiments done at a constant temperature.

2.5.2. Charge collection process in semiconductor radiation detectors

The mobility-lifetime product, $\mu\tau$, of charge carriers in detector can be determined by the Hecht's equation. For the single carrier charge transport, the Hecht's equation can be written as

$$\mathrm{CCE} = \frac{Q}{Q_0} = \frac{\mu\tau V}{d^2}\left[1 - e^{-\frac{d^2}{\mu\tau V}}\right], \tag{2.48}$$

where CCE, Q, Q_0, d, and V are charge collection efficiency, charge induced at the device contact, total charge produced by the radiation interaction, device thickness and applied bias respectively. In the Hecht formalism a uniform electric field is assumed as a function of depth. In the case of the non-uniform electric filed the modified Hecht relation[79] is used.

3. Experimental

3.1. Samples

Basic characteristics of the samples are given in Table 4. Semi-insulating CdTe and CdZnTe single crystals No 1-8 with a zinc content of about 4% and 10% were grown at the Institute of Physics, Charles University by the Vertical-gradient freezing method. The CdTe crystals were doped either with indium or with chlorine, whereas CdZnTe crystals were undoped or doped with indium. The p-$Cd_{1-x}Mn_xTe$ sample No 9 was grown at Chernivtsi National University by the vertical-gradient freezing method with Mn content of 10%. All samples were prepared by the same approach. Samples were cut from a wafer by diamond saw and polished on an alumina powder with 1 µm grain size. Afterward, each side was chemo-mechanically polished 30 s in 3% bromine-ethylene glycol solution [101], [102]. Finally, the samples were etched in 2% bromine-methanol solution for 1 min. After each chemical treatment, the samples were rinsed in methanol and acetone. Gold contacts for measurements were electrolessly deposited [103] on a pre-masked surface in 1% aqueous $AuCl_3$ solution. Obtained crystals were rinsed in water and cleaned with acetone. PL spectra were measured on the same samples used for PHES measurements.

Table 4. Samples' data: sample number, conductivity and material type, zinc content, dopant, room temperature conductivity, Fermi energy, DL energies determined by PHES and estimated ZPL in PL, and band gap energy at 300 K.

No (Group)	Material	Zn/Mn Content (%)	Dopant	Conductivity ($\Omega^{-1}cm^{-1}$)	E_c - E_F (eV)	Band gap energy (eV)
1(I)	n-CZT	4.5	-	3.7×10^{-9}	0.61	1.549
2(II)	n-CZT	3.5	-	1.1×10^{-9}	0.65	1.544
3(II)	n-CZT	10	In	1.6×10^{-10}	0.70	1.599
4(III)	n-CT		In	1.1×10^{-9}	0.65	1.526
5(III)	n-CT		In	9.1×10^{-10}	0.65	1.526
6(IV)	p-CT		Cl	1.6×10^{-6}	1.03	1.526
7(IV)	p-CT		Cl	2.4×10^{-6}	1.04	1.526
8(V)	p-CT		Cl	3.1×10^{-8}	0.93	1.526
9(V)	p-CMT	10	-	9.1×10^{-10}	1.10	1.62

3.2. Photoluminescence

Samples were placed in the Optistat helium flow cryostat (Oxford Instruments). PL was excited by a tunable Ti:Saphire laser Millennia Pro 5sJ (Spectra Physics) measured by the Bruker IFS 66s FTIR spectrometer equipped with a CaF_2 beam splitter and a cooled InSb detector. Excitation radiation was blocked in front of the spectrometer by Semrock 808 nm edge low pass filter (1.53 eV). The strongest luminescence signal was obtained by using the excitation photon energy slightly below the region of exciton absorption, i.e. in the spectral region of the Urbach tail about 20 meV below E_G, where the absorption coefficient is of the order of 10 cm^{-1}. In this case, almost all exciting radiation penetrated inside the bulk of the sample (apart from reflectivity), and it was absorbed therein. Then a suppression of PL signal by surface non-radiative recombination was reduced and bulk transitions were revealed [19], [33]. The band gap energies relevant for

PL were determined using spectra of free and bound excitons recombination excited by 1.946 eV radiation (Radius Coherent laser) and detected by silicon photodiode in the IFS66s.

3.3. Galvanomagnetic measurements

The principle of classical Hall-effect measurements and photo-Hall effect spectroscopy are depicted in Fig. 3.1 and Fig. 3.2, respectively. Bar-like samples with typical dimensions of 2x3x12 mm^3 were used in the classical six-contact Hall-bar shape convenient for galvanomagnetic measurements. Hall-bar shape approximates the ideal geometry for measuring the Hall effect, in which the constant current density flows along the long axis (5 and 6) of a rectangular solid, perpendicular to an applied external magnetic field ***B***. The ideal six-contact Hall-bar geometry is symmetrical. Side contact pairs are placed symmetrically about the midpoint of the sample's long axis and located oppositely one another.

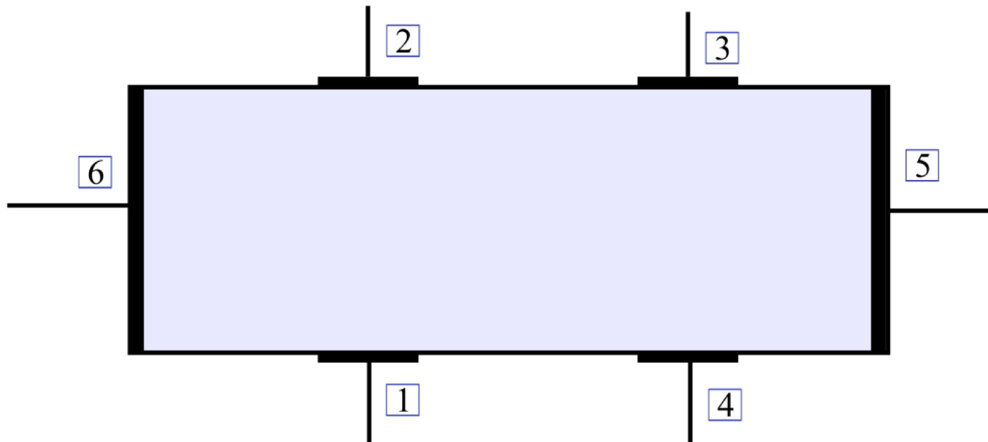

Fig. 3.1. Classical six-contact Hall-bar configuration.

This geometry allows us two equivalent measurement sets to check for sample homogeneity in both resistivity and Hall coefficient. Hall voltage contacts must be put far enough from to the sample's ends to avoid short circuit of the Hall voltage that could lead to an underestimated actual Hall coefficient. To calculate the resistivity at zero magnetic field, we first calculate the resistivity ρ_A and ρ_B measured between side contacts {2-3} and {1-4} on each side of the sample as shown in Fig. 3.1. The average value also includes different orientations of the applied current I^+ and I^-

$$\rho_A = \frac{V_{56,23}^{+} - V_{56,23}^{-}}{I_{56}^{+} - I_{56}^{-}} \frac{wd}{l} \qquad [\Omega \cdot \mathrm{cm}] \tag{3.1}$$

$$\rho_B = \frac{V_{56,14}^{+} - V_{56,14}^{-}}{I_{56}^{+} - I_{56}^{-}} \frac{wd}{l} \qquad [\Omega \cdot \mathrm{cm}] \tag{3.2}$$

Then the average resistivity is given by

$$\rho = \frac{\rho_A + \rho_B}{2} \qquad [\Omega \cdot \mathrm{cm}] \tag{3.3}$$

These two resistivities should typically agree to within ±10%. If they do not, then the sample is too inhomogeneous or anisotropic.

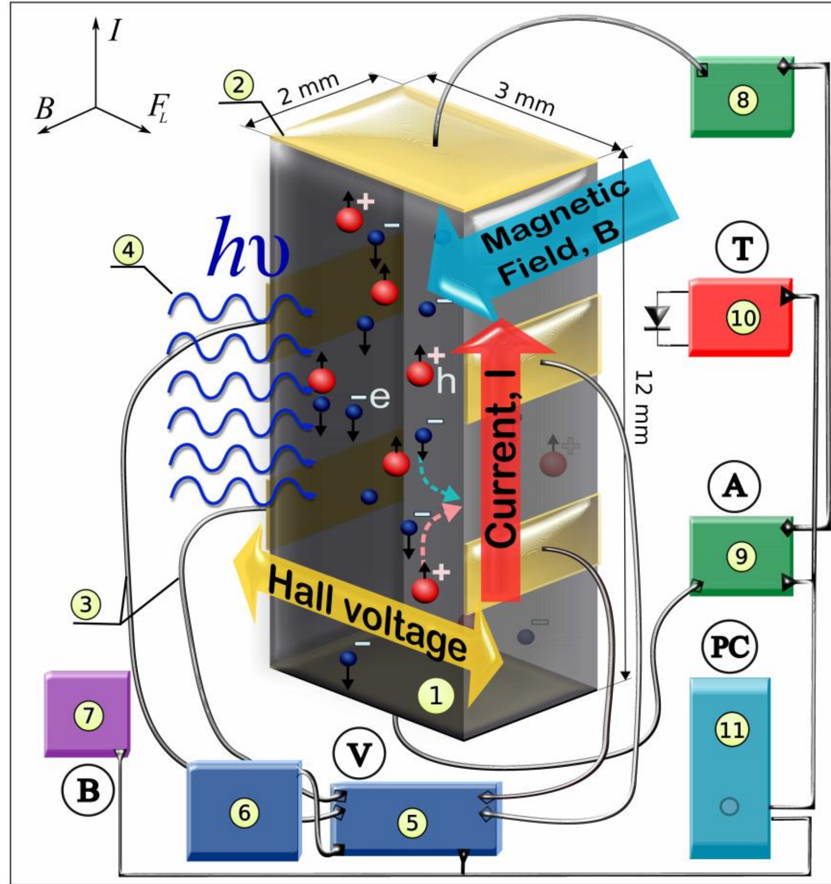

Fig. 3.2. Experimental set-up for conventional Hall effect, photo-Hall and photoconductivity measurements: 1 sample, 2 gold contacts, 3 silver wires, 4 monochromatic light, 5 switch system with Hall effect card (Keithley 7001), 6 system multimeter (Keithley 2000), 7 source for the electromagnet (15 A), 8 current source (Keithley 220), 9 picoammeter (Keithley 485), 10 GaAlAs diode for the temperature detection, 11 PC.

Hall coefficient is calculated by the same manner as an average resistivity but now the transversal Hall voltage between contacts {1-2} and {3-4} measured at different directions B^+ and $B^-$of magnetic field is taken into account:

$$R_H^A = \frac{V_{56,34}^+(+B) - V_{56,34}^-(+B) + V_{56,34}^-(-B) - V_{56,34}^+(-B)}{I_{56}^+(+B) - I_{56}^-(-B) + I_{56}^-(-B) - I_{56}^+(-B)} \frac{d}{B} \tag{3.4}$$

$$R_H^B = \frac{V_{56,21}^+(+B) - V_{56,21}^-(+B) + V_{56,21}^-(-B) - V_{56,21}^+(-B)}{I_{56}^+(+B) - I_{56}^-(-B) + I_{56}^-(-B) - I_{56}^+(-B)} \frac{d}{B} \tag{3.5}$$

and the average value of Hall coefficient is given by

$$R_H = \frac{R_H^A + R_H^B}{2} \ [\mathrm{C}^{-1} \cdot \mathrm{cm}^3] \tag{3.6}$$

Measurements were performed at room temperature with a constant magnetic field B of 1 T. The longitudinal voltage *V*, current *I*, and the transverse Hall voltage V_H were measured directly at the experiment.

3.4. Photo-Hall spectroscopy measurements

Prior to illumination, each sample was maintained in the dark for an extended period, typically 12 hours, to eliminate persisting effects of previous light exposure. The sample was then illuminated using a 100 W halogen lamp filtered through Carl Zeiss Jena quartz glass prism monochromator. All spectra were measured with a constant maximum monochromator input slit width, which yielded the wavelength dependent photon flux and consecutively normalized by the light source radiation characteristics. This approach was chosen with the aim to reduce the noise in the PHES spectra introduced by the rearrangement of the slit width at the constant photon flux measurement and exploiting nearly linear dependence of PHES signal in most situations. To fix possible deficiencies of this procedure, distinct regions of spectra were measured also in the regime with constant photon flux. It appeared that the differences between the minimum photon flux (1.2×10^{13} cm^{-2}s^{-1}) and maximum photon flux (7.2×10^{13} cm^{-2}s^{-1}) did not lead to a change in the character of the spectra. DL energies defined from these measurements did not deviate markedly from those found by using normalized flux spectra. Likewise, other systematic errors, like the monochromator tuning accuracy, temperature fluctuations, etc., did not lead to a change in the character of the spectra. The spectral resolution of the monochromator

was measured using Ocean Optics spectrometer. The resolution (defined by FWHM) grows nearly linearly from 0.01 eV at 0.5 eV up to 0.11 eV at 1.3 eV. The deep level threshold energies were identified from DWPHES spectra by monitoring μ_H and photoconductivity (PhC) spectra.

The photon flux from the conventional lamp source (halogen or Mercury) filtered by a monochromator (the common output flux < 10^{14} $cm^{-2}s^{-1}$) did not allow sufficient minority carrier generation in the energy region below the Urbach tail due to strong recombination. To overcome this obstacle we upgraded the equipment and used a more powerful white laser with a maximal filtered output photon flux of 1.3×10^{15} $cm^{-2}s^{-1}$. The laser source provides nearly constant photon flux in the 0.6 - 1.4 eV energy region which is in the most interest for deep level spectroscopy. The enhanced illumination allows separate experimental observation of both minority and majority carrier concentrations in p-type material.

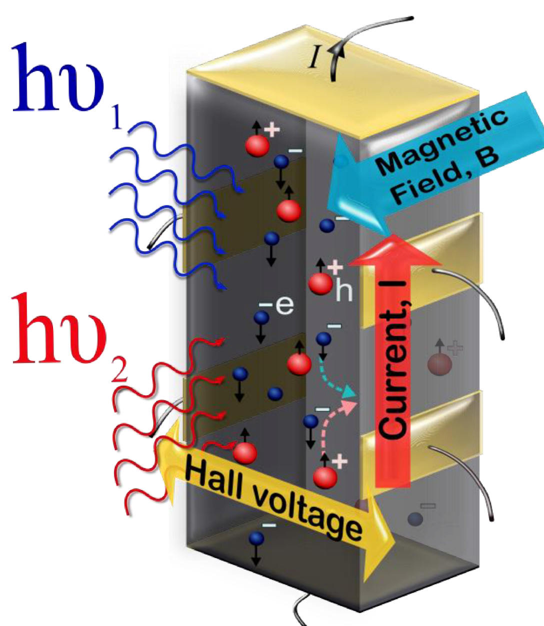

Fig. 3.3. Basic principles of DWPHES measurements.

In addition to the low-intensity excitation with the monochromator we used 0.8 eV, 0.95 eV, 1.26 eV, and 1.46 eV Thorlabs Laser Diodes with resolution 4 meV and the photon flux up to 2.5×10^{17} $cm^{-2}s^{-1}$. Fiber wavelength mixer was used to combine the two illumination sources and to provide homogeneous illumination of the sample by dual-wavelength illumination. The second source (laser diode) had the fixed photon energy and PHES spectra were measured with different monochromator

wavelengths. Basic principles of photo-Hall effect spectroscopy with dual-wavelength illumination are shown in Fig. 3.3.

The influence of the illumination on Au contacts was checked and maximal photo-voltage did not exceed one-tenth of the Hall voltage measured in PHES. DL threshold energies were identified from PHES spectra by monitoring the change of the slope of the considered curve representing the activation of generation channel.

3.5. Laser induced transient current technique

To illustrate the validity of the theoretical concepts outlined above in section 2.5, n-type sample, No 4 in Table 4, was chosen for investigation. The detector was equipped with gold contacts and the temperature dependent L-TCT measurements were performed in the steady-state and in pulsed bias. The material and detector characteristics were as follows: the detector thickness L=1.7 mm, and resistivity $\rho = 10^9\ \Omega$cm.

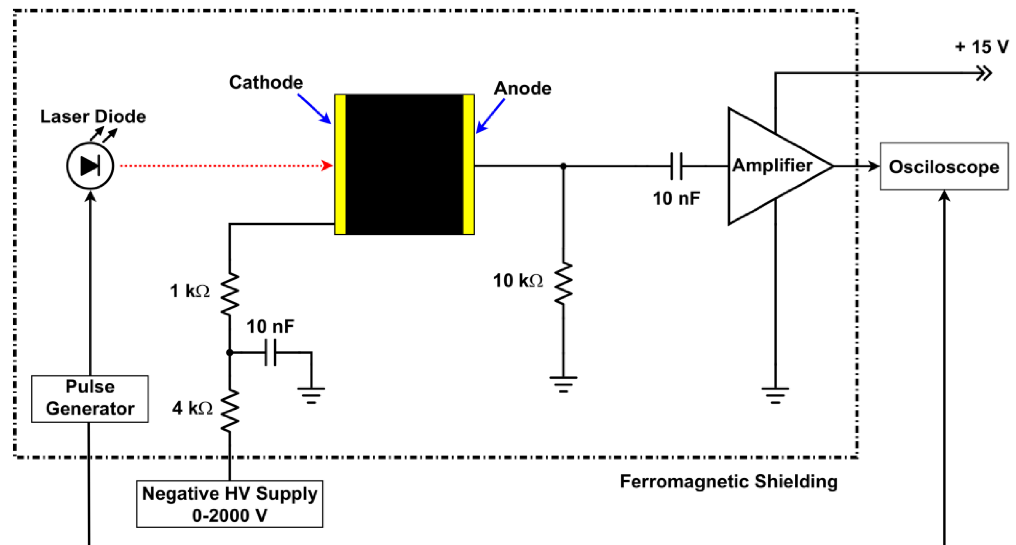

Fig. 3.4. The diagram of L-TCT setup for a transient current measurement

To generate current waveform the detector was irradiated by a laser pulse (660 nm wavelength, 2 ns pulse width as FWHM, and 3 mm^2 focal spot area) of the laser diode powered by an ultrafast pulse generator. The detailed scheme of the L-TCT apparatus is shown in Fig. 3.4. To study the space charge formation dynamics, the L-TCT setup was supplemented by an in-house constructed negative bias switching unit (5 ms rise time) driven by an arbitrary waveform generator as a master. The

generator was precisely synchronized with the laser diode pulse generator in order to enable the adjustment of a variable laser pulse time delay position within the switched-on bias interval. Pulse generator also triggers ultrafast digital sampling oscilloscope (40 Gs/s, resolution up to 11 bits, 4 GHz bandwidth) which measures the current. Arbitrarily adjustable pulse repetition rate and the bias on/off ratio were used to control the detector depolarization. In this setup, CWFs were recorded depending on the delay time Δt defined as the time interval between the bias pulse rising edge and the laser pulse occurrence.

4. Photo-Hall effect spectroscopy and Photoluminescence in n-type samples

Photo-Hall effect spectroscopy is used to study electrical properties of CdTe-based detector materials. As a result of much higher electron mobility, typically $\mu_e \approx 10\mu_h$, low hole concentration can be hardly measured by PHES in the material with dominant electron concentration[38], see 2.10 where the electron impact is proportional to the second power of the electron mobility. Therefore, results for n-type and p-type materials are discussed in chapter 4 and chapter 5 separately due to a different deep level detection approach. To enhance DL detection capabilities, PHES was further upgraded with dual-wavelength illumination for n-type samples (Chapter 4.2) and with enhanced illumination for p-type samples (Chapter 5.2).

4.1. PHES with single wavelength illumination

High resistive CdTe and CdZnTe single crystals were measured by PHES and Photoluminescence spectroscopy PL with the aim to discover the position of deep

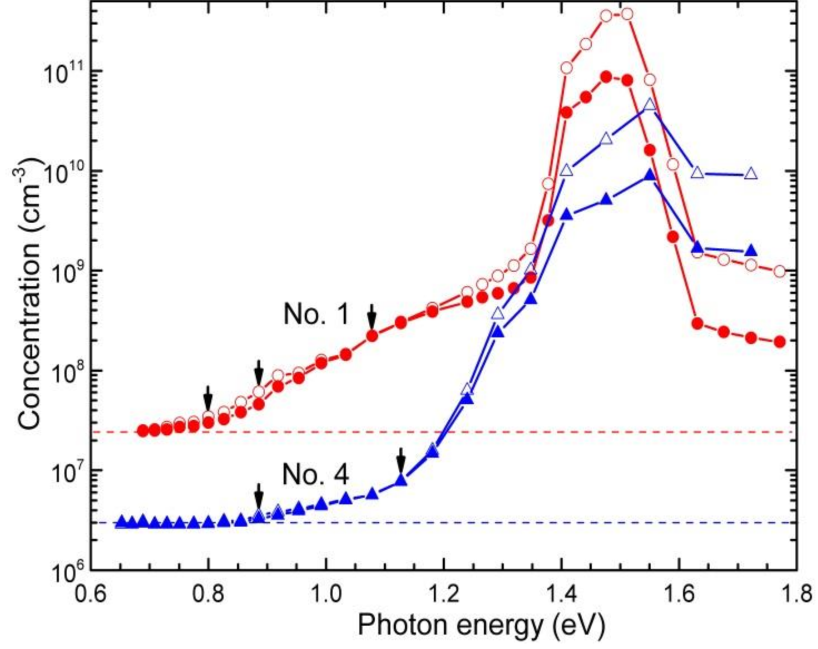

Fig. 4.1. Spectral dependence of the free carrier concentration determined by PHES for *n*-type samples No. 1 (red) and No. 4 (blue). Vertical arrows indicate DL threshold energies. The dashed lines mark corresponding dark carrier concentration. Spectra normalized to constant photon flux are shown by empty symbols.

levels in the band gap. Illumination in the range of 0.65 – 1.77 eV, room temperature, and DC electrical measurements were used in case of PHES. Low temperature (4 K) photoluminescence spectra were recorded in the spectral range above 0.47 eV. Among all *n*-type samples, groups (I) and (II) were distinguished by the set of 0.8, 0.9, 1.1 eV or by 0.8, 0.9, 1.15 eV DLs and group (III) by the 0.9 and 1.15 eV DLs absorption. Characteristic examples of PHES of samples No. 1 and 4 are shown in Fig. 4.1. The sample No. 1 with the most distinct PHES showed a strong hysteresis in the PHES measured in the loop with continuously increasing and decreasing photon energy and constant measurement rate with a delay of $\Delta t = 90$ s between single measurements. Three hysteresis loops for three different slit widths representing an incident photon flux 5.0×10^{13}, 2.6×10^{13} and 7.5×10^{12} $cm^{-2}s^{-1}$ at the central 1.13 eV photon energy are shown in Fig. 4.2**.** The characteristic time of the electron density relaxation $\tau_e \approx 60$ s was deduced from the light ON/OFF photoconductivity measurement shown in Fig. 4.3 The long lifetime of photo-induced electrons is assigned to the electron recombination on the 0.9 eV DL situated below E_F, analogous to the level E_{t1} in Fig. 2.1 with a rather low electron capture cross-section σ_e. The relaxation of

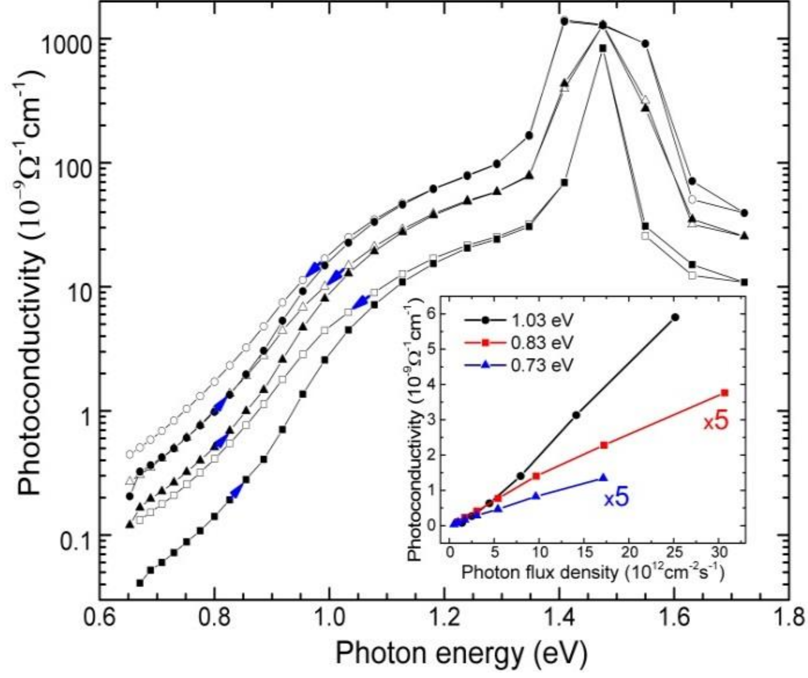

Fig. 4.2. Hysteresis loops of photoconductivity for the CdZnTe *n*-type sample No. 1. Full and open symbols show the spectra measured from low-to-high and high-to-low photon energies, respectively. The inset shows the PhC dependencies versus photon flux at 0.73, 0.83 and 1.03 eV photon energies. Curves for 0.73 eV and 0.83 eV were multiplied by a factor of 5.

the photoconductivity can be used for the determination of σ_e of the excited DL. The kinetic equation describing the electron relaxation after the switch of the excitation can be expressed as

$$\frac{\partial n}{\partial t} = -\sigma_e \nu_e n(N_t - n_t) \tag{4.1}$$

where ν_e, N_t, and n_t are the thermal velocity of electrons, total DL density and the electron density on the level, respectively. Assuming electrons previously excited exclusively from the single DL, which was completely filled by electrons in the dark, the charge neutrality requests to fulfill the clause

$$n - n_{00} = N_t - n_t \tag{4.2}$$

where n_{00} is the electron density in the dark. Substituting Eq. 4.2 into
Eq. 4.1 we may obtain the solution of Eq. 4.1 in the form

$$n = \frac{n_0 n_{00}}{n_0 + (n_{00} - n_0)e^{-\sigma_e \nu_e n_{00} t}} \tag{4.3}$$

with n_0 being the initial electron density at $t=0$. Inasmuch as electron density parameters n_0 and n_{00} are defined by the experiment and ν_e is given by well-known

formula [34], σ_e remains the only parameter to be optimized in the fit of the PhC relaxation. The single parameter fit shown in Fig. 4.3 revealed $\sigma_e = 1.7 \times 10^{-17}$ cm^2. The fact that the fit resulted in

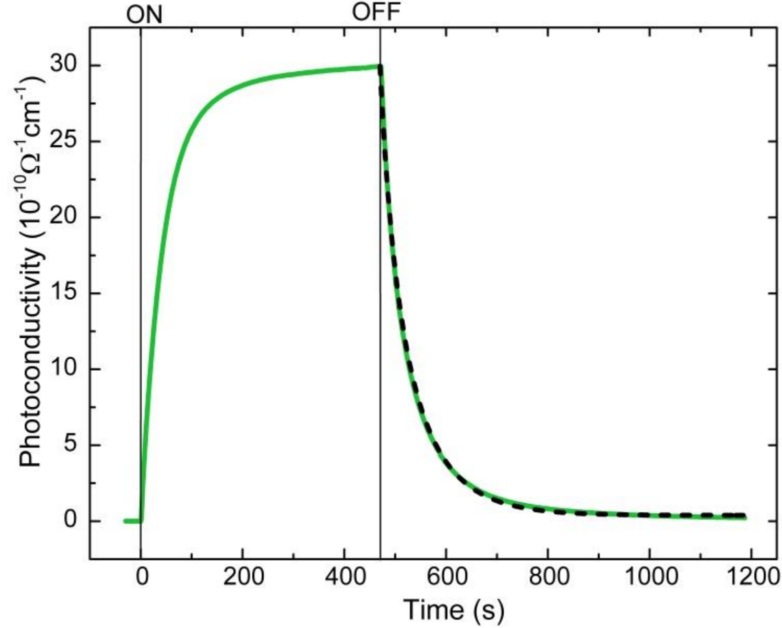

Fig. 4.3. The PhC relaxation after illumination at 0.89 eV for 500 seconds measured in sample No 1. The dashed line is the fit according to the presented model.

such a good agreement with experiment endorses the high validity of the model. The possibility to study transitions between this or similar DLs and the conduction band by PHES brings an important piece of knowledge on their properties.

The DLs energies $E_C - 0.9$ eV and $E_C - 0.8$ eV accord with the energy of a hole trap with the trapping energy $E_{th} = E_g - E_{te} \approx 0.7$ eV, which is close to often detected hole trap in radiation detectors, 0.64 eV [95] and 0.76 eV [104], identified as a principal DL responsible for polarization phenomena [25], [30]. Determination of σ_e of hole trap levels localized below the middle of the band gap is unfeasible in thermal excitation techniques where the strong interaction of hole trap with the valence band disables an effective exchange of electron between DL and conduction band. An analogous statement may be formulated for the electron traps as well. In contrast to 0.8 eV and 0.9 eV DLs the third level characterized by the energy of 1.1 eV did not reveal the hysteresis in the discerned time scale.

The DLs placed near the middle of the band gap may be definitely assigned to the defect model No 1 shown in Fig. 2.1. The description with an alternative model No 2 fails due to the proximity of pertinent DL to E_F, and its significant electron

occupancy. Such DL would cause a principal growth of the photoconductivity even at the lowest photon energies below $E_g/2$. Though the slight increase of the PhC at 0.65 eV apparent in Fig. 4.1 indicates an existence of another less distinctive DL near E_F at the energy Ec - 0.65 eV, the magnitude of the PhC increase is too low to support the validity of defect model No 2. Similar arguments were used in the interpretation of DLs in the samples of group (II).

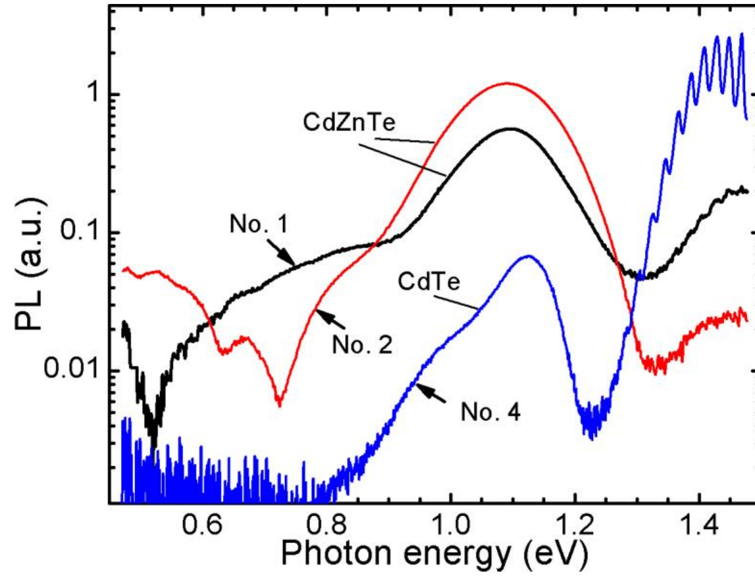

Fig. 4.4. PL spectra representing DLs transitions in CdZnTe and CdTe *n*-type samples. Affiliation of each curve is labeled by a number from the Table 4.

In agreement with PHES, the measurement of PL shown in Fig. 4.4 for sample No. 1 confirms the presence of several deep levels in the 0.6 – 0.9 eV region [105]. Zero-phonon lines (ZPL) approximately corresponding to the difference of energies of excited and ground states without atomic rearrangement are placed in PL spectra well above the PL band maximum in the high-energy tail of the PL band [33], [106]. Estimated ZPL positions of the most pronounced bands are indicated in Attachments Table A where all DL data are summarized. The peak DLs energies deduced from PL spectra can deviate from the real value due to phonon replica structures at low temperatures (see Fig. 4.5) , the dependence of band gap [106] and DL energies per se on temperature, and nature of the defect. The estimated value of these deviations is ~ 0.1 eV [33], [107].

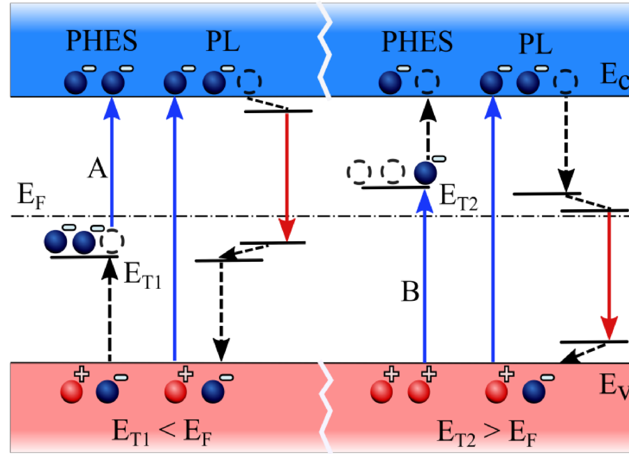

Fig. 4.5. The basic defect model with pondered transitions. Blue upward arrows delineate principal optical excitation, dashed black arrows show thermally activated transition (or supplementary optical transitions) in the PHES and carrier capture with lattice relaxation in the PL measurement. The red downward arrows represent the radiative recombination detected by PL.

In case of absent information on holes, PHES does not allow us to simply determine the type of the level significantly deviating from the midgap region. The level position either below E_F inducing direct electron transitions to the conduction band or above E_F with electron excitation from the valence band to the level and consecutively combined thermal and optical excitation to the conduction band outlined in Fig. 2.1 should be considered. We interpret all dominant transitions in n-type samples characterized by an energy ≈ 1.1 eV by the defect model No 1 with DL energy at E_C - 1.1 eV. Such result concerts with experimental data [27] while no pertinent level was found in the antipodal part of the band gap E_V + 1.1 eV (see Table 2).

4.2. PHES with dual-wavelength illumination

4.2.1. Unusual Hall mobility and Photoconductivity decrease

A single sample No 1 (Table 4) characterized by multiple unusual features like negative differential photoconductivity and anomalous depression of electron

mobility, see Fig. 4.6**,** was chosen for the detailed study involving measurements at both the steady and dynamic regimes. The electron lifetime, $\tau_e \approx 120$ ns was

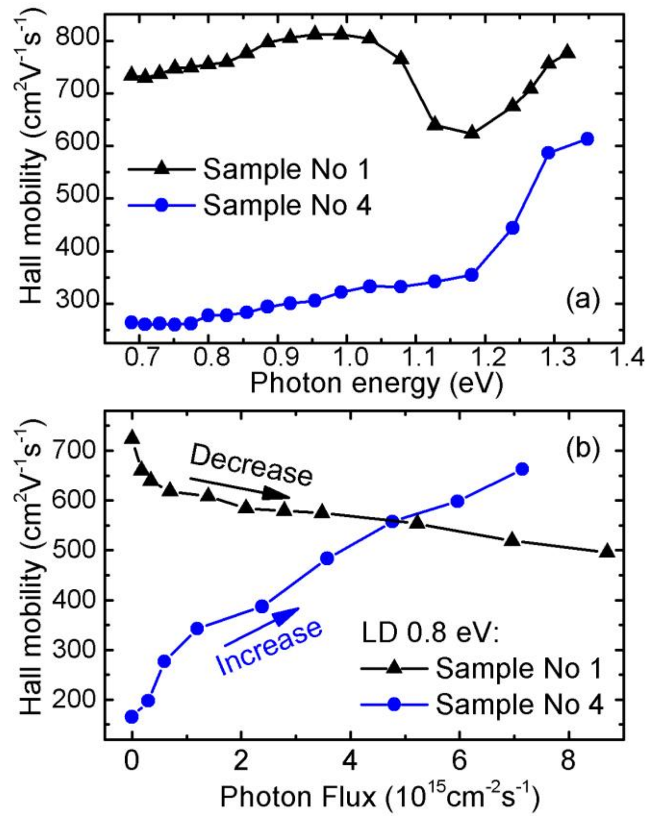

Fig. 4.6. Hall mobility spectra (a) and Hall mobility versus photon flux (b) at 0.8eV photon energy measured in samples No 1 (unusual behavior) and No 4 (common behavior).

measured by L-TCT [99] in a pulsed bias regime where 5 ms voltage pulse allowed us to overcome the polarization of the device. Rather low electron mobility-lifetime product $\mu_e\tau_e \approx 10^{-4}$ cm^{2}V^{-1} was determined by the Hecht equation fit according to Uxa et al. [108].

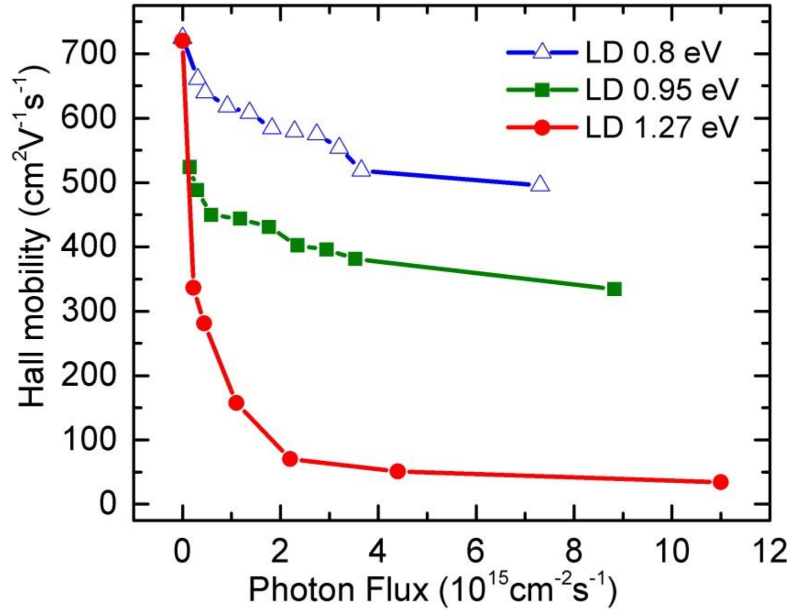

Fig. 4.7. Hall mobility versus laser-induced photon flux at 0.8, 0.95 and 1.27 eV photon energy.

In contrast to common high resistive detector grade CdZnTe and CdTe samples, where the illumination habitually induces an enhancement of the Hall mobility [109], chosen CdZnTe sample subjected to an extensive illumination showed an anomalous decrease of μ_H, see Fig. 4.6 and Fig. 4.7. Further investigation of the sample showed that PhC intensity dependencies (PhC $\propto I^{\alpha}$) reveal both superlinear regions [110] with $\alpha > 1$ at low photon flux < 10^{13} $cm^{-2}s^{-1}$ at 1.0 eV photon energy and sublinear regions [111] with $\alpha < 1$ at energies of 0.7, 0.8, 0.95, and 1.27 eV, see Fig. 4.8. Negative differential photoconductivity [69] was observed at 1.27 eV LD illumination with the photon flux above $5x10^{14}$ $cm^{-2}s^{-1}$. Simultaneously, an increasing noise of the signal represented by error bars in Fig. 4.8 (a) appeared.

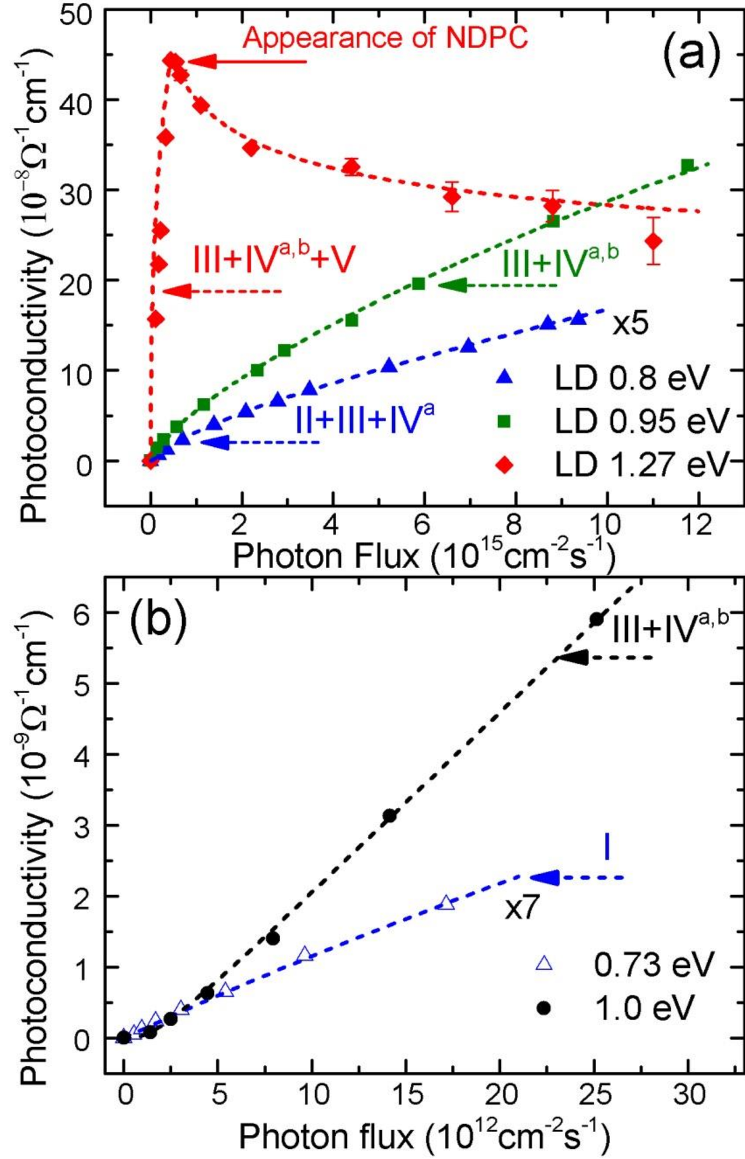

Fig. 4.8. PhC as a function of the high **(a)** and low **(b)** photon flux at 0.73, 0.8, 0.95, 1.0 and 1.27 eV photon energies (hυ). The dashed curves show the fit with the SRH model discussed in the text with parameters in Table 5. The error bars appear only if standard deviation exceeds a symbol size. Roman numerals designate respective transitions defined in the deep levels model responsible for photoconductivity rise produced by free carriers generation.

4.2.2. Deep level detection

To discover the reasons of the above-mentioned effects (shown in section 4.2.1) as well as low $\mu_e\tau_e$ and fast detector polarization [25], we have performed extensive DWPHES measurements in various regimes of simultaneous single and two-photon

illumination. Fig. 4.9 shows μ_H without and with an additional laser diode illumination. One can see threshold points near 0.75, 0.9, 1.0 and 1.2 eV in the spectra for all illumination regimes. In case of single wavelength illumination shown in Fig. 4.9(a), μ_H increases at 0.75 eV, 0.9 eV, and 1.27 eV photon energies. A significant decrease in μ_H can be observed after hυ >1.0 eV, region $IV^{a,b}$+III.

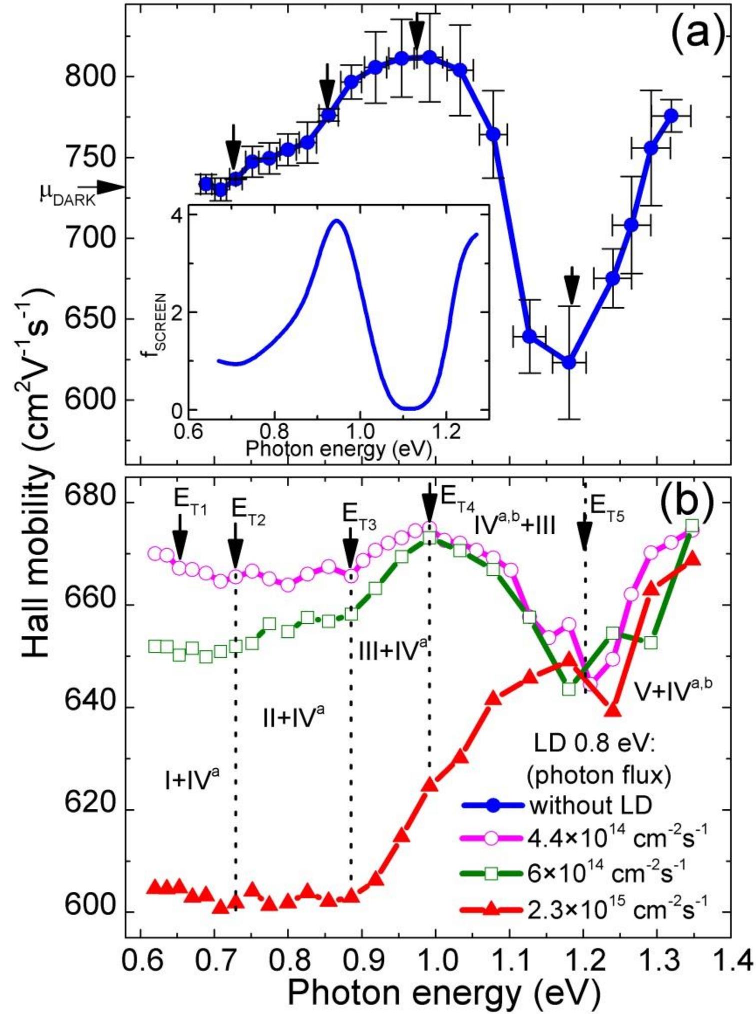

Fig. 4.9. Hall mobility spectra. Upper panel (a) shows PHES obtained without laser diode illumination. Bottom panel (b) gives plots of μ_H obtained by simultaneous illumination with monochromator and 0.8 eV laser light of different intensity. Vertical arrows indicate deep level threshold energies. The vertical and horizontal error bars represent standard deviation and monochromator experimental error, respectively. Roman numerals indicate energy regions representing different generation-recombination processes discussed later on. The inset picture shows a screening coefficient.

Similar effects are also seen after additional laser diode 0.8 eV illuminations, where in addition μ_H is suppressed below 0.9 eV. The spectrum without laser diode illumination appeared noisier than that with a laser diode, as denoted by vertical error bars in Fig. 4.9(a). Stabilization of the Hall voltage by additional laser illumination can be the keystone of this method, which can allow the Hall signal measurements not only in detector grade samples but also in the poorer quality ones.

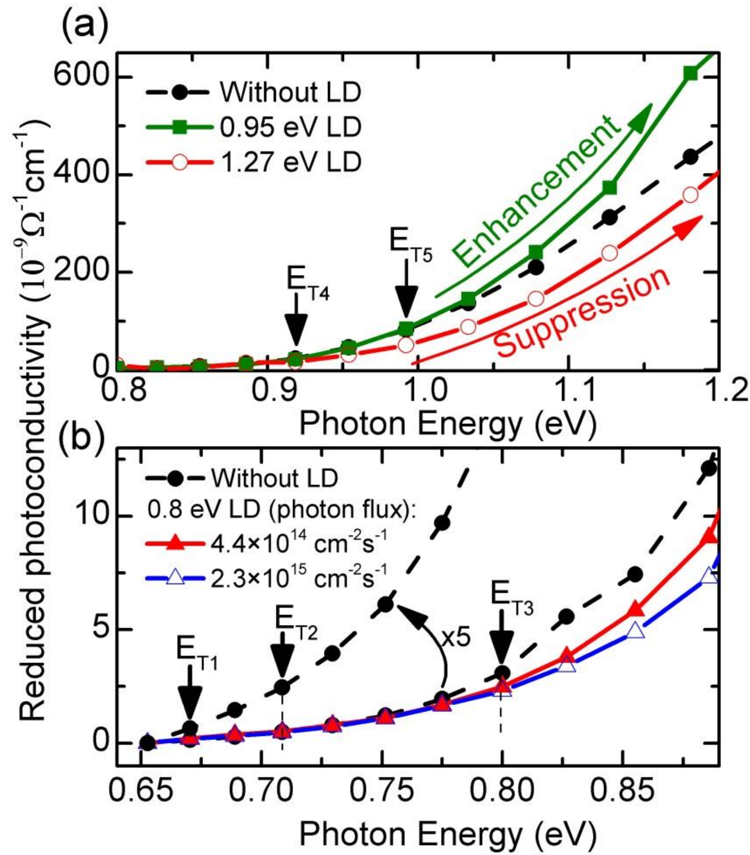

Fig. 4.10. Reduced photoconductivity spectra with the additional LD illumination at (a) 0.95 eV, 1.27 eV and (b) 0.8 eV. Black dashed curves with full bullets show spectra without additional illumination. Corresponding LD intensities were chosen to show best the effect of reduced PhC enhancement and suppression.

A comparison of conventional PhC, σ_M, and PhC with additional laser diode illumination may be used for the identification of DLs position relatively to respective bands. With this aim, we define a reduced photoconductivity $\sigma_R = \sigma_{M+LD} - \sigma_{LD}$, where σ_{M+LD}, and σ_{LD} are the photoconductivities under simultaneous monochromator and laser illumination, and PhC produced by purely laser illumination, respectively. In this way σ_R and σ_M can be compared on the same

scale. Respective results are summarized in Fig. 4.10. While a suppression of σ_R is observed in case of PhC after additional 0.8 eV or 1.27 eV laser diode illumination as an obvious consequence of the depletion of related DLs labeled E_{T2}, $E_{T3,}$ and E_{T5} in the defect model, the 0.95 eV laser diode illumination gives an enhancement of σ_R. We interpret this fact by a synergism of the excitation processes involving E_V to E_{T4} level transition at the energy of 1.0 eV and the E_{T4} to E_C transition. Consequently, while DLs energies E_{T2}, $E_{T3,}$ and E_{T5} are counted relatively to the conduction band, E_{T4} is expressed relative to the valence band. It is important to note here that another

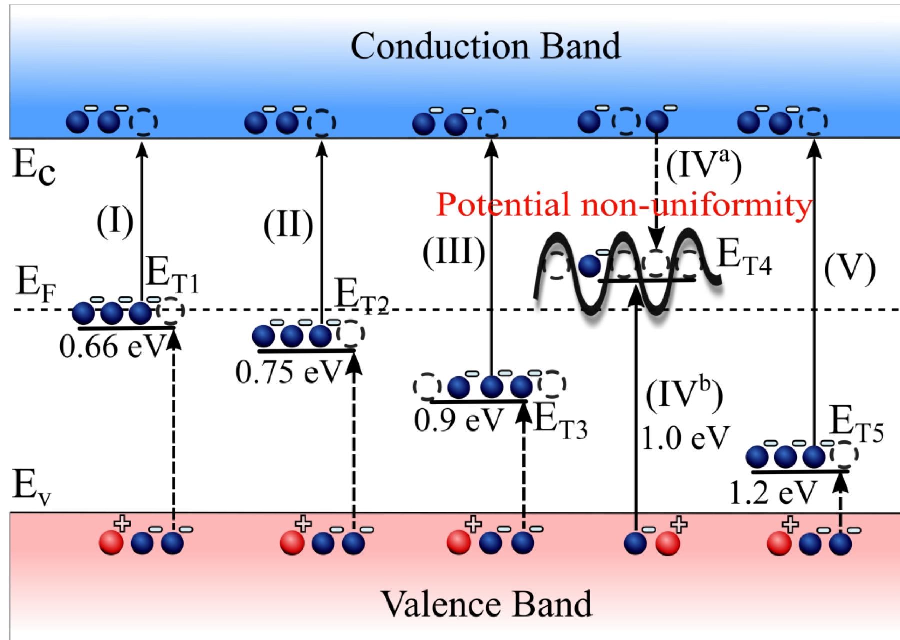

Fig. 4.11. The defect model of sample No 1 with outlined transitions. Full upward arrows delineate principal optical excitation, dashed arrows show thermally activated transitions (or supplementary optical transitions). The photon energies represent threshold energies defined by experiment. In case of upward arrows, Roman numerals show electron (hole) generation process activated by the photon energy $h\nu>E_T$. A downward arrow with IV^a numeral represents electron capture process on the E_{T4} level associated with potential non-uniformities. Same Roman numerals are used in the discussion to indicate processes involved in generation (recombination) of free carriers.

possibility of deep level positions in the band gap fails. The superlinear behavior, the same as the enhancement of the reduced photoconductivity at 0.95 eV, can't be reached by the level below Fermi energy. Such level must create positive charged

potential non-uniformities but in the n-type material the concentration of the minority holes is negligible. Hence this possibility is unlikely. Less impact from these DLs transitions is also observed in Fig. 4.9, where the value of μ_H in the region II+IV^a is suppressed and maximum rises of μ_H in the regions III+IV^a and V+IV^{a,b} are smaller in comparison with the spectra without laser diode illumination. The impact of DL E_{T1} on PhC remains untouched, mainly because of the nearly linear character of PhC vs photon flux apparent in Fig. 4.8(b) at 0.73 eV. The position of this level may be uniquely allocated relatively to E_C as it is observed below the middle of the band gap excitation, where an opposite transition could not influence the electron density [48].

4.2.3. Theoretical simulations and negative differential photoconductivity

Experimental results presented in Figs. 4.7-4.10 completed by given $\mu_e\tau_e$ were incorporated into the simulations within the five-level scheme outlined in Fig. 4.11. Parameters $\sigma_{e2} = 2\times10^{-17}$ cm^2, $\sigma_{e3} = 1.7\times10^{-17}$ cm^2, $\sigma_{e5} < 10^{-16}$ cm^2 were estimated from PhC transients measured on this sample [48]. For simplicity, deep level E_{T4} was considered as the level of an effective density N_{T4}. The fit of PhC is shown by dashed lines in Fig. 4.12 where PhC was defined as PhC = $e\mu_H(n-n_0)$. We treated the Hall mobility, concentration, and photoconductivity as effectively representing mean values through the sample. The electron mobility shown in Fig. 4.7 was used in the fit. First of all we found superlinear and sublinear behaviors of PhC that delimitated parameters of the deep levels E_{T3} and E_{T4}, Fig 4.8(b) curves LD 0.95 and 1.0 eV. Secondly, the shape of NDPC shoulder was obtained at high flux 1.27 eV illumination, which defined the parameters of level E_{T5}. The $\sigma_e \cdot N_{T1}$ product could be estimated from the electron lifetime obtained from pulsed L-TCT. The last step was the variation of the parameters to obtain a qualitative fit with all of the curves simultaneously. The parameters resulting from the fit are given in Table 5. Due to the lack of information about the levels E_{T1} and E_{T2} some parameters can vary over a wide range without an influence on the fit. Those values are not presented in the table.

Table 5. Parameters of the DLs model (sample No 1).

DL	E_{T1}	E_{T2}	E_{T3}	E_{T4}	E_{T5}
Position in the bandgap, eV	Ec – 0.66	Ec – 0.75	Ec – 0.9	E_V + 1.0	Ec – 1.2
N_t, cm^{-3}	10^{14}	10^{12}	10^{14}	3×10^{13}	10^{15}
σ_e, cm^2	3×10^{-15}	2×10^{-17}	1.7×10^{-17}	4×10^{-20}	10^{-14}
σ_h, cm^2	10^{-15}	-[a]	10^{-17}	10^{-18}	8×10^{-15}
$\tilde{\alpha}_{ei}$, $10^{-17}cm^2$	470[b]	5	2.9	16	30
$\tilde{\alpha}_{hi}$, $10^{-17}cm^2$	-	7	22	2.4	10
PhC character	Sub.[c]	Sub.	Sub.	Sup.	Sub.

[a]The values can vary over a wide range without an influence on the fit.

[b]The values of $\tilde{\alpha}_{ei}$ and $\tilde{\alpha}_{hi}$ are given correspondingly at the 0.73, 0.8, 0.95, 1.0, and 1.27 eV illumination energy.

[c]Sub./Sup.=Sublinear/Superlinear.

SRH model simulations of the photoconductivity spectra with single and dual illumination regimes with parameters from the Table 5 are presented in Fig. 4.12**.** The suppressed and enhanced curves obtained by additional illumination follow a similar course as the experimental spectra in Fig. 4.10**.** Despite a good correlation, theoretical curves have a slightly different shape in the region $h\nu > 1.0$ eV. This can be explained by increased absorption in the region near the Urbach tail which is commonly observed in CdZnTe [19].

The prominent achievement was reached at the identification of deep level responsible for the drop of μ_H presented in Fig. 4.9. This effect is explicitly joined with the excitation of the deep level E_V+1.0 eV labeled by IV in Fig. 4.11. Deep level E_{T4} is assumed to be acceptor so that it charges negatively with the electron filling.

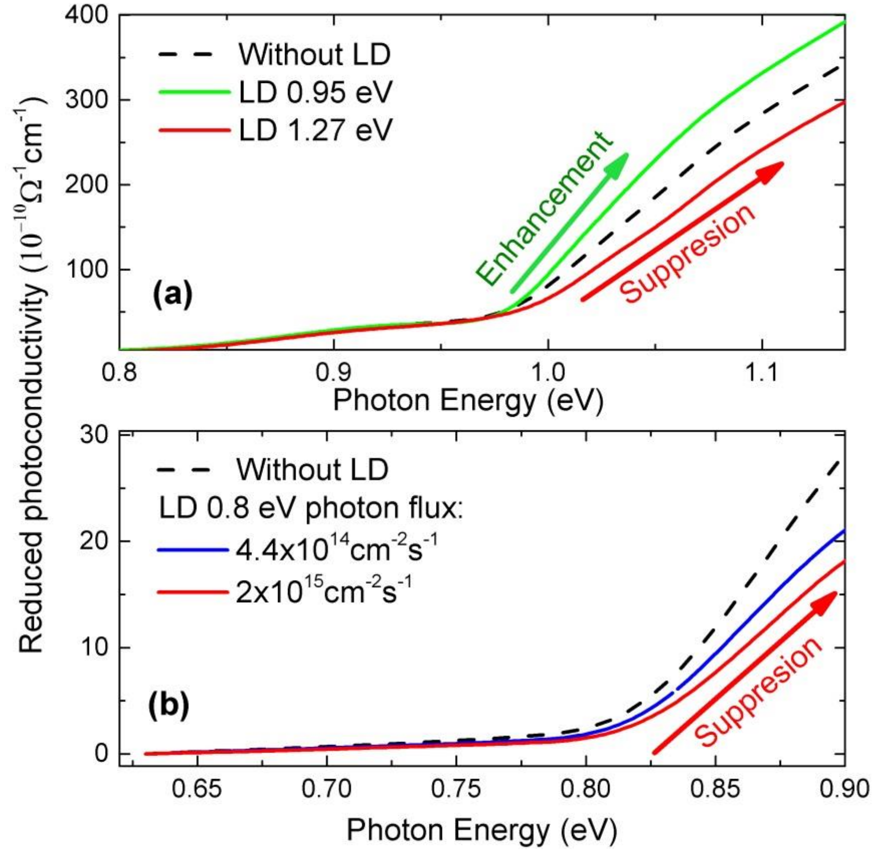

Fig. 4.12. Reduced photoconductivity spectra with the additional laser diode illumination at (a) 0.95 eV, 1.27 eV and (b) 0.8 eV obtained by SRH theoretical simulation with parameters from Table 5. Black dashed curves show theoretical spectra without additional illumination.

Electrons occupying the deep level E_{T4} produce negatively ionized charge (Fig. 4.11 IV^a and IV^b) and create Coulomb potential non-uniformities [112] (CPNUs). We explain such correlation by a nonhomogeneous spatial distribution of defects on this level. Its charging entails a formation of CPNUs [113], which consequently influence the carriers transport [114]. We assume that the bulk of the sample may be divided into two regions as outlined in Fig. 4.13. Region 1 contains the level E_{T4} with abundant density, in contrast to region 2 with E_{T4} level suppressed density. While the level E_{T4} is nearly empty in the dark and related CPNUs and bands warping are small, the optical excitation results in the level E_{T4} filling and due to its nonhomogeneous distribution the CPNUs increase entailing observed μ_H reduction. Relevant model of the Hall and photo-hall effects in inhomogeneous materials was theoretically elaborated in Ref [78] and our findings agree well with that concept, see Fig. 3 in Ref [78]. Let us note that the explanation of the μ_H

depression by other contingent models fails. The μ_H limitation caused by the enhanced ionized impurity scattering is irrelevant at room temperature and ionized defect density significantly below 10^{17} cm^{-3}, where μ_H is dominantly limited by the optical phonon scattering [115]. Similarly, the effect of holes on the μ_H reduction may be excluded due to the character of DWPHES signal, where an indication of sign conversion was never detected.

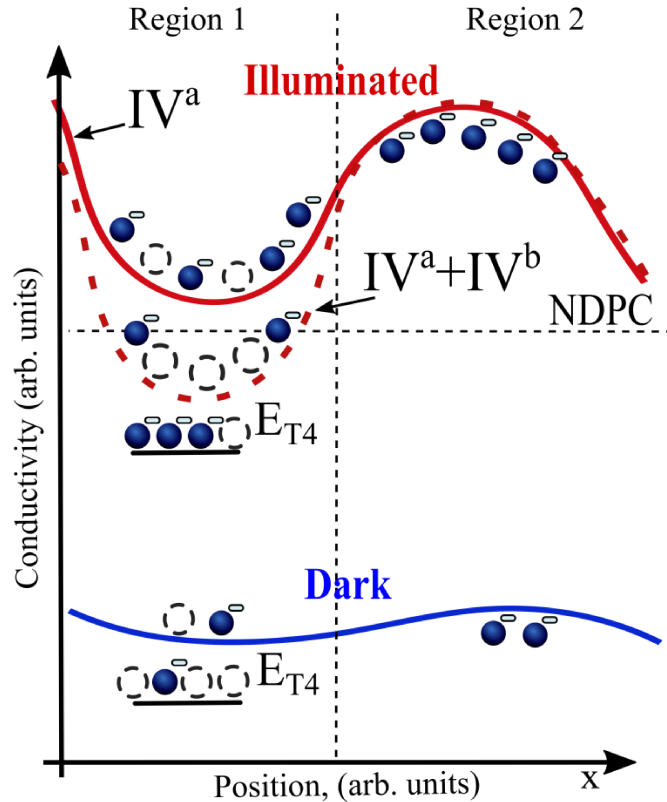

Fig. 4.13. Schematic diagram of nonhomogeneous conductivity distribution in the sample at different illumination regimes. Region 1 and Region 2 present parts of the sample with and without deep level E_{T4}. Electrons and empty circles show a relative change of carrier concentration in the conduction band and on the DL E_{T4}. Roman numerals indicate processes in Fig. 4.11**,** which lead to the occupation of the level $E_{T4.}$ Dashed line outlines the scheme of NDPC induced by relative electron depletion in Region 1 at high excitation intensity.

The enhancement of the Hall mobility occurs as a result of the compensation or screening of CPNU [112] by producing compensating charge on other DLs: E_{T1}, E_{T2}, E_{T3} and E_{T5}. The mechanism may be visualized by defining a screening coefficient

$f_{SCREEN}=n^{*}/n_{t4}$, which weighs the screening of the Coulomb interaction expressed by an effective concentration of the screening charge [116] $n^{*} = n + p + \sum_{1}^{5} n_{ti}(1 - n_{ti}/N_{ti})$ and by the charge density n_{t4} on the E_{t4} DL responsible for CPNUs. Increased n^{*} enhances μ_H, which is damped by the population of E_{t4} DL. The shape of f_{SCREEN} follows well the course of μ_H, see the inset in Fig. 4.9(a). The mobility enhancement in regions II+IV^{a}, III+IV^{a} and V+IV^{a,b} points to the presence of the DLs with threshold energies E_C - E_{T2}= 0.75 eV, E_C - E_{T3} = 0.9 eV, and E_C - E_{T5} = 1.2 eV. The μ_H depression at the high intensity LD of 0.8 eV illumination apparent in Fig. 4.9(b) is explained by the E_{T4} population via a transfer of electrons from E_{T1} or E_{T2} DLs according to the scheme $E_{T(1)2} \Rightarrow E_C \Rightarrow E_{T4}$ and by absorption of two photons by an excitation from the valence band through E_{T1} or E_{T2} DLs $E_V \Rightarrow E_{T1(2)} \Rightarrow E_C \Rightarrow E_{T4}$. Let us note that weak depletion of DLs localized below E_F results in an enlarged screening while a significant depletion of these levels with $n_{ti}<N_{ti}/2$ damps the screening oppositely.

As it was shown in Ref [78], the distinction of variations of n or μ is distinguishable in inhomogeneous materials and an attempt to derive right n or μ spatial distribution based on Hall data is not accessible. The appearance of NDPC points to the abnormality in the sample's defect structure leading to redundant carrier recombination and deterioration of the detection properties of CdZnTe. The negative differential photoconductivity has not yet been reported in CdZnTe. In our measurement the NDPC was not observed at the energies $h\nu$ < E_{T4}-E_C, see Fig. 4.8. At the same time the Hall mobility decreases monotonically at all enhanced fluxes, see Fig. 4.7. This effect can be explained by two different processes, which lead to filling of the level E_{T4}. The process IV^{a}, see Fig. 4.11, dominates at the $h\nu$ < E_{T4}-E_C and the increase of the free carrier concentration has a stronger influence on the photoconductivity than the decrease of mobility. The second generation channel is activated at $h\nu$ > E_{T4}-E_C photon energies, which results in the increased DL E_{T4} filling. Meanwhile, deep levels below Fermi energy are largely depleted from electrons due to intensive photo-excitation and the electron density decreases in Region 1, see Fig. 4.13. These two simultaneous events are described schematically in Fig. 4.13 by the transition labels (IV^{a} + IV^{b}) defined in Fig. 4.11. Interestingly, the photon capture probability of process IV^{a} is higher than of IV^{b} channel, $\tilde{\alpha}_{e4} > \tilde{\alpha}_{h4}$ see

Table 5. It results in the increase of PhC at relatively low photon fluxes ($I_{ph} < 8\times10^{14}$ $cm^{-2}s^{-1}$) at 1.27 eV illumination changing to NDPC at the high enough intensity.

4.3. Chapter summary

We have detected by PHES four DLs in n-type samples: (a) $E_c - 0.65$ eV (b) $E_c - 0.8$ eV, (c) $E_c - 0.9$ eV, (d) $E_c - (1.10\text{-}1.15)$ eV. All energies agree well with those identified by PL. The 1.30 and 1.35 eV DLs discovered by PL could not be identified by PHES due to the strong absorption by A-centres and by Urbach-type states [19]. Energies (b), (c), and (d) are also in agreement with [105]. For the placement of levels (a), (b), (c), and (d) the most effective approach appeared the comparison of detected transition energies with E_F, which allowed us unique assignment of the transition to the defect model No 1 or No 2 in Fig. 2.1. It is important to note that DLs located in close proximity to the Fermi level can change recombination channels by pinning E_F under high photon fluxes. The activation of additional recombination channels inevitably leads to the improper operation of the optoelectronic device [38].

The DL structure was further refined for sample No 1 by DWPHES using the monochromator excitation in the photon energy range 0.65–1.77 eV complemented by a laser diode high-intensity excitation at selected photon energies. We revealed that the Hall mobility and photoconductivity can be both enhanced and suppressed by an additional illumination at certain photon energies. The anomalous mobility decrease was explained by an excitation of the inhomogeneously distributed deep level at the energy Ev+1.0 eV enhancing thus potential non-uniformities. The appearance of negative differential photoconductivity was interpreted by the intensified electron occupancy of that level by a direct valence band-to-level excitation. Modified Shockley-Read-Hall theory was used for fitting experimental results by a model comprising five deep levels. Properties of the deep levels and their impact on the device performance were deduced. The DL E_C-0.66 eV is responsible for low $\tau_e \approx 120$ ns of the free electron. It participates in the high-intensity excitation at 0.8 eV causing the population of E_{T4} (E_V+1.0 eV). Electron traps E_{T3} and E_{T1} are responsible for the polarization of the detector. DL E_{T3} (E_C-0.9 eV) is populated at similar energy as the hole trap E_{T4} and both DLs have similar concentrations. The DL E_{T4} is nearly unoccupied by electrons in the equilibrium and it becomes

negatively charged after the electron filling. Electron occupancy of this DL yields in the μ_H decrease. On the contrary, DLs E_{T2} (E_C-0.75 eV), E_{T3} (E_C-0.9 eV), and E_{T5} (E_C-1.2 eV) are nearly completely occupied in the equilibrium. They induce sublinear behavior of PhC. These DLs induce the μ_H restoration. Both suppression and enhancement of μ_H in the regions II+IV^a and III+IV^{a,b} are caused by the charge redistribution. The effects were successfully fitted by the developed DLs model. DWPHES allows us to clarify and reinterpret DLs detected by conventional PHES measurements, where DLs with threshold energies 0.66 and 0.75 eV, 1.0 and 1.2 eV were interpreted as two DLs with respective energy 0.8 eV and 1.15. NDPC was explained by the decrease of electron mobility caused by CPNUs, which dominates above the increasing electron concentration. Due to the saturation tendency of *n* at high illumination fluxes and the photon flux-induced CPNUs resulting in the decrease of effective electron mobility, a sharp suppression of PhC was seen at the photon flux 8×10^{14} cm^{-2}s^{-1}. The fitted shoulder to NDPC coincides with experimental data.

5. Photo-Hall effect spectroscopy and Photoluminescence in p-type samples

P-type semiconductor samples were studied by PHES measurements to reveal their DL structure. Chapter 5.1 shows limitations of PHES with a conventional illumination source (typically < 10^{14} cm^{-2}s^{-1}). In Chapter 5.2 PHES with enhanced illumination is presented which allows extending PHES DL detection capabilities.

5.1. PHES with conventional illumination sources in p-CdTe

Typical PHES spectra of measured *p*-types excited with monochtomator at low photon flux, $I = 7\text{x}10^{13}$ cm^{-2}s^{-1}, are plotted in Fig. 5.1. The group (IV) samples were characterized by higher conductivity and they did not revert to the *n*-type even at the highest accessible optical excitation; the group (V) sample changed the sign of R_H at the monochromator excitation above 1.35 eV. The PHES spectra of group (IV) and (V) samples are shown correspondingly in the top and bottom panels in Fig. 5.1. For all *p*-type samples very weak hysteresis effects were observed.

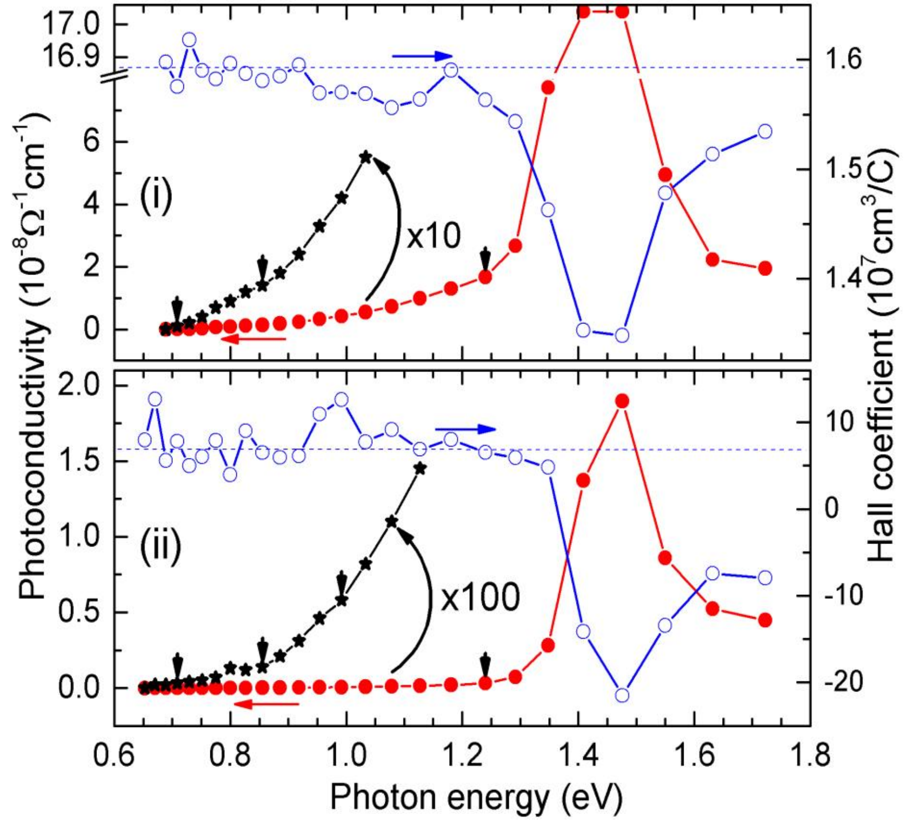

Fig. 5.1. Spectral dependence of R_H (empty bullets) and PhC (full bullets) of *p*-type samples No. 7 and 8, plotted in the upper part (i) and the bottom part (ii), respectively. The dashed lines mark R_H in the dark. For better visualization, the stars show the parts of PhC curves 10× or 100× enhanced. Vertical arrows indicate DL threshold energies.

The analysis of PhC with respect to the defect models in Fig. 2.1 allowed us the direct assignment of model No 2 with DLs localized above Fermi energy E_v + 0.7 eV and E_v + 0.85 eV to the transitions in both groups. Model No 1 is excluded because E_F is situated below the midgap region and concerned DLs are nearly electron-free in the dark. More detailed inspection, however, raises doubts on a straightforward interpretation of transitions with energies well above $E_g/2$ by model No 2. The reason stems from pretty unconvincing properties of pertinent DLs, which impeach this model. At first, the DL would have to be characterized by very low thermal and optical electron excitation to the conduction band inhibiting the sign reversal in group (IV) samples. Secondly, the positive sign of R_H even above the bandgap excitation with significant enhancement of PhC testifies to an existence of a recombination level suppressing photo-excited electrons in these samples. Such level

captures photo-excited electrons regardless of the nature of the excitation process and enhances carrier's recombination. Consequently, the direct identification of DLs cannot be simply deduced from the sign of R_H. Furthermore, levels at the 1.25 eV energy were rarely observed near the conduction band [31] in contrast to the proximity of the valence band where relatively shallow levels at the energy E_g−1.25 eV ≈ 0.25 eV are routinely reported [27], [31].

PL spectra measured for samples No 7 and No 8 are shown in Fig. 5.2. DL bands with threshold energies at 0.85, 1.05, 1.2 and 1.25 eV can be found.

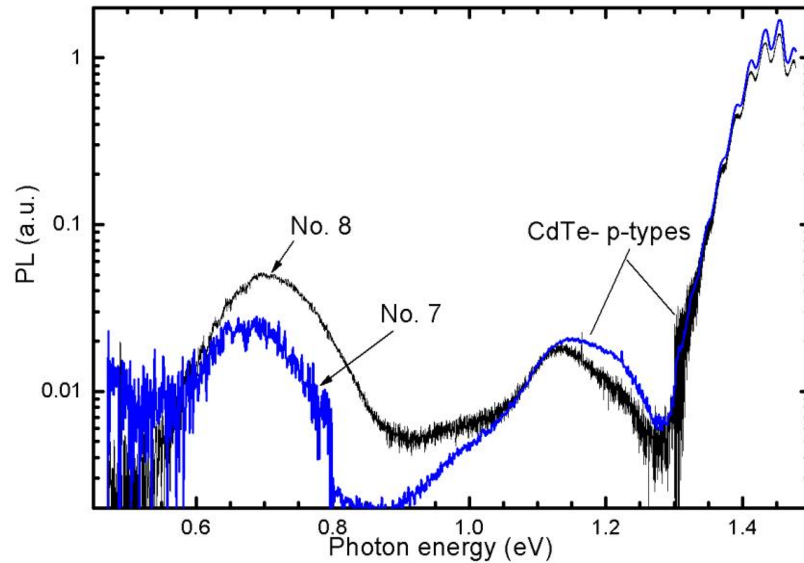

Fig. 5.2. PL spectra representing DLs transitions in CdTe p-type samples. Affiliation of each curve is labeled by a number from the Table 4.

The most realistic model of DLs involving recombination level disables the unique interpretation of transitions at energies well above $E_g/2$ by using PHES either as a single technique or supplemented by PL. On the other hand, the possibility to explore the recombination levels by PHES represents a considerable advancement in the research of properties of DLs. The importance of recombination levels for the understanding of charge dynamics in radiation detectors was highlighted in several recent papers [117]–[119].

With the aim to probe the DLs structure in *p*-type samples more deeply, we completed the excitation sources and used 0.95 eV and 1.26 eV Laser Diodes, which allowed us a significant enhancement of the excitation intensity. The most important results obtained on sample No 8 are shown in Fig. 5.3**.** The possibility to reach negative R_H in the group (V) sample attests to the damped activity of recombination

level compared to the group (IV) samples. Analyzing comprehensively PHES as plotted in Figs**.** 5.1(ii) and 5.3, we may identify a tendency of this sample to conserve R_H>0 at given hole density fixed at the lower photon energy excitation. For example, while in Fig. 5.1(ii) the R_H<0 appears at the photon energy above 1.35 eV and the PhC less than $1.5\times10^{-8}\ \Omega^{-1}cm^{-1}$, the excitation at 1.26 eV yields the R_H sign change at the PhC above $3\times10^{-8}\ \Omega^{-1}cm^{-1}$. In addition, the excitation at 0.95 eV did not produce R_H<0 even at the highest photon flux where PhC exceeded $1.5\times10^{-8}\ \Omega^{-1}cm^{-1}$. On extrapolating PHES performed at 0.95 eV excitation to a higher photon flux, the PhC corresponding to the R_H sign change results similar to the case of 1.26 eV excitation. As PhC is dominantly mediated by holes in *p*-type samples, we may conclude that the excitation well below E_g enhances the holes against electrons. This finding indicates the validity of model No 2 in Fig. 2.1 putting the level observed at 1.0 eV in sample No. 8 to the energy E_v + 1.0 eV. The R_H sign change above 1.35 eV at the low-intensity monochromator excitation accords with model No1 and setting of the 1.25 eV DL to the energy E_c–1.25 eV.

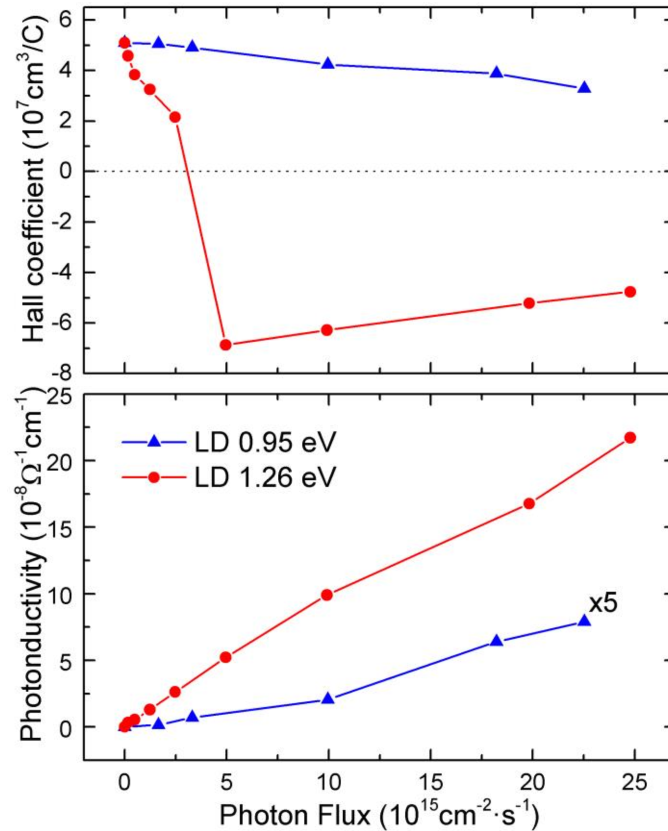

Fig. 5.3. Photo-Hall coefficient and PhC of sample No. 8 as a function of the photon flux at 0.95 eV (blue, triangles) and 1.26 eV (red, bullets) photon energy.

The drop of PHES spectra in all *n*-type and *p*-type samples at the photon energy above 1.45 eV occurs as a result of the enhanced interband light absorption followed by strong surface recombination reducing the free carrier concentration in the sample [19], [120], [121].

5.2. PHES with enhanced white laser illumination in p-$Cd_{1-x}Mn_xTe$

It was shown in the previous chapter that enhanced monochromatic illumination brings detectable minority carrier signal at PHES measurements. A single sample No 9 (group V, Table 4) was chosen for the detailed study involving PHES measurements with enhanced illumination.

5.2.1. Deep levels, carrier mobility, and negative differential photoconductivity

Photoconductivity and Hall mobility spectra measured in the energy range 0.6-1.8 eV under three different photon fluxes are presented in Fig. 5.4. One can see rises and the change of the PhC slope at 0.63, 0.9, 1.0 and 1.3 eV photon energies related to the presence of DLs near these threshold energies. It is important to note here that PhC starts to saturate and change the sign of the derivative in the energy region 0.96 -1.3 eV, Fig. 5.4(a). This effect is known as the negative differential photoconductivity. The Hall mobility μ_H starts to increase from 0.62 eV up to 0.96 eV where it starts to saturate, Fig. 5.4(b) Region I. The increase of μ_H in the p-type sample is reached by the free holes

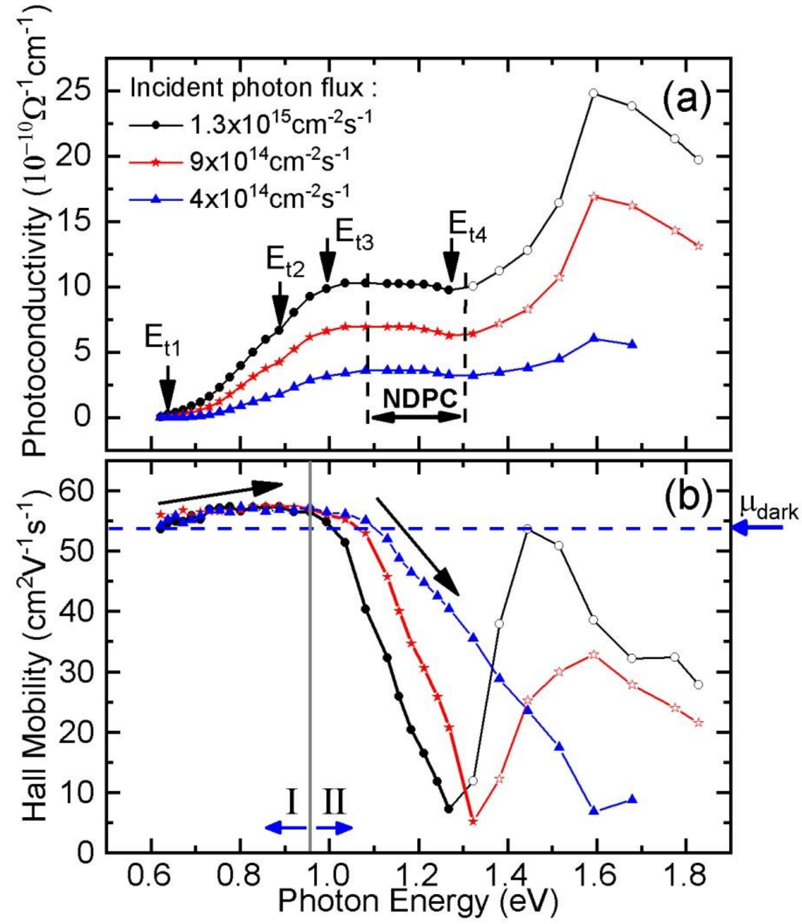

Fig. 5.4. Photoconductivity (a) and Hall mobility (b) spectra at different photon fluxes. Vertical arrows show the deep level threshold energy. Full/empty symbols correspond to positive/negative V_H. The same notation is used throughout in this section.

generation according to Eq. (2.11) associated with the transitions to DLs from the valence band in this energy region as it was mentioned in section 2.2. The μ_H decrease can be observed at hv >0.96 eV, Region II, and the negative sign of V_H is reached near 1.3 eV for a maximal photon flux of 1.3×10^{15} cm^{-2}s^{-1}. The decrease of μ_H is caused by free electrons generated in this region. One can see that the sign change of μ_H depends on the illumination intensity being shifted to higher photon energy at decreasing photon flux 9×10^{14} cm^{-2}s^{-1} and 4×10^{14} cm^{-2}s^{-1}. In contrast to the abrupt change of μ_H induced by photo-electrons, *PhC* remains stable in the energy region 1.0-1.4 eV, which proves the stable hole density dominating in σ and *PhC*. Once a negative sign of V_H is reached, μ_H increases with the further increase of the photon energy in agreement with Eq. (2.10-2.11).

To find the position of DLs relatively to E_c and E_v, i.e. to distinguish the level model 1 and 2 outlined in Fig. 2.1, free carriers concentrations spectra are needed. For evaluation of n and p from Eq. (2.10), and Eq. (2.12) in the mixed conductivity regime corresponding mobilities μ_e and μ_h must be known. The theoretically predicted values were often chosen in the photo-Hall measurements in CdTe [6] and perovskites [12]. However, such choice is not convenient for this analysis and it can lead to incorrect conclusions.

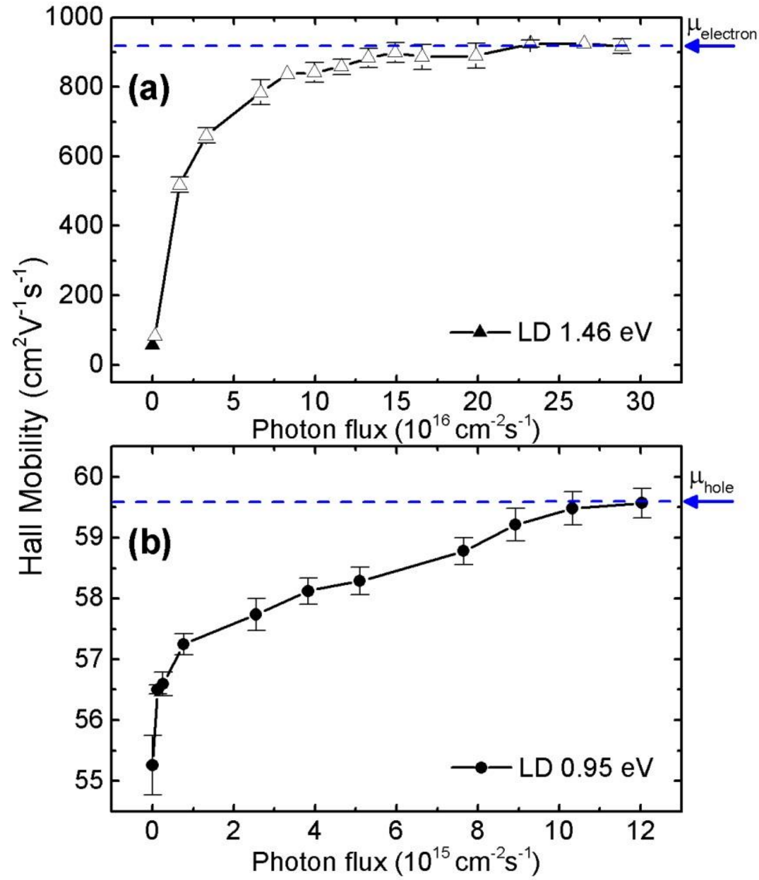

Fig. 5.5. Hall mobility measurements at high photon flux with photon energies 1.46 eV (a) and 0.95 eV (b). Horizontal arrows and the dashed lines show saturation values of the Hall mobility associated with electron and hole mobility. The solid and empty symbols represent data with the positive and negative sign of V_H, respectively.

The real value of mobility affected by actual free carrier density must be measured directly. According to Eq. (2.11) electron or hole mobility can be found in the conditions where only one type of carriers is dominating. As we already found energy regions I and II, where photoexcited holes (with maximal hole mobility at ~0.96 eV), and electrons (with maximal electron effect at ~1.45 eV) dominate, μ_H

was measured as a function of photon flux at these energies using laser diodes as an enhanced illumination source. We show in Fig. 5.5 the rapid increase of μ_H both for electrons in Fig. 5.5(a), where the μ_H saturates at 925±11 $cm^2s^{-1}V^{-1}$, and for holes in Fig. 5.5(b) with saturation at 59.6±0.4 $cm^2s^{-1}V^{-1}$. Saturated values of the Hall mobility observed in Fig. 5.5 (a)-(b) are further associated with free carriers mobility in the homogenous material.

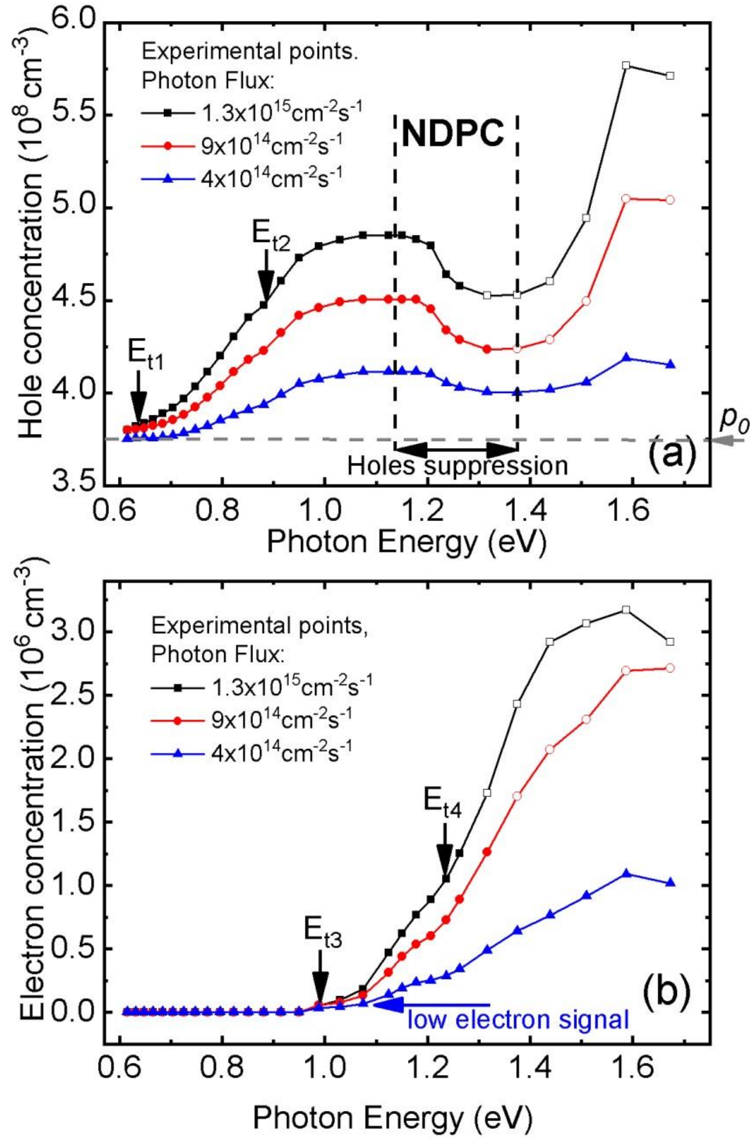

Fig. 5.6. Hole **(a)** and electron **(b)** concentration spectra at different photon fluxes. The vertical arrows show DL threshold energies. Vertical dash lines separate the region of negative differential photoconductivity.

Free electron and hole concentration spectra in the energy range 0.6-1.8 eV calculated from Eq. (2.10-2.12) and data from Fig. 5.4 using saturation values of the Hall mobility are presented in Fig. 5.6. One can see the rise of the hole concentration

at energies 0.63 and 0.9 eV. These changes of the spectra are associated with a photon induced transitions from the valence band to DLs with threshold energies $E_{t1} = E_V + 0.63$ eV, and $E_{t2} = E_V + 0.9$ eV. No free electron generation is detected in the energy region $hv < 0.96$ eV as can be seen from Fig. 5.6(b). Therefore, free electrons are neglected in region I. Corresponding transitions and DLs threshold energies are schematically shown in Fig. 5.7. The rise of the electrons concentration can be observed at 0.96 eV and 1.25 eV photon energies and it is associated with electron transitions from the DLs localized below or close to the Fermi level with threshold energies $E_{t3} = E_c - 1.0$ eV and $E_{t4} = E_c - 1.3$ eV (taking into account the resolution of the output light), which are the subject of model 1 discussed further, or secondary transitions from alternative DLs $E_{t3} = E_V + 1.0$ eV and $E_{t4} = E_V + 1.3$ eV related to model 2. The rise of the electron concentration n is followed by saturation and decrease of the hole concentration p. In view of the fact that NDPC appears at similar photon energy where electrons start to operate, we deduce that principal recombination level responsible for electron-hole recombination rules the process.

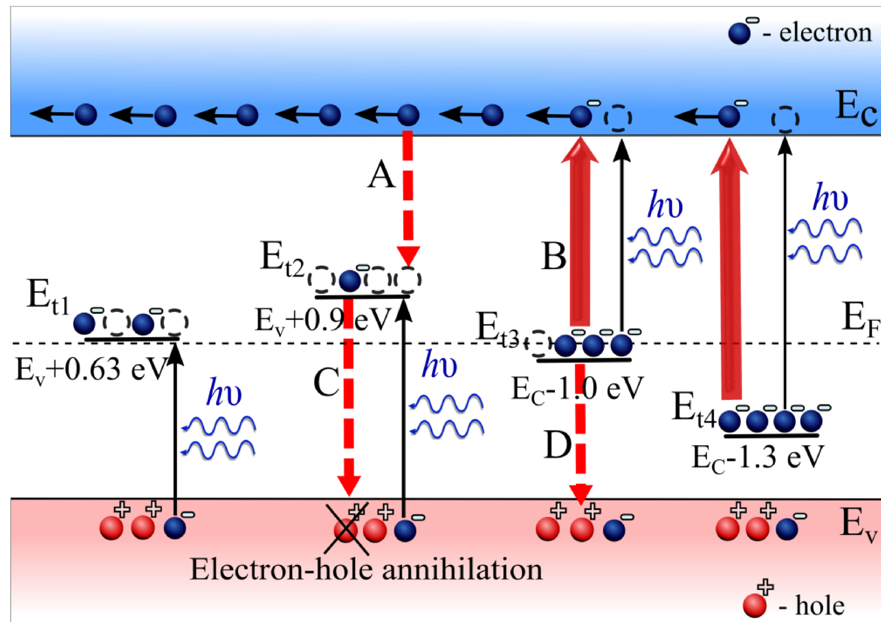

Fig. 5.7. The defect model 1 with marked transitions. Full upward black arrows delineate principal optical excitation. Bold and dashed red arrows show the generation-recombination traffic which leads to electron-hole fast annihilation and decrease (saturation) of holes concentration under illumination.

The *PhC* decrease in this region is damped by the free-electron rise in NDPC region. It is important to note that DLs threshold energies can be mistakenly shifted at lower illumination photon fluxes and such tendency can be seen in Fig. 5.6(b) near photon energy 1.0 eV. The conventional light sources [48] often used with monochromator has the maximal output photon flux of 10^{14} $cm^{-2}s^{-1}$. The electron concentration at photon fluxes less than 4×10^{14} $cm^{-2}s^{-1}$ was undetectable.

5.2.2. Deep level detection and charge carrier Shockley-Reed-Hall simulations

In this section we introduce results of SRH simulation representing the fit of all experimental data according to Eqs. (2.13)-(2.15) with parameters summarized in Table 6, denoted as model 1(a). Models 1(b) and 1(c) depict simulations where the variation of DL parameters take place to see the influence of DL properties on the studied effects, see Table 7. The model 2 is a simulation with alternative DLs position above E_F mentioned in section 2.2.

Table 6. Deep level parameters of the model 1(a), sample No 9.

DL	E_{t1}	E_{t2}	E_{t3}	E_{t4}
Position in the bandgap, eV	$E_V + 0.63$	$E_V + 0.9$	$E_C - 1.0$	$Ec – 1.3$
N_t, cm^{-3}	10^{13}	6.5×10^{12}	3.5×10^{12}	8×10^{12}
σ_e, cm^2	3×10^{-17}	9×10^{-13}	5×10^{-14}	2×10^{-14}
σ_h, cm^2	4×10^{-16}	5×10^{-14}	5×10^{-13}	3×10^{-19}
n_{ti}/N_{ti}*	0.35	10^{-5}	0.49	1

*The relative deep level occupation at the equilibrium.

Holes and electrons concentrations calculated according to Shockley-Reed-Hall model simulations completed by four DLs from the model 1 and model 2 are shown in the Fig. 5.8 by dash and dash-dot lines, respectively. DL threshold energies E_{t1} and E_{t2} are fixed in both models as these energies appear safe. The variation of the model parameters over a wide range according to the DL parameters found in the literature [64], [122] showed that competing model 2 fails to obtain electron

concentration $\Delta n > \Delta p$ in the region $hv > 1.0$ eV, because an emission-like electron generation is followed by a strong hole generation. Moreover, *p* decrease and NDPC are unreached by the same reason. Free holes and electrons behavior in this region exclude the possibility of another DL localization in the band gap (with $E_t > E_F$), where electron rise is produced by secondary electron generation. On the contrary, model 1 shows good results in simulation of the PHES spectra, see curve model 1(a) in Fig. 5.8. This proves the validity of the proposed PHES deep level detection concept. Note that DLs E_{t1}, E_{t2}, and E_{t3} have similar activation energies which can be hardly resolved by photoluminescence or thermal activation methods where DL band overlapping occurs [34], [48]. According to model 1(a) and Table 6 the electron lifetime $\tau_e = 5 \times 10^{-9}$ s is controlled by electron trap DL E_{t2} due to strong recombination. DL E_{t3} plays a minor role in the electron trapping due to lower concentration and electron capture cross section. The majority hole lifetime $\tau_h = 10^{-7}$ s is controlled mainly by the hole trap E_{t3}.

Table 7. Variation of deep level parameters of the model 1(a).

Model No:	Changed parameters:
model 1 (b)	$\sigma_{h2,\ 1(b)} = 10\times\sigma_{h2} = 5\times10^{-13}$ cm^2
model 1 (c)	$N_{t2,\ 1(c)} = 10\times N_{t2,\ 1(c)} = 6.5\times10^{13}$ cm^{-3}
model 2	$E_{t3,\ (2)} = E_V + 1.0$ eV; $E_{t4,\ (2)} = E_V + 1.3$ eV

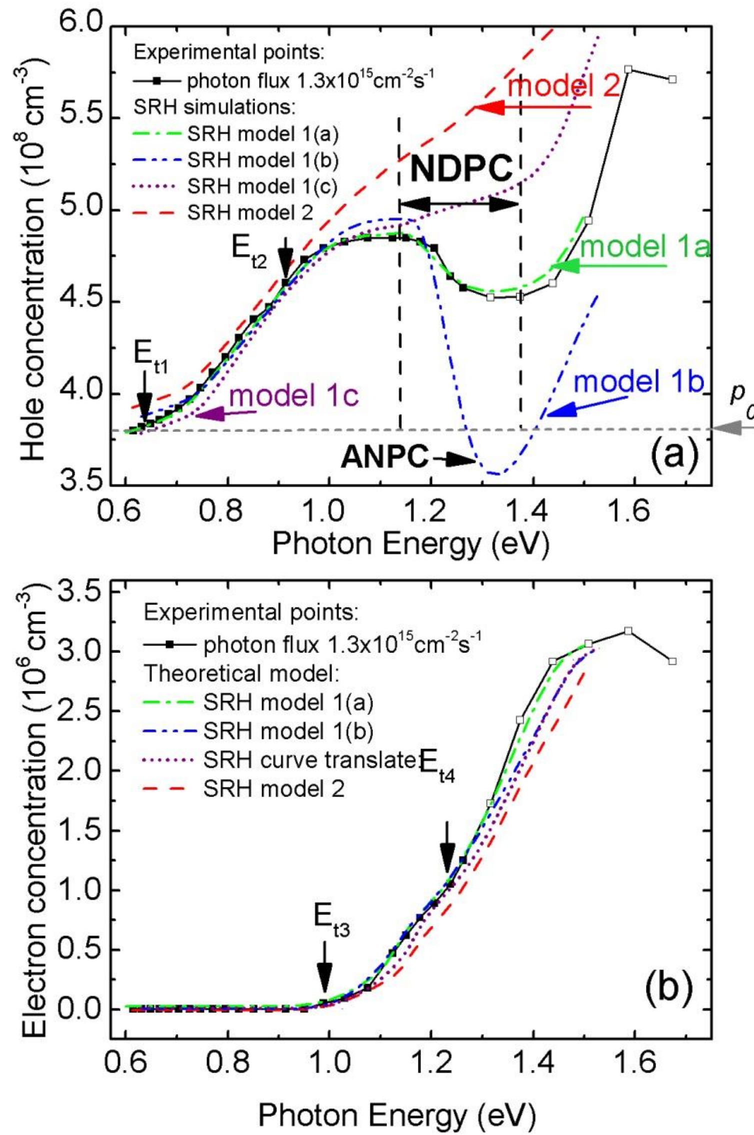

Fig. 5.8. The dashed (dash-dot) curves show SRH model simulations for two possible models (model 1(a) and model 2). Models 1(b) and 1(c) show SRH simulation in case of increased capture cross section and defect concentration of the recombination DL correspondingly. Theoretical curves are calculated for the maximum photon flux. Model 2 and model 1c curves are slightly shifted upwards/downwards for better visualization. The solid line with squares shows experimental data from Fig. 5.6 the maximum photon flux.

5.2.3. Negative differential photoconductivity characterization and charge carrier transport simulations under high illumination flux

Following to experimental results and SRH simulations, the electron generation in the region II is provided by DLs E_{t3} and E_{t4} localized below E_F (model 1) and the hole concentration rises are induced by E_{t1}, and E_{t2}. According to model 1(a) the effect of NDPC detected in Fig. 5.4 (a) is produced by the decrease of the holes concentration confirmed in the experiment, Fig. 5.6(a). The decrease of the majority carrier's concentration under sub-bandgap illumination is reached by minority carrier's fast recombination supported mainly by DL E_{t2} and as result of electron-hole annihilation, as it shown in Fig. 5.7 by bold and dashed red arrows (processes A-D). DL E_{t2} is empty enough to provide strong recombination channel for free electrons. The decrease of hole and increase of electron concentrations match the experimental points in NDPC region and confirm the reliability of the proposed deep level assisted NDPC model.

For further calculation, we chose trap E_{t2} as the most important recombination channel to show the dependence of the main NDPC effects on DL parameters. Another DLs are occupied and have insufficiently low carrier capture cross sections. Therefore, they can hardly serve as strong recombination channel. The effect of holes concentration decrease associated with NDPC depends on the capture cross section σ_{h2} which represents the hole recombination rate of the DL, see Eq. (2.17). The curve of model 1(a), in Fig. 5.8 shows results for $\sigma_{h2} = 5\times10^{-14}$ cm^2 and the model 1(b) represents simulation where $\sigma_{h2,\ 1(b)} = 5\times10^{-13}$ cm^2. The hole concentration decrease can be stimulated even more expressively and the concentration $p < p_0$ can be reached by the σ_{h2} increase. A similar effect can be produced by electron photo-generation ($\sim I\tilde{\alpha}_{ei}$ in Eq. (2.18) increase from the DLs E_{t1}, E_{t3}, or E_{t4}. The effect of the carrier decrease under illumination below the dark equilibrium values is known as absolute negative photoconductivity. We found that decrease in the hole concentration in NDPC region is not observed for capture cross sections $\sigma_{h2} < 2\times10^{-14}$ cm^2.

To show the effect of the recombination DL concentration on p decrease we developed the model 1(c) where the concentration of the recombination channel DL

E_{t2} (2×10^{13} cm^{-3}) is higher by the order of magnitude than in model 1(a) (6.5×10^{12} cm^{-3}), see spectra in Fig. 5.8 (dotted purple line). Despite the fact that the electron lifetime is dropped from the value 5×10^{-9} s to 5×10^{-10} s the decrease of p in the NDPC region is completely suppressed. The main reason of this result is comprised in the increase of DL E_{t2} concentration, which also implies the increase of the terms $\sigma_{hi}v_h(N_{ti}-n_{ti})p_{1i}$ and $I\tilde{\alpha}_{hi}(N_{ti}-n_{ti})$ responsible for free holes thermal and optical generation, see Eqs. (2.14), (2.17) and (2.19). Meanwhile, the recombination term $\sigma_{hi}v_h n_{ti}p$ and electron generation term $I_{ci} = I\tilde{\alpha}_{ei}n_{ti}$ are increasing slowly due to emptiness of the DL above E_F. That's why free holes concentration increases in NDPC region and does not decrease when DL concentration increases. It is important to remind that the deep level E_{t3} acts as an alternative recombination channel in case of the absence of the deep level E_{t2}. Therefore, to define the lower concentration of the recombination channel at which NDPC is observed, DL E_{t3} must be included for analysis. We have found that the decrease of the holes concentration under illumination was observed when DL concentrations met the following relation

$$10^{10}cm^{-3} < \frac{N_{t2}+N_{t3}}{2} < 2\times10^{13}cm^{-3}. \quad (5.1)$$

As one can see, even in the material with relatively low defect concentration [104] NDPC can be stimulated. Multiplying left part on the limit value for capture cross section we get NDPC lower limit rule for CdMnTe material.

$$N_t\sigma_h > 2\times10^{-4}cm^{-1}. \quad (5.21)$$

It should be noted that in case of absence of the electron generation channels (DLs E_{t3} and E_{t4} localized below E_F) the NDPC effect vanishes, see Fig. 5.8(a) model 2. This illustrates an important fact that both recombination and minority carrier generation channels must be present in the material showing the negative differential photoconductivity effect.

The sub-bandgap illumination is often used to study the detector's performance instead of X- and gamma-ray or alpha particle radiation sources [123], [124]. The carrier concentrations of $Cd_{1-x}Mn_xTe$ and detector grade CdTe (CdTe sample without NDPC effect) were studied under extensive 1.46 eV laser illuminations, to show the influence of discovered DLs and NDPC on the material absorption properties. One can see in Fig. 5.9 that the hole concentration starts to saturate and reaches the saturation value of 1.8×10^{9} cm^{-3} at photon flux 7×10^{16} $s^{-1}cm^{-2}$ in $Cd_{1-x}Mn_xTe$ sample. The further increase of the photon flux does not yield in the free holes concentration

enhancement. The suppression of p is followed by a slow superlinear increase of n. The proposed NDPC deep level model 1(a) presented by a solid curve is in a good agreement with experimental data. Experimental data and SHR simulations with DLs positions in the bandgap discovered by PHES show that such holes suppression and superlinear electron raise are the consequence of the recombination through half empty DL E_{t2} (and partially DL E_{t3}) and further electron-hole annihilation. Numerical simulations also show that in the absence of the electron generation channel depicted in model 2 no NDPC can be observed and the same as for PHES spectra electron generation is followed by the higher hole concentration. In case of accentuated recombination channel, model 1(b), the appearance of NDPC effect is followed by ANPC at higher flux as it was predicted by the PHES spectra simulation Fig. 5.8(a) NDPC region.

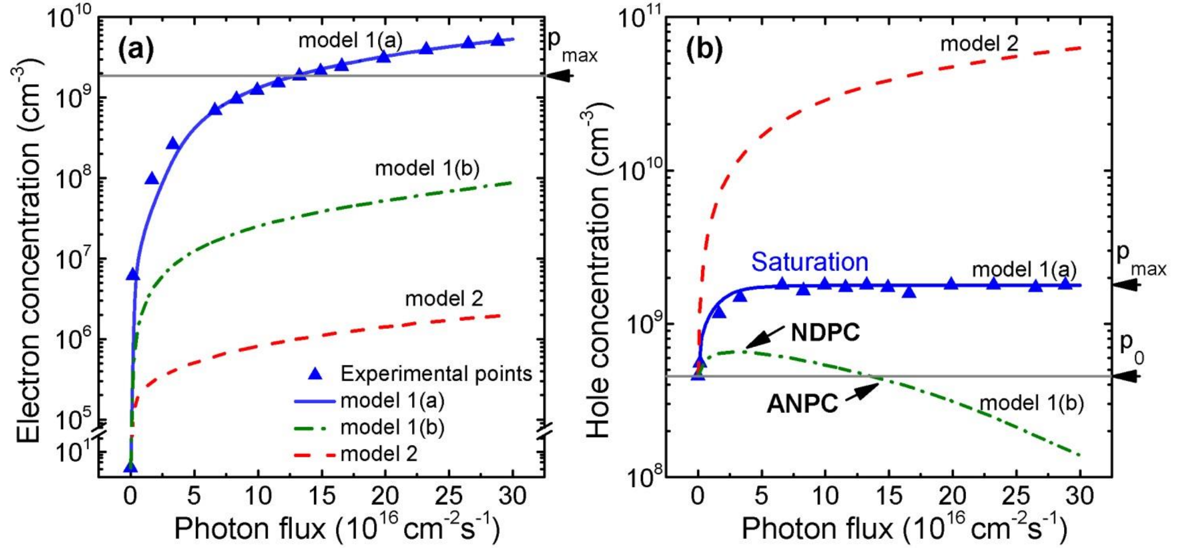

Fig. 5.9. **(a)** Electron and **(b)** hole concentration as a function of photon flux at 1.46 eV high-flux illumination in $Cd_{1-x}Mn_xTe$. Dashed curves show SRH simulations with DLs from Fig. 5.7 (model a).

The occupancy of deep levels of model 1(a) as a function of photon flux is shown in Fig. 5.10 by means of reduced filling factor $F_i(I)$. The electron generation at 1.46 eV photon energy is supported by DLs E_{t1}, E_{t3} and E_{t4} as it can be seen from the depletion of the corresponding DLs. The recombination of minority electrons is driven by DLs E_{t2} and E_{t3} where the increased occupation of DLs is observed. Note nontrivial occupation shape of DL E_{t3}. According to Eq. (2.13) the generation rate I_{ci} is connected to recombination rate U_i^e. With increasing illumination intensity both

terms are increasing, see Eqs. (2.13) and (2.18). Due to initial depletion tendency of DL E_{t3}, the electron thermal emission part of the net recombination rate $\sigma_{ei}v_e n_{ti} n_{1i}$ is decreasing in comparison to equilibrium state. On the contrary, the electron capture rate $\sigma_{ei}v_e(N_{ti} - n_{ti})n$ is increasing and predominates the thermal emission part.

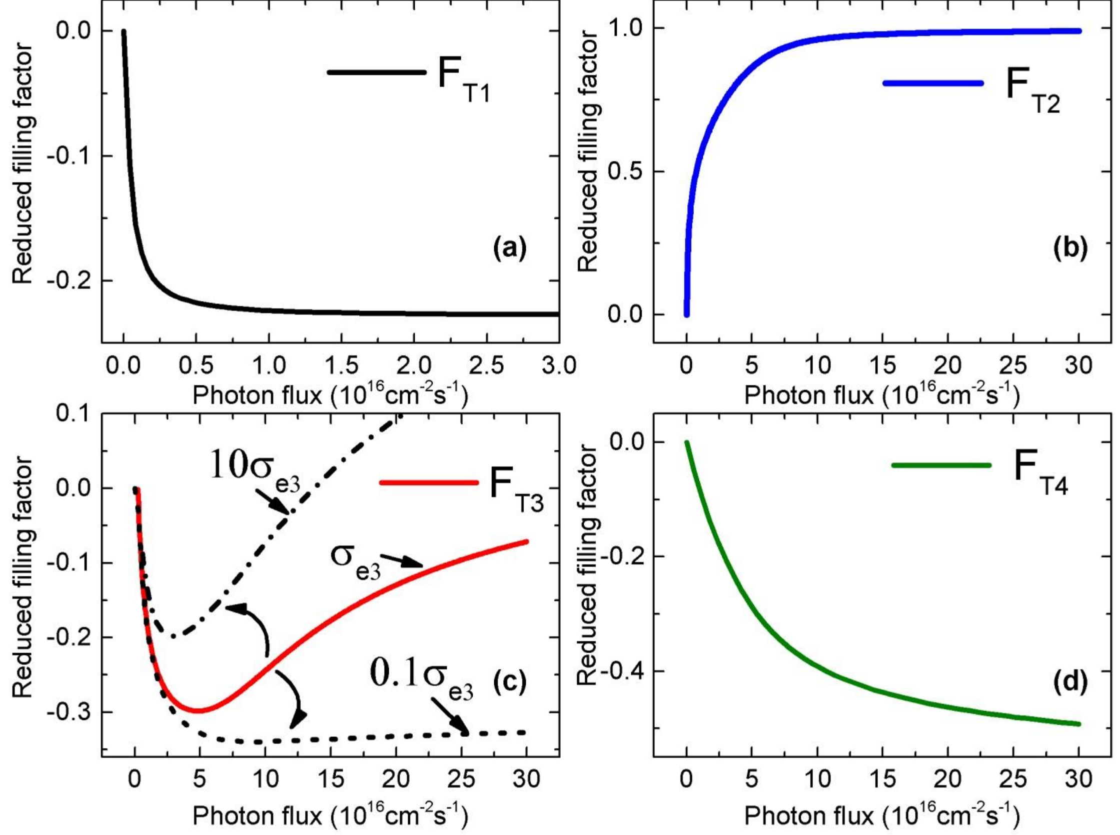

Fig. 5.10. Deep level reduced filling factor calculated by SRH theory for model 1(a) with deep levels from Fig. 5.7.

Similar tendencies are observed for the hole associated processes U_i^h and I_{vi}. The steady state conditions for trapped electrons (holes) are preserved in Eq. (2.22). Note that the electron generation rate I_{ci} is proportional to n_{ti} and hole generation rate I_{vi} is proportional to $N_{ti} - n_{ti}$. Due to the initial tendency of electron depletion of partly filled DL, hole generation rate is increasing faster than the electron one. This synergy of facts leads to nontrivial DL E_{t3} occupation. To emphasize the influence of the electron recombination trough DL E_{T3} on non-trivial occupation behavior (process A, Fig. 5.7), we present occupancy profiles for enlarged and reduced electron capture cross section σ_{ei} in Fig. 5.10(c). The understanding of complicated dynamics of the

space charge in radiation detectors utilized at high flux was a serious problem so far [24], [80], [125]–[127].

5.2.4. Chapter summary

We have detected by PHES four DLs in p-type samples listed below: E_v + 0.70 eV, E_v + 0.85 eV, E_c – 1.25 eV, E_v + 1.0 eV. All energies agree well with those identified by PL. In the case of DLs E_c – 1.25 eV the recombination level participating in the charge dynamics disabled our unique localization of levels. DL threshold energy was interpreted by means of additional measurement of photon flux dependence.

The DL structure was further studied for CdMnTe sample No 9 (group V) by PHES with enhanced illumination. We showed that values of minority (925±11 $cm^2s^{-1}V^{-1}$) and majority (59.7±1 $cm^2s^{-1}V^{-1}$) carriers mobility can be measured directly using proper illumination energy and information about the relative DL position in the bandgap obtained from photo-Hall effect spectra. Four deep levels with ionization energies $E_{t1} = E_V + 0.63$ eV, eV, $E_{t2} = E_V + 0.9$ eV, E_{t3} = Ec – 1.0 eV and $E_{t4} = E_C - 1.3$ eV were detected in p-type CdMnTe and relative positions in the bandgap were verified by comparison of photogenerated electron and hole concentrations. The proposed concepts were analyzed and alternative DL models were rejected by Shockley-Reed-Hall charge generation-recombination simulations. We showed that the extended operation photon fluxes ($I > 4\times10^{14}$ $cm^{-2}s^{-1}$) used in the spectra acquisition is a keystone of the PHES method.

We explained the appearance of negative differential photoconductivity by fast minority carrier recombination through the nearly empty DLs and subsequent electron-hole annihilation, which leads to a decrease or saturation of majority carrier concentration. We also presented the comprehensive analysis of NDPC effect by means of SRH simulations. We showed that both recombination and generation channels are necessary to obtain NDPC. The dependence of the effect on DL parameters such as carrier capture cross sections and DL concentration as well as the connection between negative differential photoconductivity and absolute negative photoconductivity was discussed. The influence of such effect on the material performance was studied in the regime of enhanced laser illumination at hv = 1.46 eV. The effect can be observed even in a material with relatively low defect

concentration and it can be suppressed by the decrease in deep level concentration. The occupation of DLs was studied by means of SRH simulations. Nontrivial occupation shape of a hole trap with activation energy $E_C - 1.0$ eV was detected and explained by a synergy of enhanced electron recombination and hole generation.
All DLs detected by PHES in samples from Table 4 are summarized in Attachments, Table A.

6. Characterization of polarizing semiconductor radiation detector by laser-induced transient currents

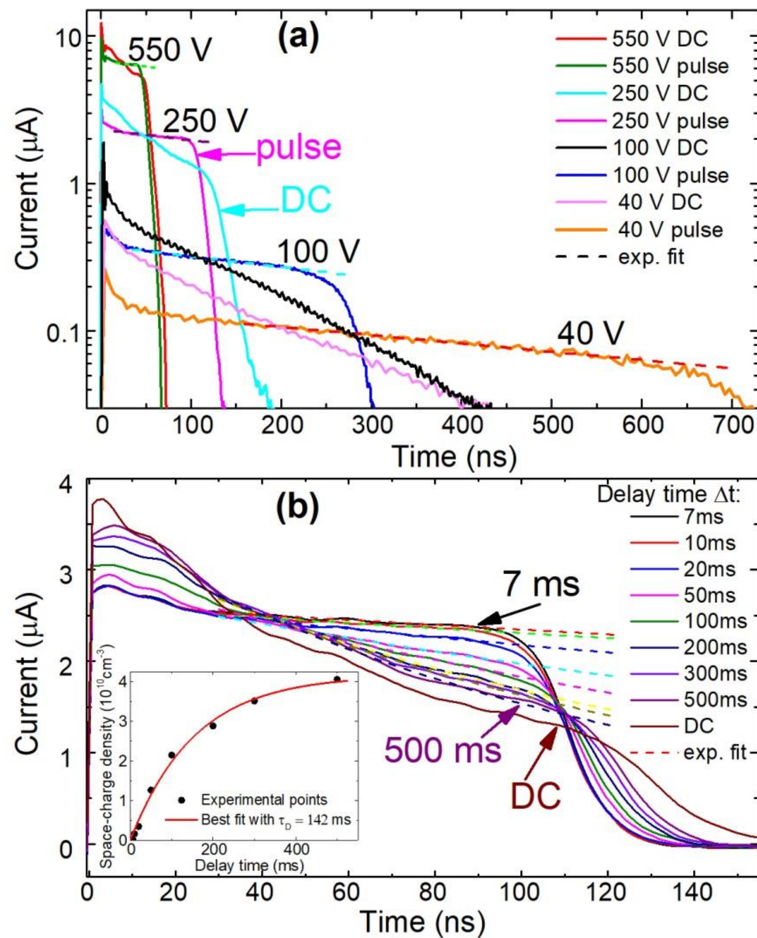

Fig. 6.1. (a) L-TCT CWFs measured at 40V, 100 V, 250 V and 550 V bias in the pulse with Δt=10ms and steady-state (DC) regimes corresponding to the flat/tilted CWFs. **(b)** L-TCT CWFs measured at 250 V bias in the pulse mode. Each waveform was obtained with given delay time Δt. Dashed lines plot the exponential fit of transients. The inset shows the space-charge density as a function of the delay time according to Eq. (2.40).

In previous chapters we showed DL structure of multiple samples detected by PHES measurements. In this chapter we study the polarization of CdTe detector produced by the space charge associated with mentioned charged DL states. The influence of the space charge on main detector properties is presented based on L-TCT measurements at pulsed and DC regimes. Sample No 4 presented in Table 4 was chosen. The electron mobility, μ=1050 cm^2/Vs, was determined from the bias dependence of the drift velocity fit according to Suzuki et. al [99].

Examples of CWFs after the Δt=10ms pulsed and steady-state biasing by 40 V, 100 V, 250 V, and 550 V are plotted in Fig. 6.1(a). One can see the influence of the positive space charge formation on the CWFs represented by the gradual tilting of the CWF in time. The space charge also leads to the disappearance of the visible bending of CWF at 40 V and 100 V, which correspond to the growth of transit time to the infinity and the formation of inactive region near anode as it was predicted in model (B) in Chapter 2.5 above.

Fig. 6.1(b) shows CWFs measured with different time delay Δt after biasing at 250V. The slope c of CWF increases monotonically with the increase of Δt. The space charge density obtained using Eq. (2.37) is plotted in the inset of Fig. 6.1(b) and it was used for the fitting of detrapping time τ_D, Eq. (2.41). The detrapping time τ_D = 142 ms of DL associated with the space charge formation was found using the fit by Eq. (2.40). The lifetime for uncharged detector determined according to Eq. (2.39) resulted in τ_0=800 ns. The corresponding $\mu\tau_0$=8.4×10^{-4} cm^2/V represents the mobility-lifetime product of the uncharged detector. It exceeds $\mu\tau_{He}$ determined with the Hecht equation 2.48.

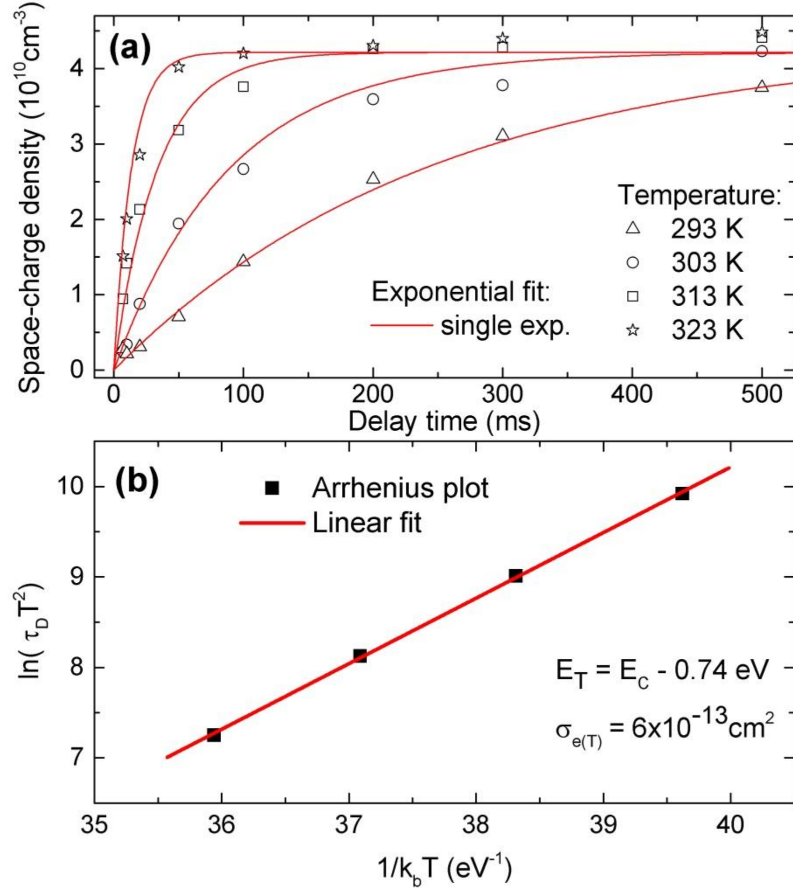

Fig. 6.2. (a) Space-charge density as a function of the delay time measured at different temperatures at 550 V bias. The full lines show the single exponential fit. **(b)** Arrhenius plot according to the detrapping time obtained from Fig. 6.2(a).

The time evolution of the space charge density measured at distinct temperatures is plotted in Fig. 6.2(a) together with the fit according to Eq. (2.40). The DL ionization energy and electron capture cross section can be obtained from the τ_D temperature dependence. The DL ionization energy E_T=E_c-0.74 eV and the electron capture cross-section $\sigma_{e(T)}$=6×10^{-13} cm^2 were determined according to the fit of Arrhenius plot (Eq. 2.42) in Fig. 6.2(b).

The lifetime τ was determined using model (B) by searching for the voltage at which the CWF is transformed to the single-exponential shape. Results are presented in Fig. 6.3 where the steady-state CWFs are plotted in the logarithmic scale. We clearly see the transformation of the bent curve obtained at 100V to the single exponential linear shape at 80V. Taking U=80V as the limiting voltage defined by Eq. (2.43), the space charge density N(80V)=3.1×10^{10} cm^{-3} and the lifetime τ(80V)=460 ns were obtained. On recalling the iterative Hecht fit above, N(80V) as

well as $\mu\tau$(80V)= 4.8×10^{-4} cm^2/V are in a very good agreement with fitted N and $\mu\tau_{He}$.

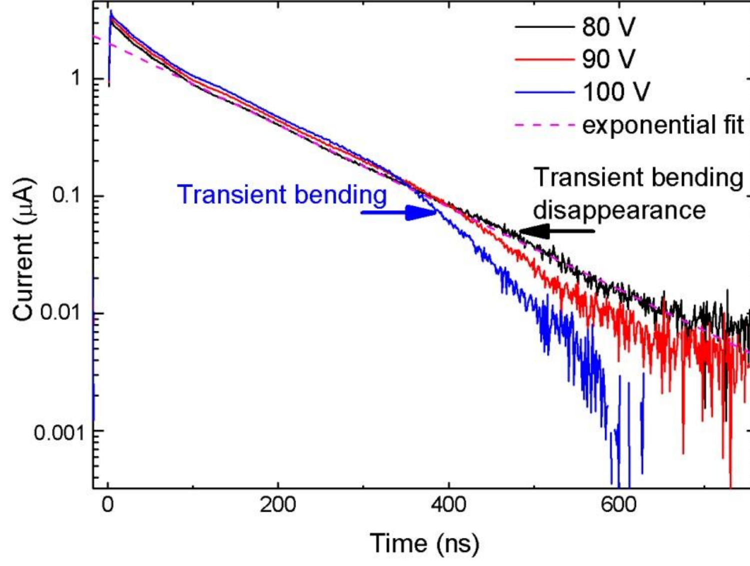

Fig. 6.3. L-TCT waveforms measured in DC regime at 300K at different biasing. The process of the disappearance of CWF bending can be seen with decreasing voltage. The dashed curves represent the exponential fit of the transient.

Substituting parameters c and τ obtained in model B into equation (2.47) resulted in σ_e = 9×10^{-13} cm^2, which is similar to $\sigma_{e(T)}$ found by the thermal spectroscopy. The deviation of $\sigma_{e(T)}$ and σ_e can be explained by considering the well-known drawback of thermal emission spectroscopy techniques, which provide $\sigma_{e(T)}$ associated with σ_e by the formula [34]

$$\sigma_{e(T)} = \frac{g_0}{g_1}\sigma_e e^{\frac{\alpha}{k_b}}, \tag{6.1}$$

where α= $-dE_t/dT$ and g_0/g_1 is the ratio of degeneracy factors. Let us note that α, g_0, and g_1 are hardly accessible experimentally and they are usually omitted at the DLs characterization. Making use of the parallel discovery of both $\sigma_{e(T)}$ and σ_e; $\sigma_{e(T)}/\sigma_e$ = $e^{\alpha/kb}g_0/g_1$=0.7 could be assigned. Though the difference of capture cross-sections obtained in this sample by means of the Arrhenius fit and the fit of transient currents is small, the suggested technique represents a general scheme that may be applied in materials where the distinction of $\sigma_{e(T)}$ and σ_e could reach a significant degree.

Determining the properties of the electron trap, its effect on evaluated parameters may be accounted as outlined by Eqs. (2.45-2.46). Taking the data of the polarized sample biased at 250V in the DC regime at 293 K shown in Fig. 6.1(b), where space charge density N=4.2×10^{10} cm^{-3} was determined, the improved approach

yields N=3.8×10^{10} cm^{-3}. The lifetime decreased markedly from τ_0=800 ns down to τ=430 ns. Subsequently, $\mu\tau$ dropped down to $\mu\tau$=4.5×10^{-4} cm^2/V, which is close to $\mu\tau_{He}$ determined using the Hecht equation. The proximity of $\mu\tau$s established by independent approaches proves the validity of the proposed concept.

Summarizing, we developed two independent techniques based on L-TCT and supported by Hecht equation fit, which may be used for the comprehensive characterization of radiation detector materials without extensive numerical calculations. The utility of the theoretical model was demonstrated on the fast polarizing n-CdTe where the electron mobility 1050 cm^{2}V^{-1}s^{-1}, initial lifetime 800 ns falling down to 430 ns in the polarized detector, deep level energy E_T(eV)=E_c-0.74 and electron capture cross-section σ_e=9×10^{-13} cm^2 were found.

We may conclude that the combination of thermal spectroscopy and transient techniques opens a possibility of how to recognize parameters of DLs, which have so far been hardly accessible in experiments.

7. Conclusions

The first goal of this thesis was to reintroduce Photo-Hall effect spectroscopy and to represent the PHES modifications, such as PHES with dual-wavelength and enhanced illumination, to the research of deep levels in semi-insulating semiconductors. The set of n-type and p-type CdTe and CdZnTe samples was measured and advantages consisting in the possibility to identify the type of the level and hidden characteristics, as well as drawbacks of the method, were discussed. It was concluded that PHES is a useful tool for the study of properties of deep levels which are hardly accessible in other methods, including the properties of recombination levels. The data obtained from PHES can be further used for developing of a charge generation-recombination theoretical model. It was shown that such model is very useful for the detailed analysis and understanding of effects like negative photoconductivity and superlinear/sublinear dependence of photoconductivity on illumination intensity.

Negative differential photoconductivity was observed in samples No 1 (n-type CdZnTe) and No 9 (p-type CdMnTe). In the case of n-type CdZnTe, NDPC is explained by mobility decrease induced by the potential non-uniformities enhanced by extensive illumination at particular photon energy. In the case of p-type CdMnTe, a second model was developed which consists in the majority carrier's concentration decrease under sub-bandgap illumination reached by fast recombination of minority carriers. The second model was established due to the positive Hall voltage conversion into negative one which is the evidence of free electron impact in photoconductivity. Meanwhile, no signal conversion was observed for n-type CdZnTe.

The final goal of this thesis was to develop a procedure enabling the radiation detector characterization via the laser-induced transient current technique. It was shown that the combination of thermal spectroscopy and transient techniques opens a possibility of how to recognize parameters of DLs, which have been hardly accessible in experiments so far. The guideline for determination of the carrier drift mobility, lifetime, electric field distribution, and the dynamics of space charge formation including the detrapping energy and capture cross-section of dominant trap level in polarizing semiconductor radiation detectors was developed. The procedure

stems from the laser-induced transient current measurements done at a steady-state and pulsed biasing and at variable temperature.

Bibliography

[1] N. Debmann, S. G. Pavlov, A. Pohl, N. V. Abrosimov, S. Winnerl, M. Mittendorff, R. K. Zhukavin, V. V. Tsyplenkov, D. V. Shengurov, V. N. Shastin, and H. W. Hubers, "Lifetime-limited, subnanosecond terahertz germanium photoconductive detectors," *Appl. Phys. Lett.*, vol. 106, no. 17, p. 171109, 2015.

[2] H. O. Funsten, S. M. Ritzau, R. W. Harper, and R. Korde, "Fundamental limits to detection of low-energy ions using silicon solid-state detectors," *Appl. Phys. Lett.*, vol. 84, no. 18, pp. 3552–3554, 2004.

[3] L. Alloatti and R. J. Ram, "Resonance-enhanced waveguide-coupled silicon-germanium detector," *Appl. Phys. Lett.*, vol. 108, no. 7, p. 071105, 2016.

[4] T. Takahashi and S. Watanabe, "Recent progress in CdTe and CdZnTe detectors," *IEEE Trans. Nucl. Sci.*, vol. 48, no. 4 I, pp. 950–959, 2001.

[5] L. A. Kosyachenko, T. Aoki, C. P. Lambropoulos, V. A. Gnatyuk, S. V. Melnychuk, V. M. Sklyarchuk, E. V. Grushko, O. L. Maslyanchuk, and O. V. Sklyarchuk, "Optimal width of barrier region in X/γ-ray Schottky diode detectors based on CdTe and CdZnTe," *J. Appl. Phys.*, vol. 113, no. 5, p. 054504, 2013.

[6] E. Nygard, *Radiation Detectors for Medical Imaging*, J. S. Iwan. CRC Press, 2016.

[7] F. Nava, G. Bertuccio, A. Cavallini, and E. Vittone, "Silicon carbide and its use as a radiation detector material," *Meas. Sci. Technol.*, vol. 19, no. 10, p. 102001, 2008.

[8] A. Butler, P. Butler, S. Bell, G. A. Chelkov, D. V Dedovich, M. A. Demichev, V. G. Elkin, M. I. Gostkin, S. A. Kotov, D. A. Kozhevnikov, U. G. Kruchonak, A. A. Nozdrin, S. Y. Porokhovoy, I. N. Potrap, P. I. Smolyanskiy, M. M. Zakhvatkin, and A. S. Zhemchugov, "Measurement of the energy resolution and calibration of hybrid pixel detectors with GaAs:Cr sensor and Timepix readout chip," *Phys. Part. Nucl. Lett.*, vol. 12, no. 1, pp. 59–73, 2015.

[9] K. Hitomi, T. Tada, T. Onodera, T. Shoji, S. Y. Kim, Y. Xu, and K. Ishii, "Timing performance of TlBr detectors," *IEEE Trans. Nucl. Sci.*, vol. 60, no. 4, pp. 2883–2887, 2013.

[10] E. Kamieniecki, "Effect of charge trapping on effective carrier lifetime in

compound semiconductors: High resistivity CdZnTe," *J. Appl. Phys.*, vol. 116, no. 19, p. 193702, 2014.

[11] G. Korcsmáros, P. Moravec, R. Grill, A. Musiienko, and K. Mašek, "Thermal stability of bulk p-CdTe," *J. Alloys Compd.*, vol. 680, pp. 8–13, 2016.

[12] E. Kamieniecki, "Defect specific photoconductance: Carrier recombination through surface and other extended crystal imperfections," *J. Appl. Phys.*, vol. 112, no. 6, p. 063715, 2012.

[13] M. Rejhon, J. Franc, V. Dědič, J. Kunc, and R. Grill, "Analysis of trapping and de-trapping in CdZnTe detectors by Pockels effect," *J. Phys. D. Appl. Phys.*, vol. 49, no. 37, p. 375101, 2016.

[14] V. Dědič, J. Franc, M. Rejhon, R. Grill, J. Zázvorka, and P. J. Sellin, "De-polarization of a CdZnTe radiation detector by pulsed infrared light," *Appl. Phys. Lett.*, vol. 107, no. 3, p. 32105, 2015.

[15] Q. Le Huy, J. L. Ducote, and S. Molloi, "Radiation dose reduction using a CdZnTe-based computed tomography system: comparison to flat-panel detectors.," *Med. Phys.*, vol. 37, no. 3, pp. 1225–1236, 2010.

[16] A. Burger, M. Groza, Y. Cui, U. N. Roy, D. Hillman, M. Guo, L. Li, G. W. Wright, and R. B. James, "Development of portable CdZnTe spectrometers for remote sensing of signatures from nuclear materials," *Phys. Status Solidi (c)*, vol. 2, no. 5, pp. 1586–1591, 2005.

[17] T. Siegert, R. Diehl, J. Greiner, M. G. H. Krause, A. M. Beloborodov, M. C. Bel, F. Guglielmetti, J. Rodriguez, A. W. Strong, and X. Zhang, "Positron annihilation signatures associated with the outburst of the microquasar V404 Cygni.," *Nature*, vol. 531, no. 7594, pp. 341–3, 2016.

[18] H. A. Mohamed, "Dependence of efficiency of thin-film CdS/CdTe solar cell on optical and recombination losses," *J. Appl. Phys.*, vol. 113, no. 9, 2013.

[19] E. Belas, Uxa, R. Grill, P. Hlídek, L. Šedivý, and M. Bugár, "H1. Belas, E. et al. High temperature optical absorption edge of CdTe single crystal. J. Appl. Phys. 116, 103521 (2014).igh temperature optical absorption edge of CdTe single crystal," *J. Appl. Phys.*, vol. 116, no. 103521, p. 103521, 2014.

[20] J. Zhang, W. Jie, L. Luan, T. Wang, and D. Zeng, "Evaluation of Mn uniformity in CdMnTe crystal grown by the vertical Bridgman method," *J. Electron. Mater.*, vol. 37, no. 8, pp. 1158–1162, 2008.

[21] U. N. Roy, A. E. Bolotnikov, G. S. Camarda, Y. Cui, A. Hossain, K. Lee, W.

Lee, R. Tappero, G. Yang, R. Gul, and R. B. James, “High compositional homogeneity of CdTexSe1-x crystals grown by the Bridgman method,” *APL Mater.*, vol. 3, no. 2, p. 026102, 2015.

[22] K. H. Kim, A. E. Bolotnikov, G. S. Camarda, G. Yang, A. Hossain, Y. Cui, R. B. James, J. Hong, and S. U. Kim, “Energy-gap dependence on the Mn mole fraction and temperature in CdMnTe crystal,” *J. Appl. Phys.*, vol. 106, no. 2, p. 023706, 2009.

[23] K. H. Kim, G. S. Camarda, A. E. Bolotnikov, R. B. James, J. Hong, and S. Kim, “Improved carrier-transport properties of passivated CdMnTe crystals,” *J. Appl. Phys.*, vol. 105, no. 9, p. 093705, 2009.

[24] D. S. Bale and C. Szeles, “Nature of polarization in wide-bandgap semiconductor detectors under high-flux irradiation: Application to semi-insulating Cd1-x Znx Te,” *Phys. Rev. B*, vol. 77, p. 035205, 2008.

[25] H. Elhadidy, V. Dedic, J. Franc, and R. Grill, “Study of polarization phenomena in n-type CdZnTe,” *J. Phys. D. Appl. Phys.*, vol. 47, no. 5, p. 055104, 2014.

[26] S. del Sordo, L. Abbene, E. Caroli, A. M. Mancini, A. Zappettini, and P. Ubertini, “Progress in the development of CdTe and CdZnTe semiconductor radiation detectors for astrophysical and medical applications,” *Sensors*, vol. 9, pp. 3491–3526, 2009.

[27] A. Castaldini, A. Cavallini, B. Fraboni, P. Fernandez, and J. Piqueras, “Deep energy levels in CdTe and CdZnTe,” *J. Appl. Phys.*, vol. 83, no. 4, p. 2121, 1998.

[28] P. M. Mooney, “Photo-deep level transient spectroscopy: A technique to study deep levels in heavily compensated semiconductors,” *J. Appl. Phys.*, vol. 54, no. 1, pp. 208–213, Jan. 1983.

[29] F. Schmidt, H. Von Wenckstern, O. Breitenstein, R. Pickenhain, and M. Grundmann, “Low rate deep level transient spectroscopy - A powerful tool for defect characterization in wide bandgap semiconductors,” *Solid. State. Electron.*, vol. 92, pp. 40–46, 2014.

[30] V. Dědič, J. Franc, H. Elhadidy, R. Grill, E. Belas, P. Moravec, J. Zázvorka, and P. Höschl, “Study of deep levels in high resistivity CdZnTe by discharge current measurement,” *J. Instrum.*, vol. 8, no. 01, pp. C01008–C01008, 2013.

[31] X. Mathew, “Photo-induced current transient spectroscopic study of the traps

in CdTe," *Sol. Energy Mater. Sol. Cells*, vol. 76, pp. 225–242, 2003.

[32] J. Kubat, J. Franc, V. Dedic, E. Belas, P. Moravec, V. Babentsov, P. Hoschl, and R. Grill, "Photoconductivity Mapping of Semi-Insulating CdZnTe," *IEEE Trans. Nucl. Sci.*, vol. 58, no. 4, pp. 1953–1957, Aug. 2011.

[33] J. Zazvorka, P. Hlidek, R. Grill, J. Franc, and E. Belas, "Photoluminescence of CdTe:In the spectral range around 1.1 eV," *J. Lumin.*, vol. 177, pp. 71–81, 2016.

[34] R. Grill, J. Franc, H. Elhadidy, E. Belas, Š. Uxa, M. Bugár, P. Moravec, and P. Höschl, "Theory of deep level spectroscopy in semi-insulating CdTe," *IEEE Trans. Nucl. Sci.*, vol. 59, no. 5 PART 3, pp. 2383–2391, 2012.

[35] K. H. Nicholas and J. Woods, "The evaluation of electron trapping parameters from conductivity glow curves in cadmium sulphide," *Br. J. Appl. Phys.*, vol. 15, no. 7, pp. 783–795, 1964.

[36] V. D. Popovych, F. F. Sizov, O. a Parfenjuk, and Z. F. Tsybrii (Ivasiv), "The effect of inhomogeneous dopant distribution on the electrical transport properties and thermal stability of CdTe:Cl single crystals," *Semicond. Sci. Technol.*, vol. 25, no. 3, p. 035001, 2010.

[37] J. Pousset, I. Farella, S. Gambino, and A. Cola, "Subgap time of flight: A spectroscopic study of deep levels in semi-insulating CdTe:Cl," *J. Appl. Phys.*, vol. 119, no. 10, p. 105701, 2016.

[38] J. Rosenzweig, "Bipolar photo-Hall effect in CdTe," *J. Cryst. Growth*, vol. 59, pp. 263–269, 1982.

[39] F. J. Bartoli, "Characterization of impurities in p-type HgCdTe by photo-Hall techniques," *J. Vac. Sci. Technol. A Vacuum, Surfaces, Film.*, vol. 4, no. 4, p. 2047, 1986.

[40] P. Hubik, J. J. Mares, J. Kristofik, A. Baraldi, C. Ghezzi, and A. Parisini, "Hall and photo-Hall effect measurements on sulphur-doped GaSb," *Semicond. Sci. Technol. April 1995; 10(4) 455 62*, vol. 10, p. 455, 1995.

[41] R. Ascázubi, C. Shneider, I. Wilke, R. Pino, and P. S. Dutta, "Enhanced terahertz emission from impurity compensated GaSb," *Phys. Rev. B - Condens. Matter Mater. Phys.*, vol. 72, no. 4, p. 045328, 2005.

[42] K. Yasutake, H. Kakiuchi, a Takeuchi, K. Yoshii, and H. Kawabe, "Deep-level Characterization in Semi-insulating GaAs by Photo-induced Current and Hall Effect Transient Spectroscopy," *J. Mater. Sci. Mater. Electron.*, vol. 8,

no. 4, pp. 239–245, 1997.

[43] K. C. Lin, M. Y. Li, D. C. Ling, C. C. Chi, and J. C. Chen, "Evolution of hot carrier dynamics in graphene with the Fermi level tuned across the Dirac point," *Phys. Rev. B - Condens. Matter Mater. Phys.*, vol. 91, no. 12, pp. 1–6, 2015.

[44] Y. Chen, H. T. Yi, X. Wu, R. Haroldson, Y. N. Gartstein, Y. I. Rodionov, K. S. Tikhonov, A. Zakhidov, X. Y. Zhu, and V. Podzorov, "Extended carrier lifetimes and diffusion in hybrid perovskites revealed by Hall effect and photoconductivity measurements," *Nat. Commun.*, vol. 7, p. 12253, 2016.

[45] Y. Chen, H. T. Yi, and V. Podzorov, "High-Resolution ac Measurements of the Hall Effect in Organic Field-Effect Transistors," *Phys. Rev. Appl.*, vol. 5, no. 3, pp. 1–9, 2016.

[46] H. T. Yi, Y. N. Gartstein, and V. Podzorov, "Charge carrier coherence and Hall effect in organic semiconductors," *Sci. Rep.*, vol. 6, no. 1, p. 23650, 2016.

[47] A. Musiienko, R. Grill, P. Moravec, G. Korcsmáros, M. Rejhon, J. Pekárek, H. Elhadidy, L. Šedivý, and I. Vasylchenko, "Dual-wavelength photo-Hall effect spectroscopy of deep levels in high resistive CdZnTe with negative differential photoconductivity," *J. Appl. Phys.*, vol. 123, no. 16, 2018.

[48] A. Musiienko, R. Grill, P. Hlídek, P. Moravec, E. Belas, J. Zázvorka, G. Korcsmáros, J. Franc, and I. Vasylchenko, "Deep Levels in high resistive CdTe and CdZnTe explored by Photo - Hall Effect and Photoluminescence Spectroscopy," *Semicond. Sci. Technol.*, vol. 32, no. 1, p. 015002, 2016.

[49] E. Molva, J. I. Pautrat, K. Saminadayar, G. Milchberg, and N. Magnea, "Acceptor states in CdTe and comparison with Zn Te. General Trends," *Phys. Rev. B*, vol. 30, no. 6, pp. 3344–3354, 1984.

[50] W. Jantsch, G. Brunthaler, and G. Hendorfer, "Constant Photo-EPR: A new method for deep level characterization," *Mater. Sci. Forum*, vol. 10–12, no. 14, pp. 515–520, 1986.

[51] J. M. Francou, K. Saminadayar, and J. L. Pautrat, "Shallow donors in CdTe," *Phys. Rev. B*, vol. 41, no. 17, pp. 35–46, 1990.

[52] M. Fiederle, D. Ebling, C. Eiche, D. M. Hofmann, M. Salk, W. Stadler, K. W. Benz, and B. K. Meyer, "Comparison of CdTe, Cd0.9Zn0.1Te and CdTe0.9Se0.1 crystals: application for γ- and X-ray detectors," *J. Cryst. Growth*, vol. 138, pp. 529–533, 1994.

[53] R. Soundararajan, K. G. Lynn, S. Awadallah, C. Szeles, and S. H. Wei, “Study of defect levels in CdTe using thermoelectric effect spectroscopy,” *J. Electron. Mater.*, vol. 35, no. 6, pp. 1333–1340, 2006.

[54] C. Szeles, Y. Y. Shan, K. G. Lynn, a. R. Moodenbaugh, and E. E. Eissler, “Trapping properties of cadmium vacancies in Cd1-xZnxTe,” *Phys. Rev. B*, vol. 55, no. 11, pp. 6945–6949, 1997.

[55] M. A. Berding, “Annealing conditions for intrinsic CdTe,” *Appl. Phys. Lett.*, vol. 74, no. 4, pp. 552–554, 1999.

[56] Y.-C. Chang and R. B. James, “Theoretical studies of Cd vacancies and vacancychlorine complexes in CdTe and CdZnTe,” *SPIE Conf. Proc.*, vol. 3768, pp. 381–391, 1999.

[57] C. P. Ye and J. H. Chen, “Studies of defects in n-type CdTe by charge transient spectroscopy,” *J. Appl. Phys.*, vol. 67, no. 5, pp. 2475–2481, 1990.

[58] E. Molva, K. Saminadayar, J. L. Pautrat, and E. Ligeon, “Photoluminescence studies in N, P, As implanted cadmium telluride,” *Solid State Commun.*, vol. 48, no. 11, pp. 955–960, 1983.

[59] K. D. Tovstyuk, V. G. Deybuk, S. V. Melnichuk, and K. Tovstyuk, “3d-Impurity Levels in CdTe and ZnSe,” vol. 130, no. K153, pp. 153–156, 1985.

[60] N. Krsmanovic, A. W. Hunt, K. G. Lynn, P. J. Flint, and H. L. Glass, “Studies of deep trapping levels in undoped and Sn doped Cd1-xZnxTe by thermoelectric effect spectroscopy and thermally stimulated current,” *Proc. SPIE - Int. Soc. Opt. Eng.*, vol. 4141, pp. 11–22, 2000.

[61] F. Debbag, G. Bastide, and M. Rouzeyre, “THERMAL IONISATION AND PHOTOIONISATION PROPERTIES OF DEEP TRAPS IN n TYPE CdTe,” *Solid State Commun.*, vol. 67, no. 1, pp. 1–5, 1988.

[62] R. KREMER and W. LEIGH, “DEEP LEVELS IN CdTe RE.,” *J. Cryst. Growth*, vol. 86, pp. 490–496, 1988.

[63] A. Zerrai, G. Marrakchi, and G. Bremond, “Electrical and optical characteristics of deep levels in vanadium-doped Cd0.96Zn0.04Te materials by photoinduced current, capacitance, and photocapacitance transient spectroscopies,” *J. Appl. Phys.*, vol. 87, no. 9, pp. 4293–4302, 2000.

[64] K. H. Kim, A. E. Bolotinikov, G. S. Camarda, A. Hossain, R. Gul, G. Yang, Y. Cui, J. Prochazka, J. Franc, J. Hong, and R. B. James, “Defect levels of semi-insulating CdMnTe:In crystals,” *J. Appl. Phys.*, vol. 109, no. 11, p.

113715, 2011.

[65] G. Hendorfer, G. Brunthaler, W. Jantsch, J. Reisinger, and H. Sitter, "PHOTO-EPR AND DLTS OF CdTe : CO," *J. C~stalGrowth*, vol. 86, pp. 497–501, 1988.

[66] H. J. Stocker, "Total negative photoconductance in solids and possibility of a new type of instability," *Phys. Rev. Lett.*, vol. 18, no. 26, pp. 1197–1199, 1967.

[67] M. Liao, Y. Koide, J. Alvarez, M. Imura, and J. P. Kleider, "Persistent positive and transient absolute negative photoconductivity observed in diamond photodetectors," *Phys. Rev. B*, vol. 78, no. 4, p. 045112, 2008.

[68] B. Y. Sun and M. W. Wu, "Negative differential transmission in graphene," *Phys. Rev. B - Condens. Matter Mater. Phys.*, vol. 88, no. 23, p. 235422, 2013.

[69] M. A. Mangold, M. Calame, M. Mayor, and A. W. Holleitner, "Negative Di ff erential Photoconductance in Gold Nanoparticle Arrays in the Coulomb Blockade Regime," *ACS Nano*, vol. 6, no. 5, pp. 4181–4189, 2012.

[70] A. I. Yakimov, A. V. Dvurechenskii, A. I. Nikiforov, O. P. Pchelyakov, and A. V. Nenashev, "Evidence for a negative interband photoconductivity in arrays of Ge/Si type-II quantum dots," *Phys. Rev. B - Condens. Matter Mater. Phys.*, vol. 62, no. 24, pp. 283–286, 2000.

[71] R. Labouvie, B. Santra, S. Heun, S. Wimberger, and H. Ott, "Negative Differential Conductivity in an Interacting Quantum Gas," *Phys. Rev. Lett.*, vol. 115, no. 5, p. 050601, 2015.

[72] A. Musiienko, R. Grill, P. Moravec, G. Korcsmáros, M. Rejhon, J. Pekárek, H. Elhadidy, L. Šedivý, and I. Vasylchenko, "Dual-wavelength Photo-Hall effect spectroscopy of deep levels in high resistive (CdZn) Te with negative differential photoconductivity," *J. Appl. Phys.*, vol. 123, no. 16, p. 161502, 2018.

[73] I. Shalish, C. E. M. de Oliveira, Y. Shapira, and J. Salzman, "Hall photovoltage deep-level spectroscopy of GaN films," *Phys. Rev. B*, vol. 64, no. 20, p. 205313, 2001.

[74] F. Stockmann, "Negative Photoeffekte in Haibleitern," *Zeltschrift fur Phys.*, vol. 356, p. 143, 1955.

[75] M. A. Jafarov, E. F. Nasirov, and S. A. Mamedova, "Negative photoconductivity in films of alloys of II?VI compounds," *Semiconductors*,

vol. 48, no. 5, pp. 570–576, 2014.

[76] C. H. Lui, A. J. Frenzel, D. V. Pilon, Y. H. Lee, X. Ling, G. M. Akselrod, J. Kong, and N. Gedik, "Trion-induced negative photoconductivity in monolayer MoS2," *Phys. Rev. Lett.*, vol. 113, no. 16, p. 166801, 2014.

[77] B. K. Ridley, "A mechanism for negative differential resistance in III-V and II-VI semiconductors associated with the enhanced radiative capture of hot electrons," *J. Phys. C Solid State Phys*, vol. 7, p. 1169, 1974.

[78] R. H. Bube, "Interpretation of hall and photo-hall effects in inhomogeneous materials," *Appl. Phys. Lett.*, vol. 13, no. 4, pp. 136–139, 1968.

[79] Š. Uxa, R. Grill, and E. Belas, "Evaluation of the mobility-lifetime product in CdTe and CdZnTe detectors by the transient-current technique," *J. Appl. Phys.*, vol. 114, no. 9, p. 094511, 2013.

[80] A. Santi, M. Zanichelli, G. Piacentini, M. Pavesi, A. Cola, and I. Farella, "An original method to evaluate the transport parameters and reconstruct the electric field in solid-state photodetectors," *Appl. Phys. Lett.*, vol. 104, no. 19, 2014.

[81] G. Irmer, W. Siegel, G. Kuhnel, X. M. Weng, H. L. Cui, J. Monecke, M. Wenzel, D. A. Anderson, N. Apsley, Y. Kang, K. Krishnaswamy, H. Peelaers, A. Baraldi, F. Colonna, C. Ghezzi, P. J. Briggs, A. B. Walker, D. C. Herbert, F. Meinardi, A. Parisini, and L. Tarricone, "Determination of the effective Hall factor in p-type semiconductors," *Semicond. Sci. Technol. Semicond. Sci. Technol*, vol. 13, no. 1398, pp. 505–511, 1998.

[82] M. Borgwardt, P. Sippel, R. Eichberger, M. P. Semtsiv, W. T. Masselink, and K. Schwarzburg, "Excitation correlation photoluminescence in the presence of Shockley-Read-Hall recombination," *J. Appl. Phys.*, vol. 117, no. 21, p. 215702, 2015.

[83] W. Van Roosbroeck and W. Shockley, "Photon-radiative recombination of electrons and holes in germanium," *Phys. Rev.*, vol. 94, no. 6, pp. 1558–1560, 1954.

[84] A. M. Cowley and S. M. Sze, "Surface states and barrier height of metal-semiconductor systems," *J. Appl. Phys.*, vol. 36, no. 10, pp. 3212–3220, 1965.

[85] D. H. Ryman, R. J. Biersner, and M. James, "A DETAILED ANALYSIS OF THE METAL-SEMICONDUCTOR CONTACT," *Solid. State. Electron.*, vol. 17, no. 3, pp. 217–237, 1974.

[86] E. Rhoderick, "Metal-semiconductor contacts," *IEE Rev.*, vol. 129, no. Pt. I, No. 1, 1982.

[87] U. N. Roy, R. M. Mundle, G. S. Camarda, Y. Cui, R. Gul, A. Hossain, G. Yang, A. K. Pradhan, and R. B. James, "Novel ZnO:Al contacts to CdZnTe for X- and gamma-ray detectors," *Sci. REPORS*, vol. 108, no. 24, p. 242106, 2016.

[88] F.-L. Kuo, Y. Li, M. Solomon, J. Du, and N. D. Shepherd, "Workfunction tuning of zinc oxide films by argon sputtering and oxygen plasma: an experimental and computational study," *J. Phys. D. Appl. Phys.*, vol. 45, no. 6, p. 065301, 2012.

[89] S. Li, Z. Peng, J. Zheng, and F. Pan, "Optimizing CdTe–metal interfaces for high performance solar cells," *J. Mater. Chem. A*, vol. 5, no. 15, pp. 7118–7124, 2017.

[90] G. Zha, W. Jie, X. Bai, T. Wang, L. Fu, W. Zhang, J. Zhu, and F. Xu, "The study on the work function of CdZnTe with different surface states by synchrotron radiation photoemission spectroscopy," *J. Appl. Phys.*, vol. 106, no. 5, p. 053714, 2009.

[91] X. Rong, H. Tian, W. Bi, H. Jin, T. Zhang, D. Guo, and K. Zhao, "Impact of metal electrode work function of CH3NH3PbI3/p-Si planar heterojunction perovskite solar cells," *Sol. Energy*, vol. 158, pp. 424–431, 2017.

[92] F. Behrouznejad, S. Shahbazi, N. Taghavinia, H.-P. Wu, and E. Wei-Guang Diau, "A study on utilizing different metals as the back contact of $CH_3NH_3PbI_3$ perovskite solar cells," *J. Mater. Chem. A*, vol. 4, no. 35, pp. 13488–13498, 2016.

[93] P. N. Murgatroyd, "Theory of space-charge-limited current enhanced by Frenkel effect," *J. Phys. D. Appl. Phys.*, vol. 3, pp. 151–156, 1970.

[94] D. Poplavskyy, W. Su, and F. So, "Bipolar charge transport, injection, and trapping studies in a model green-emitting polyfluorene copolymer," *J. Appl. Phys.*, vol. 98, no. 11, p. 014501, 2005.

[95] I. Farella, G. Montagna, A. M. Mancini, and A. Cola, "Study on Instability Phenomena in CdTe Diode-Like Detectors," *IEEE Trans. Nucl. Sci.*, vol. 56, no. 4, pp. 1736–1742, 2009.

[96] M. Zanichelli, A. Santi, M. Pavesi, and A. Zappettini, "Charge collection in semi-insulator radiation detectors in the presence of a linear decreasing

electric field," *J. Phys. D. Appl. Phys.*, vol. 46, no. 36, p. 365103, 2013.

[97] S. Uxa, E. Belas, R. Grill, P. Praus, and R. B. James, "Determination of electric-field profile in CdTe and CdZnTe detectors using transient-current technique," *IEEE Trans. Nucl. Sci.*, vol. 59, no. 5 PART 3, pp. 2402–2408, 2012.

[98] Y. Cui, M. Groza, D. Hillman, A. Burger, and R. B. James, "Study of surface recombination velocity of Cd1−xZnxTe radiation detectors by direct current photoconductivity," *J. Appl. Phys.*, vol. 92, no. 5, pp. 2556–2560, 2002.

[99] K. Suzuki, T. Sawada, and K. Imai, "Effect of DC bias field on the time-of-flight current waveforms of CdTe and CdZnTe detectors," *IEEE Trans. Nucl. Sci.*, vol. 58, no. 4, pp. 1958–1963, 2011.

[100] R. Grill, E. Belas, J. Franc, M. Bugár, Š. Uxa, P. Moravec, and P. Höschl, "Polarization study of defect structure of CdTe radiation detectors," *IEEE Trans. Nucl. Sci.*, vol. 58, no. 6 PART 2, pp. 3172–3181, 2011.

[101] A. Hossain, A. E. Bolotnikov, G. S. Camarda, Y. Cui, D. Jones, J. Hall, K. H. Kim, J. Mwathi, X. Tong, G. Yang, and R. B. James, "Novel approach to surface processing for improving the efficiency of CdZnTe detectors," *J. Electron. Mater.*, vol. 43, no. 8, pp. 2771–2777, 2014.

[102] S. U. Egarievwe, A. Hossain, I. O. Okwechime, R. Gul, and R. B. James, "Effects of Chemomechanical Polishing on CdZnTe X-ray and Gamma-Ray Detectors," *J. Electron. Mater.*, vol. 44, no. 9, pp. 3194–3201, 2015.

[103] N. Zambelli, G. Benassi, E. Gombia, M. Zanichelli, and D. Calestani, "Electroless gold patterning of CdZnTe crystals for radiation detection by scanning pipette technique," *Cryst. Res. Technol.*, vol. 49, no. 8, pp. 535–539, 2014.

[104] A. Musiienko, R. Grill, J. Pekárek, E. Belas, P. Praus, J. Pipek, V. Dědič, and H. Elhadidy, "Characterization of polarizing semiconductor radiation detectors by laser-induced transient currents," *Appl. Phys. Lett.*, vol. 111, no. 8, 2017.

[105] J. Franc, P. Hlídek, H. Sitter, E. Belas, A. L. Toth, L. Turjanska, and P. Hoschl, "Photoluminescence of deep levels in (CdZn) Te-correlation with diffusion length measurement," *Phys. B*, vol. 273–274, pp. 883–886, 1999.

[106] J. Franc, P. Hlidek, E. Belas, P. Hoschl, L. Turjanska, and R. Varghova, "Determination of energy gap in CdZnTe (x= 0- 0.06)," *Semicond. Sci. Technol.*, vol. 15, pp. 561–564, 2000.

[107] W. Stadler, D. M. Hofmann, H. Alt, T. Muschik, B. K. Meyer, E. Weigel, G. Muller-Vogt, M. Salk, E. Rupp, and K. W. Benz, “Optical investigations of defects in CdZnTe,” *Phys. Rev. B*, vol. 51, no. 16, pp. 10619–10630, 1995.

[108] Š. Uxa, R. Grill, and E. Belas, “Evaluation of the mobility-lifetime product in CdTe and CdZnTe detectors by the transient-current technique,” *J. Appl. Phys.*, vol. 114, no. 094511, p. 094511, 2013.

[109] C. a Dimitriadis, “The mobility of polycrystalline semiconductors under optical illumination,” *J. Phys. D. Appl. Phys.*, vol. 18, no. 11, pp. 2241–2246, 2000.

[110] R. H. Bube, “A new mechanism for superlinear photoconductivity with relevance to amorphous silicon,” *J. Appl. Phys.*, vol. 74, no. 8, p. 5138, 1993.

[111] J. Kubat, H. Elhadidy, J. Franc, R. Grill, E. Belas, P. Hoschl, and P. Praus, “Evaluation of the concentration of deep levels in semi-insulating CdTe by photoconductivity and TEES,” *IEEE Trans. Nucl. Sci.*, vol. 56, no. 4, pp. 1706–1711, 2009.

[112] K. Lee and P. Asbeck, “Numerical study of inhomogeneity effects on Hall measurements of graphene films,” *Solid. State. Electron.*, vol. 106, pp. 34–43, 2015.

[113] T. Kurusu and N. Sano, “Significance of the long-range part of the Coulomb potential on the mobility in impure bulk semiconductors,” *Phys. B Condens. Matter*, vol. 314, no. 1–4, pp. 198–202, 2002.

[114] S. Sarkar, K. R. Amin, R. Modak, A. Singh, S. Mukerjee, and A. Bid, “Role of different scattering mechanisms on the temperature dependence of transport in graphene,” *Sci. Rep*, no. October, p. 16772, 2015.

[115] K. Suzuki, S. Seto, A. Iwata, and M. Bingo, “Transport Properties of Undoped Cd 0 . 9 Zn 0 . 1 Te Grown by High Pressure Bridgman Technique,” *J. Electron. Mater.*, vol. 29, no. 6, pp. 704–707, 2000.

[116] R. Grill, “Screening in compensated semiconductors,” *J. Phys. Condens. Matter*, vol. 7, no. January, p. 3565, 1995.

[117] V. Dědič, J. Zázvorka, M. Rejhon, J. Franc, R. Grill, and P. J. Sellin, “Temporal and temperature evolution of electric field in CdTe:In radiation detectors,” *J. Appl. Phys.*, vol. 116, p. 053702, 2014.

[118] A. Cola and I. Farella, “The polarization mechanism in CdTe Schottky detectors,” *Appl. Phys. Lett.*, vol. 94, p. 102113, 2009.

[119] L. a Kosyachenko, O. L. Maslyanchuk, V. a Gnatyuk, C. Lambropoulos, I. M. Rarenko, V. M. Sklyarchuk, O. F. Sklyarchuk, and Z. I. Zakharuk, “Charge collection properties of a CdTe Schottky diode for x- and γ-rays detectors,” *Semicond. Sci. Technol.*, vol. 23, p. 075024, 2008.

[120] H. Devore, “Spectral Distribution of Photoconductivity,” *Phys. Rev.*, vol. 102, no. 1, pp. 86–91, 1956.

[121] J. Franc, J. Kubát, R. Grill, and P. Höschl, “Influence of space charge and potential fluctuations on photoconductivity spectra of semiinsulating CdTe,” *IEEE Trans. Nucl. Sci.*, vol. 54, no. 4, pp. 1416–1420, 2007.

[122] K. Kim, G. Jeng, P. Kim, J. Choi, A. E. Bolotnikov, G. S. Camarda, and R. B. James, “Influence of the cooling scheme on the performance and presence of carrier traps for CdMnTe detectors,” *J. Appl. Phys.*, vol. 114, no. 6, p. 063706, 2013.

[123] A. Cola and I. Farella, “CdTe X-ray detectors under strong optical irradiation,” *Appl. Phys. Lett.*, vol. 105, no. 20, p. 203501, 2014.

[124] K. Suzuki, T. Sawada, and S. Seto, “Temperature-Dependent measurements of time-of-flight current waveforms in Schottky CdTe detectors,” *IEEE Trans. Nucl. Sci.*, vol. 60, no. 4, pp. 2840–2844, 2013.

[125] L. Abbene, G. Gerardi, and F. Principato, “Digital performance improvements of a CdTe pixel detector for high flux energy-resolved X-ray imaging,” *Nucl. Instruments Methods Phys. Res. A*, vol. 777, pp. 54–62, 2015.

[126] D. S. Bale and C. Szeles, “Electron transport and charge induction in cadmium zinc telluride detectors with space charge build up under intense x-ray irradiation,” *J. Appl. Phys.*, vol. 107, no. 11, p. 114512, 2010.

[127] M. Strassburg, C. Schroeter, and P. Hackenschmied, “CdTe/CZT under high flux irradiation,” *J. Instrum.*, vol. 6, pp. C01055–C01055, 2011.

List of Tables

Table 1. Several semiconductor material properties at 298 K ……………….……..…5

Table 2. Overview of deep energy levels in CdZnTe…………………………….…8

Table 3. Work function of some metals and semiconductors[87]–[92]……..…...…21

Table 4. Samples' data: sample number, conductivity and material type, zinc content, dopant, room temperature conductivity, Fermi energy, DL energies determined by PHES and estimated ZPL in PL, and band gap energy……………………….……29

Table 5. Parameters of the DLs model (sample No 1)………………………….………48

Table 6. Deep level parameters of the model 1(a), sample No 9……………….…….62

Table 7. Variation of deep level parameters of the model 1(a). …………………...…63

List of Abbreviations

CdTe	cadmium telluride
CdZnTe/CZT	cadmium zinc telluride
CdMnTe/ $Cd_{1-x}Mn_xTe$	cadmium mangan telluride
PHES	photo-Hall effect spectroscopy
DWPHES	transient-current-technique
NDPC	negative differential photoconductivity
ANPC	absolute negative photoconductivity
DLTS	deep-level transient spectroscopy
DCM	discharge current measurements
PDLTS	photo-DLTS
PICTS	photo-induced current transient spectroscopy
PL	photoluminescence spectroscopy
ZPL	zero-phonon lines
TEES	thermoelectric effect spectroscopy
DL	Deep level
FWHM	full width at half maximum
VGF	vertical-gradient-freeze
HPB	high-pressure-Bridgeman
THM	travelling-heater-method
C	Czochralski
CVD	chemical vapor deposition
TChT	transient charge technique
LD	laser diode
LED	light emitting diode
$CH_3NH_3PbI_3$	methylammonium lead halide

L-TCT	laser-induced transient current technique
CWFs	current waveforms
CPNUs	Coulomb potential non-uniformities
DC	direct current
Sub./Sup.	sublinear/superlinear
SRH	Shockley-Read-Hall

List of symbols

$\mu\tau$	mobility-lifetime product
L	sample width
$\phi_{m/s}$	work function of metal/semiconductor
$F_{m/s}$	Fermi level of metal/semiconductor
E_{vac}	energy of vacuum
E_c	conducting band
E_v	valence band
ϕ_B	barrier height
χ_s	electron affinity of semiconductor
ρ	resistivity
$\varphi(x,y)$	electrostatic potential
v_{th}	thermal velocity of free carriers
n/p	density of free electrons/holes
N_t	density of trapping centres
τ	lifetime
$\tilde{\alpha}_e$	photon capture cross sections relevant to the conduction band
$\tilde{\alpha}_h$	photon capture cross sections relevant valence band

σ_e	electron capture cross section
σ_h	hole capture cross section
σ	Conductivity
q_e	elementary charge
$\mu_{n/p}$	mobility of electrons/holes
E	electric field strength
v_{dr}	drift velocity of carriers
m_n^*	effective mass of the electron
τ_{sc}	scattering relaxation time
E_g	bandgap energy
k	Boltzmann constant
T	temperature
kT	thermal energy
μ_d	drift mobility
n_t	density of trapped carriers
$f(\boldsymbol{k}; t)$	distribution function
t	time
$\boldsymbol{k}$	momentum
t_r	transit time
ϵ_0	vacuum permittivity
ϵ_r	relative permittivity of the material
PhC	photoconductivity
Δn	photo-generated electrons
Δp	photo-generated holes
B	magnetic field
R_H	Hall coefficient
μ_H	Hall mobility

C_{bb}	band-to-band recombination constant
E_t	deep level energy
E_f	Fermi energy
v	velocity
V	voltage
I	current/photon flux
qV_{Bn}	Schottky barrier
V_{Bi}	the built-in voltage
$\tilde{A}$	Richardson constant
R_C	contact resistivity
n_0	n_0 initial electron density at $t=0$
n_{00}	electron density in the dark
T	transmittance
U_i^e	electron net recombination rate
U_i^h	hole net recombination rate
I_{bb}	interband light induced generation rate
U_{bb}	band-to-band net recombination rate
FF	filling factor
f_i	filling factor
$F_i(I)$	reduced filling factor
τ_D	detrapping time
σ_e	electron thermal capture cross-section (non-affected)
$\sigma_{e(T)}$	thermally determined capture cross-section
n_1	electron density in case of Fermi energy E_F being set to the deep level
$j(t)$	decayed current density
a	linear slope of the electric field

E_0	electric field under the irradiated electrode
N	space-charge density
W	depletion width
Q	total collected charge
Δt	delay after the biasing
c	damping parameter
$\mu\tau$	mobility lifetime product
$\mu\tau_{He}$	mobility lifetime product determined by the Hecht equations
g	degeneracy factor

Attachments

Table A. DL energies determined by PHES, PL, L-TCT and DWPHES

No (Group)	Conduct. type[a]	E_c - E_F (eV)	Detected DLs by PHES (eV)	DLs by PL (eV)
1(I)	n-CZT	0.61	$E_c - 0.65$; $E_c - 0.8$; $E_c - 0.9$; $E_c - 1.1$[a]	0.7 – 1.05 [b]; 1.25
2(II)	n-CZT	0.65	$E_c - 0.8$; $E_c - 0.9$; $E_c - 1.1$[a]	0.65; 0.75; 0.9; 1.25
3(II)	n-CZT	0.70	$E_c - 0.8$; $E_c - 0.9$; $E_c - 1.15$[a]	0.65; 0.75; 0.9; 1.25
4(III)[c]	n-CT	0.65	$E_c - 0.9$; $E_c - 1.15$[b]	1.05; 1.2
5(III)	n-CT	0.65	$E_c - 0.9$; $E_c - 1.15$[a]	1.05; 1.2
6(IV)	p-CT	1.03	$E_v + 0.7$; $E_v + 0.85$; $E_c - 1.25$	0.85; 1.05 1.2; 1.25
7(IV)	p-CT	1.04	$E_v + 0.7$; $E_v + 0.85$; $E_c - 1.25$	0.85; 1.05 1.2; 1.25
8(V)	p-CT	0.93	$E_v + 0.7$; $E_v + 0.85$ $E_v + 1.0$, $E_c - 1.25$	0.9; 1.05; 1.2; 1.25
9(V)[d]	p-CMT	1.1	$E_v + 0.63$; $E_v + 0.9$ E_c - 1.0, $E_c - 1.3$	-

[a]The position relatively to E_C was deduced from data in the literature.

[b] DLs with threshold energies E_C-0.66 eV, E_C-0.75 eV, E_C-0.9 eV, E_V+1.0 eV and E_C-1.2 eV were founded by DWPHES

[c] DL E_C- 0.75 eV responsible for sample polarization was founded by L-TCT by L-TCT.

[d] DLs were founded by PHES with enhanced illumination.